FINAL REPORT
R- DW-414-01

April 27, 2001

INTEGRATED QUANTITATIVE NONDESTRUCTIVE EVALUATION (NDE) AND RELIABILITY ASSESSMENT OF AGING AIRCRAFT STRUCTURES

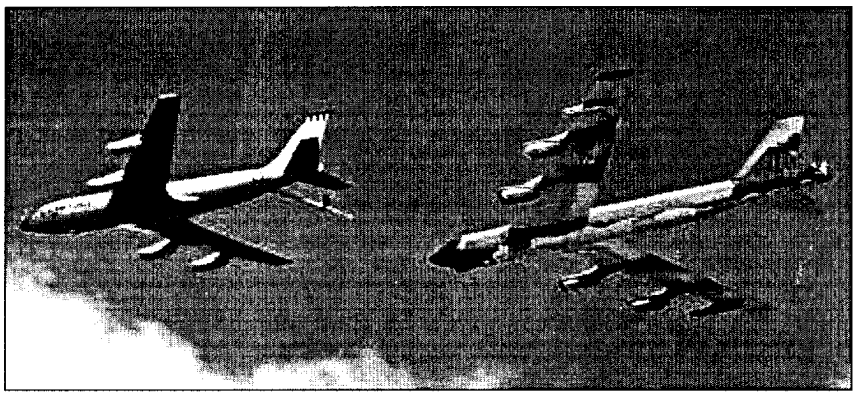

Prepared for: The United States Air Force
Office of Scientific Research

D&W Enterprises, LTD.
8776 W. Mountainview Lane
Littleton, CO 80125-9406
TEL: (303) 791-1940
FAX: (303) 791-1940 - Auto Switch

CENTER FOR NDE
Iowa State University

REPORT DOCUMENTATION PAGE

AFRL-SR-BL-TR-01-

0392

PLEASE DO NOT RETURN YOUR FORM TO THE ABOVE ADDRESS.

1. REPORT DATE (DD-MM-YYYY)	2. REPORT TYPE	3. DATES COVERED (From - To)
27 April 2001	FINAL	1 Sept 1999 to 31 Aug 2000

4. TITLE AND SUBTITLE

Integrated Quantitative Nondestructive Evaluation (NDE) and Reliability Assessment of Aging Aircraft Structures

5a. CONTRACT NUMBER
F49620-99-C-0060

5b. GRANT NUMBER

5c. PROGRAM ELEMENT NUMBER

6. AUTHOR(S)

Ward D. Rummel
John R. Bowler

5d. PROJECT NUMBER
99AF0234

5e. TASK NUMBER
STTR/TX - 1999

5f. WORK UNIT NUMBER
Topic #99-001

7. PERFORMING ORGANIZATION NAME(S) AND ADDRESS(ES)

D&W Enterprises, Ltd,
8776 W. Mountainview Lane, Littleton, CO 80125

Center for NDE
Iowa State University, Ames, Iowa 50011

8. PERFORMING ORGANIZATION REPORT NUMBER
R-DW-414-01

9. SPONSORING/MONITORING AGENCY NAME(S) AND ADDRESS(ES)

AFOSR/PKC
801 N. Randolph St Room 732
Arlington, VA 22203

10. SPONSOR/MONITOR'S ACRONYM(S)
AFOSR/NA

11. SPONSORING/MONITORING AGENCY REPORT NUMBER

12. DISTRIBUTION AVAILABILITY STATEMENT

Report Unlimited

Software Copyright and available (for sale) from the performing organizations.

13. SUPPLEMENTARY NOTES

Further development of the pulsed eddy current system and engiinerring acceptance criteria are necessary to consider the system for commercial application.

14. ABSTRACT

This report documents work performed to understand the capability and reliabiity of a pulsed eddy current inspection / measurement method for the detection and quantification of hidden corrosion in aircraft structures. The method has been shown to be uniquely capability of detection and quantifying corrosion in the second layer and gap thickness between layers of aircraft structure. One element of the program was the development of a first principles model of the the measurement process. The model predicts both applicability and capability for application to typical aircraft structure. The model was validated by limited experimental measurements. A second major element of the project was the upgrade of analysis software for generating probability of detection analysis and plots from experimental and model generated data.

15. SUBJECT TERMS

Pulsed eddy current technology
Nondestructive Evaluation
Pulsed eddy current modeling
Hidden corrosion
NDE capability and reliability
Probability of Detection Analysis
PEC Modeling

16. SECURITY CLASSIFICATION OF:			17. LIMITATION OF ABSTRACT	18. NUMBER OF PAGES	19a. NAME OF RESPONSIBLE PERSON
a. REPORT	b. ABSTRACT	c. THIS PAGE	Unlimited	101	19b. TELEPONE NUMBER (Include area code)

R- DW-414-01 INTEGRATED QNDE AND RELIABILITY ASSESSMENT OF AGING AIRCRAFT STRUCTURES

FINAL REPORT

CDRL ITEM 0001AD

Period Covered 1 Sept 99 to 31 Aug 00

This status report is submitted as in compliance to CDRL ITEM 0001AD, of Contract F49620-99- C-0060, Integrated QNDE and Reliability Assessment of Aging Aircraft Structures. It is submitted as a technical progress report to:

Dr. Spencer Wu
Program Manager

Air Force Office of Scientific Research
AFOSR/NA AATN: Dr. Spencer Wu
801 North Randolph Street, Room 732
Arlington, VA 22203-1977

R- DW-414-01 INTEGRATED QNDE AND RELIABILITY ASSESSMENT OF AGING AIRCRAFT STRUCTURES

TABLE OF CONTENTS

(Click on Name to Link to the Section)

LIST OF FIGURES

(Click on Name to Link to the Figure)

APPENDICES

(Click on Name to Link to the Appendix)

R- DW-414-01 INTEGRATED QNDE AND RELIABILITY ASSESSMENT OF AGING AIRCRAFT STRUCTURES

I. INTRODUCTION

Continuing safe life service of infrastructure is a major challenge in current society and culture. An immediate focus on aging aircraft has generated a multitude of problem analyses and resolution approaches. The development of fracture mechanics as an analysis tool has enabled quantification of scheduled aircraft inspection and maintenance and the quantification damage tolerance characteristics and service margins for crack-like anomalies. Crack-like anomalies due to variance in material quality, service usage (fatigue and physical damage) and environmental initiation are the primary initial consideration in assessing and quantifying structural integrity of engineering materials, structures, components and systems. Crack-like anomalies are the cause for approximately 80% of the aircraft that are retired from service due to degradation in structural integrity. Major technology initiatives have focused on detection and quantification of crack-line anomalies with resultant high confidence in aircraft life extension and major cost savings in operational readiness and aircraft replacement.

Corrosion is frequently cited as a major factor in aircraft maintenance, component replacement, and life-cycle cost. Indeed corrosion is a source of crack initiation with resultant degradation in structural integrity and is of concern due to loss of material and hence general degradation in structural integrity. The engineering parameter most often used for assessing degradation due to corrosion is loss of material / thinning. Fortunately, load redistribution and general margins provide damage tolerance due to corrosion over a wide range of corrosion conditions. Unfortunately, corrosion damage is often hidden and is not detected in a timely manner to enable optimum scheduled arrest, maintenance and replacement. Continuing life extension of aging aircraft has increased the need for both timely detection, quantification and analysis of corrosion (visible and hidden) for safe-life aircraft systems management.

Development and evolution of a measurement technology is often based on what can be measured and on criteria described in terms of what can be measured. In the case of corrosion, wall thinning in an aircraft skin can be measured using available ultrasonic, eddy current and radiometric tools. A loss in wall thickness can then be related to an increase in a local stress concentration using load / stress per unit area analyses. Unfortunately, corrosion also occurs at interfaces and in the second layer of an aircraft structure that may not be accessible and is not reliability assessed by conventional nondestructive evaluation tools. The problem is further complicated by the lack of structural engineering analysis tools and acceptance criteria. Reliable nondestructive measurement / assessment tools are necessary for economical management of corrosion damage and quantified engineering acceptance criteria are necessary to realize benefit from early detection, measurement and characterization. This "chicken and egg" dilemma has been approached by a combination of exploratory approaches to corrosion detection and measurement and by exploratory approaches to understanding and quantifying the effects of corrosion damage on structural integrity. The work described herein addresses elements of an exploratory approach to reliable nondestructive measurement of corrosion damage characteristics and a cursory assessment of related work in establishing acceptance criteria.

R- DW-414-01 INTEGRATED QNDE AND RELIABILITY ASSESSMENT OF AGING AIRCRAFT STRUCTURES

The nondestructive measurement work is an extension of work initiated by the late John Moulder [REF 1] in the application of pulsed eddy current measurements to a two-layer structure that has been modified by corrosion damage. The Moulder work was the result of experimental observations and a deep knowledge of practical eddy current interactions and applications. The advancements provided by the current project were to develop and measurement model for predicting detection capability and improvements in the "probability of detection" analysis tools used in assessing the capability and reliability of nondestructive measurements and applications. Finally, an assessment of potential for commercial implementation of the measurement technique and instrumentation was initiated.

The project reported herein was divided into four tasks:

- Assessment and definition of the need for corrosion measurement based on the pulsed eddy current method;
- Development and validation of a measurement model using the pulsed eddy current method;
- Improvements in the analysis code used for the assessment of nondestructive measurement capability and reliability (probability of detection); and
- Assessment and planning commercial implementation of the pulsed eddy current method (Planned Phase II)

II SIGNIFICANCE OF THE HIDDEN CORROSION PROBLEM AND OPPORTUNITY FOR IMPLEMENTATION OF A PULSED EDDY CURRENT MEASUREMENT

A. GENERAL

The NRC Report, "Aging of US Air Force Aircraft" [REF 2] identifies the most important NDE needs as (1) "Damage detection of fatigue cracks under fasteners"; (2) "Hidden Corrosion"; (3) "Detection of small cracks associated with wide spread fatigue damage (WFD); and (4) "Corrosion in multi-layer structures". Although the need has been broadly identified, specific identification and characterization of that need are necessary to assess the primary factors involved in establishing requirements for measurement and matching those requirements to available technology. Commercialization of a measurement capability (tool, system or service) must include analysis of the need, practicality and economics of a broad application.

Existing ultrasonic, eddy current and radiometric methods adequately measure wall thinning in the first layer of an aircraft structure. In addition, wide area imaging by pulsed infrared methods provide a semi quantitative measure of corrosion patterns and location. Unfortunately, there is no standardized acceptance criteria or methods of using the data provided by these measurements. Indeed, each aircraft manufacturer and user has an individualized method of assessing and using the information provided. A part of the lack of standardization is due to the variation in use and need between commercial, private and military aircraft. The same difficulty is evident in identifying criteria for detection and quantification of hidden corrosion in all aircraft structures. The structures engineering analysis task is difficult and methods of analysis are immature. Indeed, current plans for structures assessment (with respect to hidden corrosion)

include a detailed tear down and analysis of retired aircraft to try to understand the problem and to develop criteria and analytical methods. Two parameters that are evident in analysis needs are the gap between interfaces in multi-layer aircraft skin and corrosion damage in the second layer. The pulsed eddy current measurement method is currently the only method identified which may meet the needs for identification and quantification of characteristic damage conditions.

B. NEED AND ACCEPTANCE CRITERIA

Survey of industry aircraft structure engineering experts reaffirmed the lack of quantified acceptance criteria for second layer corrosion and developmental state of understanding and tools for analysis and management of corrosion damage. The most promising program involves disassembly of a retired commercial aircraft; visual analysis and photographic recording of conditions found; sub-element testing of selected components to assess residual strength and fatigue life; and an exploratory analysis to relate corrosion pitting patterns to residual fracture toughness. Near term closure is not expected.

In summary, there is a recognized need to detect and quantify progressive corrosion damage in aircraft structures. Current practices rely on deterministic engineering judgment for repair / replacement of damaged areas. In addition, corrosion damage to military aircraft differs significantly from that experienced in commercial and private aircraft. The differences are primarily due to differences in materials and alloys, loading / flight profiles, design margins, base facilities environments and maintenance practices.

C. DEFACTO CRITERIA BASED ON INSPECTION / DETECTION CAPABILITIES

In the absence of mature analytical methods and quantified acceptance criteria, the capability of available inspection methods has traditionally been the defacto acceptance criteria. Use of such tools aids in management of engineering structures and maintenance operations and supports increasing understanding of the conditions and effects of the anomaly being assessed. Pulsed eddy current measurement methods have been demonstrated to be capable of:

- Detecting corrosion damage in the form of thinning in the first layer of an aircraft structure;
- Detecting gaps between the first and second layer of an aircraft structure (note that the gap is often increased by the accumulation of corrosion products at the interface); and
- Detecting corrosion damage in the form of thinning in the second layer of an aircraft structure.

Aircraft owners / operators will be reluctant to invest in instrumentation to detect and measure second layer corrosion until a generally accepted acceptance criteria is developed and economic methods of corrosion arrest and remedial action are developed. Technology transfer of pulsed eddy current measurement methods to industry will therefore depend on its capabilities for providing useful measurements in detecting extreme conditions and its usefulness in understanding the conditions and effects of corrosion damage on structural integrity. The primary objectives of the program reported herein were therefore to:

- Increase understanding of the capabilities of the pulsed eddy current method in materials evaluation as applied to corrosion damage;
- Increase understanding of the pulse eddy current method with the objective of establishing confidence in its use as a measurement method;
- Increase awareness of the method as a useful tool for nondestructive measurement and assessment; and
- To explore technology transfer potential including the development and marketing of a commercial instrument for general use in the public domain.

III. THE PULSED EDDY CURRENT (PEC) METHOD

Although several NDE methods are available to detect and assess corrosion damage in the first layer of aircraft structures, the pulsed eddy current (PEC) method developed by Center for Nondestructive Evaluation (CNDE) at Iowa State University (ISU) is the only method that has been demonstrated to be capable of quantifying interface gap (varying amounts of corrosion products) or reliable detection in the second layer [REF 1]. Second layer and hidden corrosion have been identified as major aging aircraft problem conditions. Proof of principle and applicability of the PEC method been demonstrated and validated in related work.

Pulsed eddy current work at CNDE was initiated by the late John Moulder and resulted in the development of a novel approach to application and analysis of the technology. The ISU work is highly leveraged by combined support by this project, by the Federal Aviation Administration (FAA) and by private industry. Joint benefits have been realized by concurrent work on different elements of pulsed eddy current research, methods validation and demonstration on industry products.

Pulsed eddy current measurement is not a new technology. Modern integrated circuit components and digital design capabilities have greatly increased measurement instrument stability and options for complex measurements. The parameters measured and the causal model relationships developed in our work are new innovations that have enabled assessment of corrosion conditions. To our knowledge, the method is a unique advancement in eddy current technology and experimental assessments have shown detection capabilities for hidden corrosion and corrosion a second layers in the presence of a varying interface gap. The PEC technology is an advanced form of the usual continuous-wave (CW) eddy current (EC) method, which is the traditional choice of NDE technique for many inspection applied to aircraft structures. However, in order for CW EC instruments to qualify for the above types of critical inspections, they must operate at low frequencies for deep penetration and at multiple frequencies for depth resolution. These operational requirements are both time-consuming and inconvenient. The time-domain EC method provides an excellent resolution of these shortcomings because, by nature, it can acquire the equivalent of low-frequency and multiple-frequency data in a single pulse. Being a time-domain method, pulsed eddy current provides opportunities to employ time-gating, which has shown excellent discrimination capabilities against interfering signals from fasteners and subsurface structures.

R- DW-414-01 INTEGRATED QNDE AND RELIABILITY ASSESSMENT OF AGING AIRCRAFT STRUCTURES

The state of the art of the ISU PLC technology is found in [REF 1, 6]. This work includes the Cheng-Dodd-Deeds (CDD) theory behind the model-based corrosion characterization. Pulsed eddy-current systems have important advantages from the operator perspective. They can be constructed from simple, relatively inexpensive equipment. Since the method is based on a familiar technology, problems with implementation of the technique in a USAF overhaul or field level NDE facility by USAF personnel would be minimized. By adding a scanning capability to the instrument, the results can be displayed in an image format, which is much easier to interpret and understand. Since pulsed signals contain inherently a broad range of frequencies, pulsed eddy current methods are akin to swept-frequency measurement methods. Yet the pulsed eddy-current technique is much faster: 100 milliseconds to acquire a pulsed eddy-current signal compared to several minutes to complete a swept-frequency measurement. Operation of a prototype instrument has been demonstrated at Tinker, Kelly, McClellan, and Robins Air Force Bases. It was singled out as one of the most promising new technologies for corrosion detection in the second round of blind trials conducted by ARINC, Inc. for Tinker AFB [REF 3,4,5].

The original PEC method demonstrated used a bobbin coil for both generation and detection. A false color image of the test object was generated from the time-gated output signal produced as shown in Figure 1. Figures 2 and 3 describe various features of system functionality.

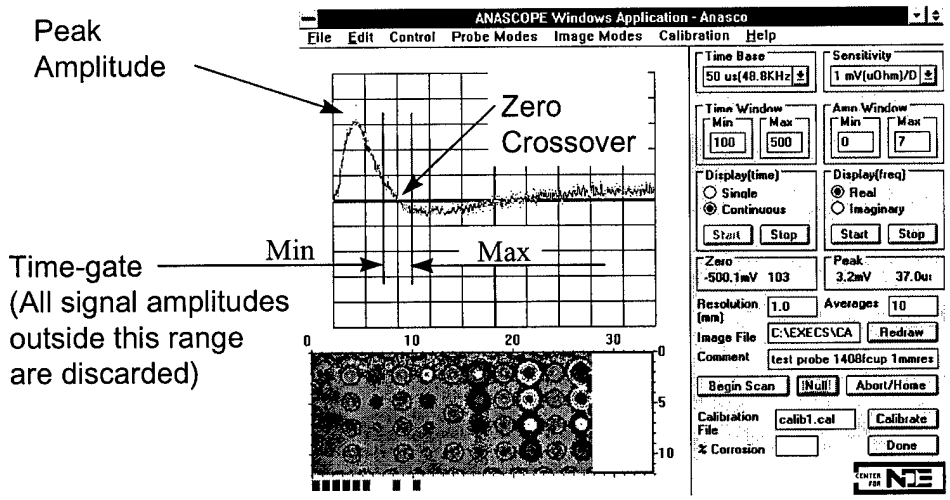

Figure 1. Pulsed eddy current instrument control and display panels (software). The difference between the return and reference signals is plotted as a function of time in the A-scan display. For 2D scans, the instrument displays a C-scan image based on the peak values. The software allows users to display the time-gated C-scan image for a selected range of zero-crossing times.

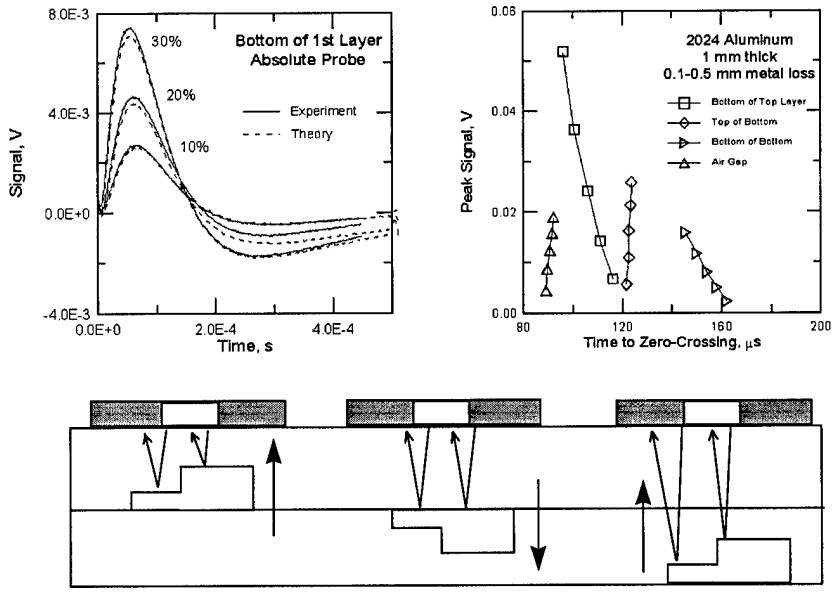

Figure 2. Plots to show the usage of the time-of-flight information, which can determine the severity of corrosion as well as the relative location in the multi layer.

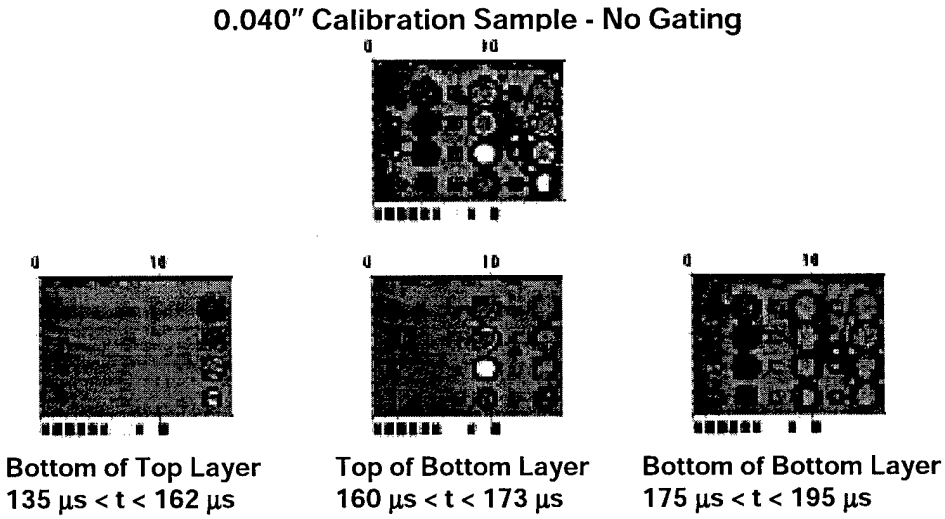

Figure 3. Time-gated vs. non-gated C-scan images. These plots demonstrate that the time-gating method effectively discriminates corrosion signals from other signals of geometrical origins, such as rivets and holes. [REF 1].

R- DW-414-01 INTEGRATED QNDE AND RELIABILITY ASSESSMENT OF AGING AIRCRAFT STRUCTURES

Instrument improvements were made during the current program on a companion project. Detector coils were replaces by Hall- sensors to improve depth of penetration and remove sensitivity to sensor(primarily temperature) changes. The detector board was upgraded to accommodate the Hall-sensor and to improve signal outputs. Detector software was upgraded to Win-32 and analysis / processing improvements were made to remove stringer and tear-strap signals and to improve data storage. Resultant system performance was improved as shown in Figure 4. The depth of penetration was increased using the Hall-sensor as shown in Figure 5.

- **Detection capability: less than 4% material loss in ¼" Al plate.**
- **Depth penetration can be increased, at the expense of measurement time, using a larger probe.**

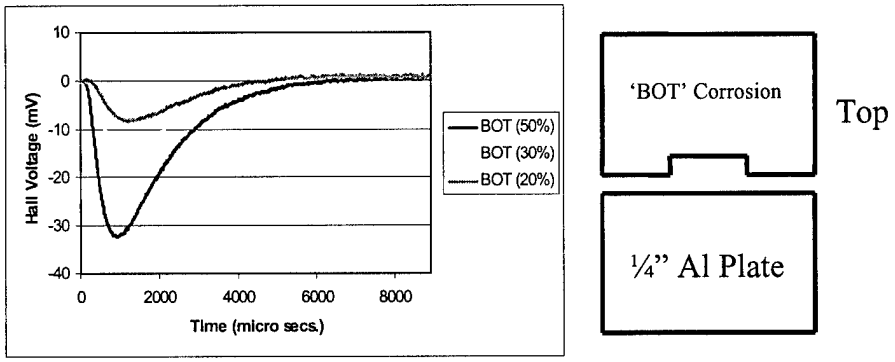

Figure 4. Improved detection capability using the Hall-Sensors.

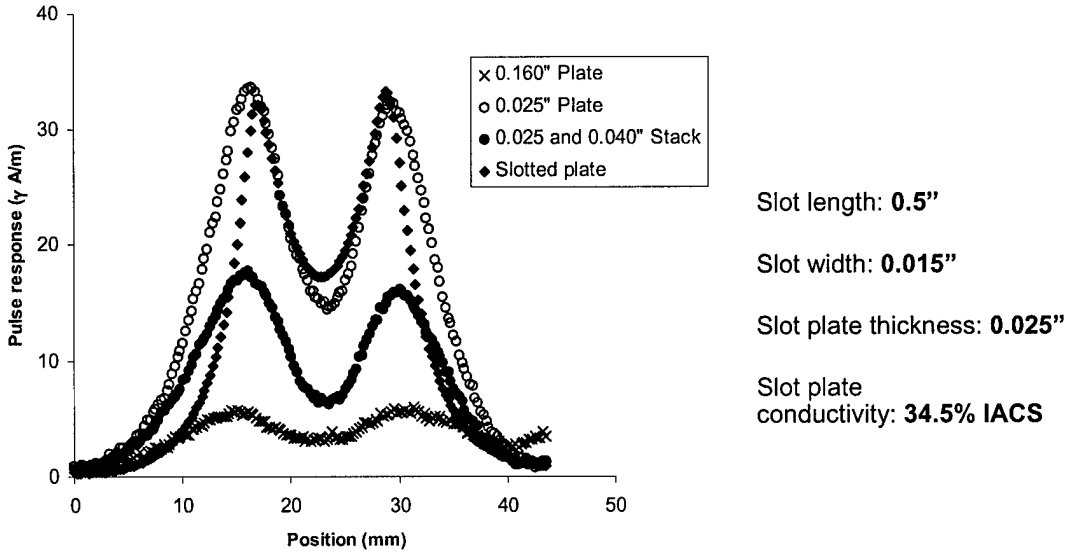

Figure 5 Improvements in depth of penetration using the Hall-sensor

R- DW-414-01 INTEGRATED QNDE AND RELIABILITY ASSESSMENT OF AGING AIRCRAFT STRUCTURES

A summary of the concurrent hardware and experimental tasks completed under funding from the FAA is included for reference in APPENDIX A.

IV. MEASUREMENT MODEL DEVELOPMENT FOR PULSED EDDY CURRENT APPLICATIONS

A major contribution and output of the current project was the development of a measurement model for pulsed eddy current application. The model is a useful tool in understanding various aspects of pulsed eddy current technology and in quantifying expected results for various applications. The predictive model is also a useful input to prediction of detection capabilities and reliability using the probability of detection (POD) models. The model predicts output signal levels in various applications and must be used in combination with experimentally determined noise measurements for use in the POD models. Noise levels are input for laboratory and field measurements and provide the anchor for predicting detection capabilities in the laboratory / field applications [REF 7,8,9,].

John R. Bowler completed the measurement model as an independent task as a part of the CNDE support work. The stand-alone task report for this work is included in Appendix B. The Software program for this model is available from the Center for Nondestructive Evaluation at Iowa State University. [REF 10]. The output of the software model is data in the form shown in Figure 5. Instructions for use of the software model are described in APPENDIX C.

V. PROBABILITY OF DETECTION (POD) MODEL INTERFACE AND UPGRADE

Probability of Detection (POD) is the standard for quantifying the capability and reliability of various nondestructive evaluation (NDE) procedures and applications. The original work in development of the method was completed using a moving average method of quantifying the POD function. This method requires a large amount of data and is uneconomical for most applications. The form of the function is described as the merger of the distributions of signal and noise in a practical application. Signal and noises distributions are expected to be Gausian in form, thus the merger of the two distributions can be described in the form a log logistic model. This method was proposed by Berens [REF 11] and has become the standard for POD data analysis.

The POD (detection) model is based on an assumption that repetitive measurements of a single flaw and the associated measurement noise are normally distributed; and that the measured values provide a means for discriminating between background measurement noise and a flaw signal [REF 7,12,13]. Figure 6, shows a typical desired response with clear discrimination between signal and noise. The measurement distributions are the result of repetitive measurements made on a flaw of a single size. A number of measurements are required to establish confidence in the repeatability of the measurement process. The corresponding confidence level and required sample size are taken directly from statistical sampling tables and are based on random sampling (for example, MIL HDBK 5).

As the flaw size decreases, the measured signal magnitude decreases and approaches the noise measurement levels as shown in Figure 7. Discrimination between signal and noise are more difficult and "FALSE CALLS" will be made when the noise signal is interpreted as a flaw signal. If the acceptance threshold is set low enough (point A) to assure detection of all flaws, a significant number of "FALSE CALLS" will result due to noise being interpreted as a FLAW signal level. Conversely, if the acceptance threshold is set high enough to avoid "FALSE CALLS", some "FLAWS" will be missed and the probability of detection will be low. The useful threshold discrimination point (specificity) for a measurement method is that point at which the probability of detection (POD) exceeds a minimum value (by convention the 90% point) with no false calls (or an accepted level of "false calls"). Some flaws that are smaller than the established threshold POD value will be detected due to flaw-to-flaw variances, but the measurement method will not reliably detect flaws that are below the POD value. Validation of the capability of an NDE procedure requires characterization of the signal and noise response values and the establishment of a useable discrimination threshold. (acceptance criteria for the procedure). The decision threshold level is most often established by comparative measurement to a reference artifacts ("calibration") and is the basis for reproducing the measurement parameters for an NDE procedure. The causal relationship response of the measurement to variation in flaw size is established experimentally by repetitive measurements of flaws of varying size (ideally the relationship is linear or log-linear).

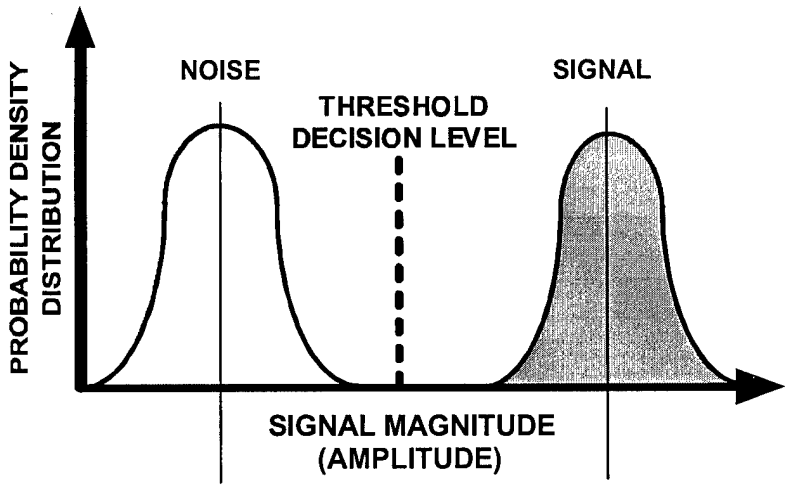

Figure 6. Relationship between measurement signal and background / measurement noise

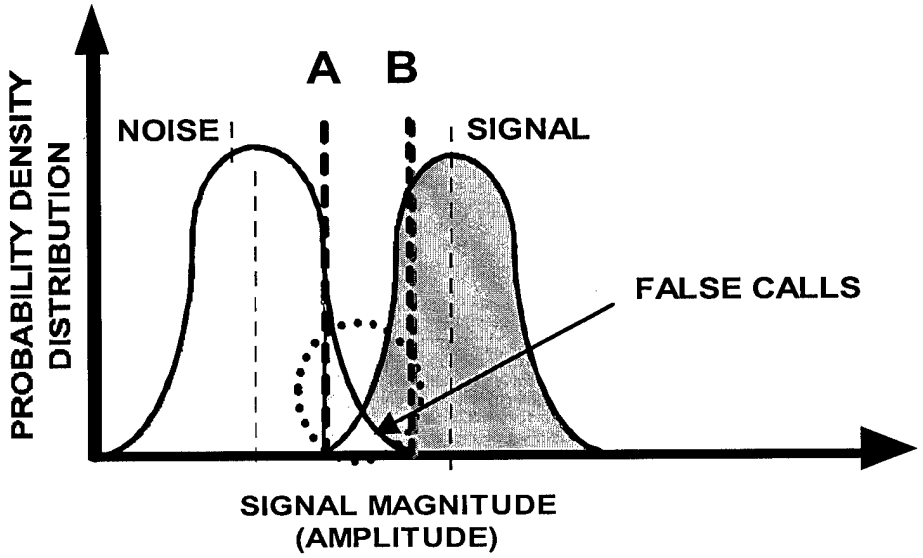

Figure 7. Signal and noise overlap at a small flaw size

The standard statistical model for describing two overlapping Gausian distributions is the log-logistics (log-odds) model that is:

$$\mathrm{PoD}(a) = \frac{\exp(\alpha+\beta\ln a)}{1+\exp(\alpha+\beta\ln a)} \quad \text{or} \quad \ln\left[\frac{\mathrm{PoD}(a)}{1-\mathrm{PoD}(a)}\right] = \alpha+\beta\ln a$$

This may be rewritten as:

$$\mathrm{PoD}(a) = \left\{1+\exp\left[-\frac{\pi}{\sqrt{3}}\left(\frac{\ln a-\mu}{\sigma}\right)\right]\right\}^{-1}$$

where $\mu = \dfrac{-\alpha}{\beta}$ and $\sigma = \dfrac{\pi}{\beta\sqrt{3}}$

Some investigators with similar results also use the lognormal or Weibull model. Both POD methods assume a log linear relationship between increasing signal level and increasing flaw size. This relationship is valid for most NDE modalities when the flaw is large with respect

to the interrogating probe and with those modalities that depend on visual detection such as visual and penetrant methods.

An integrated NDE measurement model (such as that developed for the pulsed eddy current application) may be used to predict output signal levels under varying instrument and operational parameters and may therefore be linked to predict the probability of detection (POD) under varying instrument / operational conditions. The measurement model must also account for "noise" signals such that the threshold discrimination level (acceptance criteria) can be set to detect all measured anomalies without reporting false calls. The "noise" component may be input from models or from experimental measurement data [REF 7,8,9]. An acceptance signal threshold must then be established to provide the basis for "detection" or a' miss in the case of a 'Hit" / "Miss" analysis or as a boundary condition for analysis of discrete signal data. The linked modeling sequences constitute a predictive POD modeling tool. An interim step may be necessary to transform the predicted output to the log linear form that is necessary for the logistics or lognormal POD models. Attention to the transform is especially required for detection of small flaws and for detection involving special boundary conditions, such as an edge at a corrosion damage site.

Basic POD software (log-logistic model) was modified in Microsoft Excel™ Macro [REF 13] form to provide an engineering user tool for analysis of "Hit / Miss" data. The basic software was used as the basis for analyses of all data in the "NDE Capabilities Data Book" [REF 12]. Since different versions of Microsoft Excel™ require different procedures for plotting, specific instructions for three different versions were required. The Microsoft Excel™ Macro method was selected for this software package to provide direct interface with most data in tabular / spread sheet form. This provides a convenient interface to the eddy current measurement model data and to experimental data. The POD Excel Macro is available from D&W Enterprises [REF 14].

The output of the new Macro analysis software is shown in Figure 8, where the threshold a_{NDE} value (by convention) is that point at which the curve crosses the 90-percentile level. The output results are identical to that used in the "NDE Capabilities Data Book". The analysis and plotting are considerably faster than then the basic model and are now able to interface with various version of Microsoft Excel™. Instructions for use of the POD Macro are documented in APPENDIX D. Plots of data from the pulsed eddy current model were not completed due to the requirement for experimentally measured noise data. For purposes of this initial assessment, the noise level is assumed to be at the baseline for the pulsed eddy current model output.

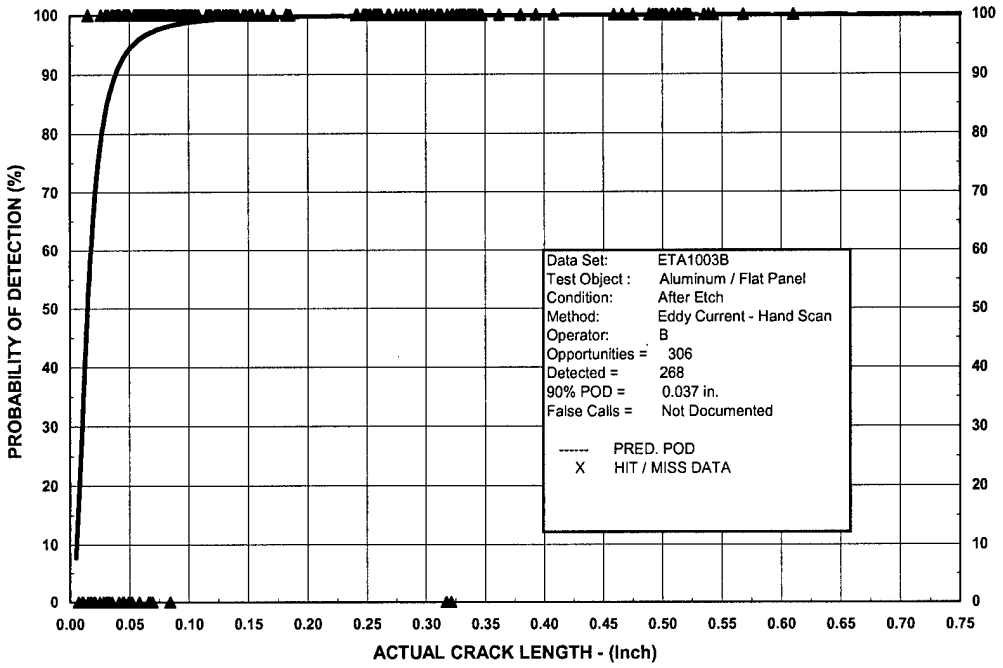

Figure 8. A typical POD curve output from the POD Macro

VI. TECHNOLOGY TRANSFER ANALYSIS AND SUMMARY

A major objective of the project was to assess marketability and transfer of the technology to the commercial sector. Several NDE instrument producers expressed interest in producing an instrument under contract as a research instrument or to customer specific requirements. Such production would include the cost of instrument design specific to Air Force needs and provisions for minimum quantity buy would be included. This is typical of Air Force specific NDE instrumentation that are used in other inspection applications and are used in general Air Force maintenance operations. The same instrument manufacturers would consider licensing and production of a commercial instrument at such time that firm requirements are generated by the aircraft (original equipment manufacturers OEM's) industry and of profitable market can be projected. Although the technology uniquely addresses an Air Force need, commercialization is not recommended at this time. A Phase II program will therefore be delayed to allow for further development of the technology and equally important, to allow for development of engineering acceptance criteria and analysis methods to utilize the measurements made. Requirements for measurement will not be forthcoming until engineering acceptance criteria and analysis methods are developed and generally accepted by Air Force Maintenance, by aircraft manufacturers, and by airlines. The pulsed eddy current measurement technology is still evolving as evidenced by the replacement of the coil with a Hall sensor detector, by the industry evaluation / assessment program with Boeing [REF 16], and by the maturity of the pulsed eddy current instrument design and acceptance test. Major progress in maturation of the technology was provided in the form of the measurement model and the POD macro programs that are necessary for analysis.

In summary, the pulsed eddy current method offers a unique capability for detection and quantification of corrosion damage and gap at the second layer of an aircraft structure. Detection capabilities for slots 0.5 inches long have been demonstrated by experiment and by modeling for an outside skin thickness of 0.160 inch (2024 T3 aluminum). Commercial aircraft skin thickness is nominally 0.037 inch thus a favorable signal to noise ratio has been demonstrated for practical application. Work remains to optimize /balance the detection margin as a function of scanning speed. Two prototype design iterations of the system have been built and are under field evaluation at Boeing. These iterations will be invaluable in addressing application conditions such as rivets, substructure and tear straps. In addition, the capability for measurement of corrosion and gap is expected to be a benefit to the development of acceptance criteria and corrosion analysis / management tools. Further engineering development support are necessary to produce a mature design that can be considered for licensing, instrument production and marketing. It is expected that the instrument design and supporting technology may reach sufficient maturity in the next year to warrant reconsideration for a Phase II STTR program and for licensing, commercial instrument development and marketing.

The tangible outputs of this program are the measurement modeling software that may be marketed by the Center for Nondestructive Evaluation and the Probability of Detection Macro's that are marketed by D&W Enterprises, LTD. Both programs are Copyright © by the developers and marketing options will remain with the developers.

Pulsed eddy current technology has been demonstrated to have potential for detection and measurement of corrosion in the second layer of aircraft structures. Significant progress in understanding the technology and in addressing application conditions has been made under the current project and in conjunction with related, concurrent project funding and support. Work performed under the current program is considered to be a success story but did not progress to licensing and commercial marketing stage during this Phase. It is anticipated that a Phase II STTR program will be pursued pending further development to bring it to a level for consideration of license, instrument development and commercial production. It is clear that the need for acceptance criteria, engineering analysis tools and establishment of requirements for measurement in maintenance operations are required before commercial marketing can be considered. These developments are inter-related, but independent of consideration for further development of the pulsed eddy current technology.

The authors appreciate the support of the Air Force Office of Scientific Research and the data shared by the concurrent industry and FAA programs that have supported pulsed eddy current technology development. The combined efforts and resources were of significant benefit to this program.

REFERENCES

[1] J. C. Moulder, J. A. Bieber, W. Ward III, and J. H. Rose, "Scanned pulsed-eddy-current instrument for non-destructive inspection of aging aircraft," in *Nondestructive Evaluation of Aging Aircraft, Airports and Aerospace Hardware*, SPIE Volume **2945**, 1996, pp. 2-13,.

[2] Aging of U. S. Air Force Aircraft, report prepared by the National Research Council Committee for the U.S. Air Force, NMAB-488-2, 1997

[3] J.L Rudd, UASF Aging Aircraft Program, pp 1-1-1-13, "Aging Aircraft Fleets - Long-term Application," AGARD, Lecture Series, 206, 1996.

[4] The United State Air Force "Structural Integrity Conference", Annual, 1996, 1997, 1998.

[5] The combined FAA, NASA and DOD, "Conference of Aging Aircraft" , Annual, 1996, 1997, 1998

[6] R. Satvelli, J. C. Moulder, B. Wang and J. H. Rose, "Impedance of a coil near an imperfectly layered metal structure: the layer approximation," J. Appl. Phys. **79**, 1996, 2811.

[7] R. Bruce Thompson, "Overview of the ETC POD Methodology", in Review of Progress in Quantitative Nondestructive Evaluation, Vol 18, D. O. Thompson and D. E. Chimenti, Eds. (Plenum Press, NY, in press).

[8] J. N. Gray, T. A. Gray, N. Nakagawa, R. B. Thompson, "Models for Predicting NDE Reliability," Metals Handbook, 9th Edition, Vol. 17, Nondestructive Evaluation and Quality Control (ASM, Metals Park, OH, 1989), pp. 702-715.

[9] W.D. Rummel, "Considerations for Quantitative NDE and NDE Reliability Improvement", in Review of Progress in Quantitative Nondestructive Evaluation, Vol 2, D. O. Thompson and D. E. Chimenti, Eds. (Plenum Press, NY,), 1982, pp. 19-36.

[10] PEC Modeling Software is Copyright © by Iowa State University, Center for Nondestructive Evaluation, Applied Sciences Complex, 1915 Scholl Road, Ames, Iowa, 50011.

[11] A.P. Berens, "NDE Reliability Data Analysis", in the Metal's Handbook, 9th Edition, Vol. 17, p 689, ASM International, 1989

[12] W.D. Rummel and George Matzkanin, NDE Capabilities Data Book, 3rd Edition, Published by NTIAC, Austin, TX, 1997.

[13] Rummel, Ward D., Paul H. Todd Jr., Sandor A. Frecska, and Richard A. Rathke, The Detection of Fatigue Cracks by Nondestructive Testing Methods, NASA CR-2369 February 1974.

[14] "Excel 95, 97 and 2000" are Trademarks of the Microsoft Corporation, Redmond WA.

[15] "Probability of Detection (POD) MS Exel Analysis Macro's', Version 3.0, is available from D&W Enterprises, Ltd, 8776 W. Mountainview Lane, Littleton, CO 801125.

[16] Boeing Aircraft Company, Seattle, WA.

APPENDIX A

CONCURRENT WORK AND DATA DEVELOPED UNDER A FEDERAL AVIATION ADMINISTRATION FUNDED PROGRAM

Scanning Pulsed Eddy Current for Aviation Applications

- Investigation Team:

  J. R. Bowler, Center for NDE, ISU

  M. J. Johnson, Center for NDE, ISU

- Students:

  Y. Huang, Graduate Student in Electrical and Computer Engineering

- Industry Partners:

  D. Moore, AANC, D. Wilson, B. Jappe, Boeing Long Beach, S. LaRiviere, J. Thompson, R. Novak, Boeing Seattle, J. Skramstad, NW Airlines

Technical Monitor: Dave Gallela
Grant/Contract Number: DTFA0398D00008

Objectives

- To transition the pulsed eddy current (PEC) technology from the developer to the user community and to facilitate its rapid introduction and acceptance in commercial aviation.

- To develop and demonstrate new PEC-based detection and characterization methods for small fatigue cracks in multi-layered aircraft structures.

- To transition the PEC methodologies for corrosion and crack detection in cooperation with industrial partners.

Progress to Date

Sept 98	Program Initiation
Jan 99	Delivered SPEC I system to Boeing, Renton for evaluation by Lloyd Schaefer and Jeff Thompson.
May 99	Carried out hardware and software upgrades to Boeing system.
Jul 99	Performed comparisons of PEC data with conventional EC (NDT 19e).
Nov 99	SPEC II (Laboratory System) design completed
Apr 00	Laboratory System functioning
Sep 00	Design of Field System complete
Nov 00	Development of Field System

Technical Details

Summary of Progress

- System has been redesigned to improve performance
  - ➢Hall-sensor gives improved depth penetration
  - ➢Response is insensitive to temperature changes
  - ➢Software upgraded to Win-32
- Analysis and processing
  - ➢Removal of stringer, tear-strap or edge signals
  - ➢Full waveform now stored for off-line processing

Technical Details

Performance

- Hall-sensor gives improved depth penetration

  - Induction coils actually measure the rate-of-change of field and so are less sensitive at low frequencies.
  - Hall sensors measure the magnetic field directly and are sensitive at low frequencies.
  - Hall element sensors enable the detection of deep flaws.
  - The Hall-element sensors have good spatial resolution.

Technical Details

Performance

- **Detection capability: less than 4% material loss in ¼" Al plate.**
- **Depth penetration can be increased, at the expense of measurement time, using a larger probe.**

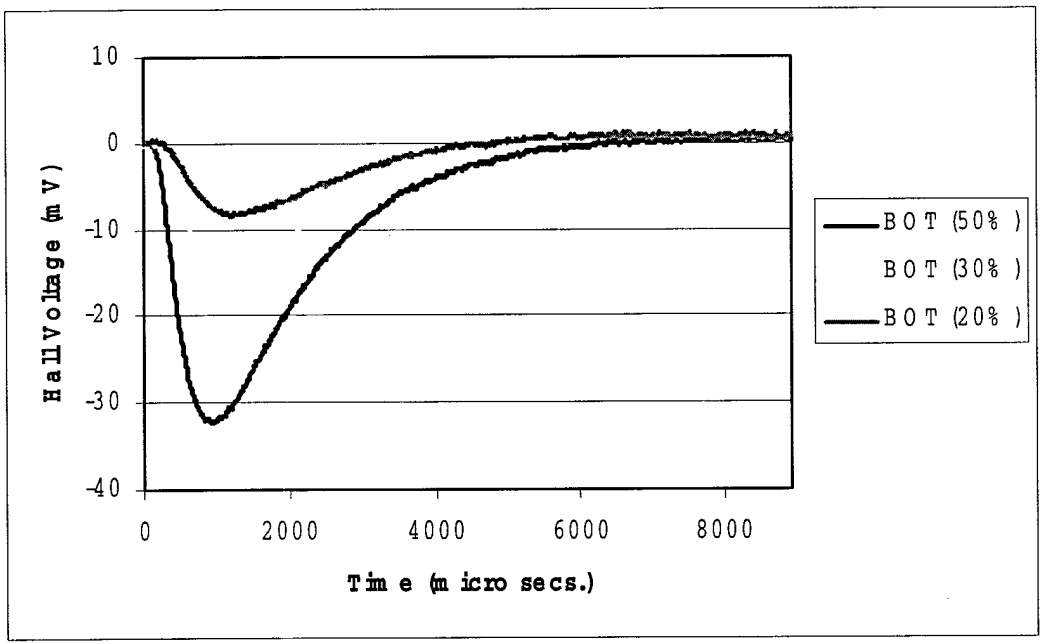

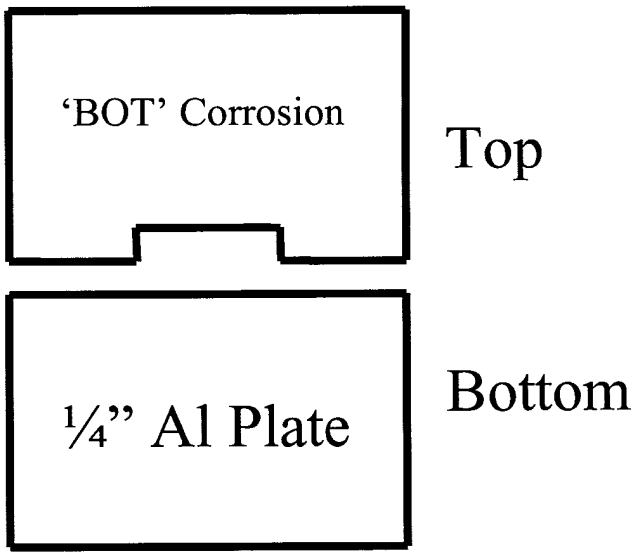

Technical Details

Depth Penetration

To investigate depth of penetration trials were conducted on a slot in a thin aluminum plate placed under various unflawed plates of different thickness.

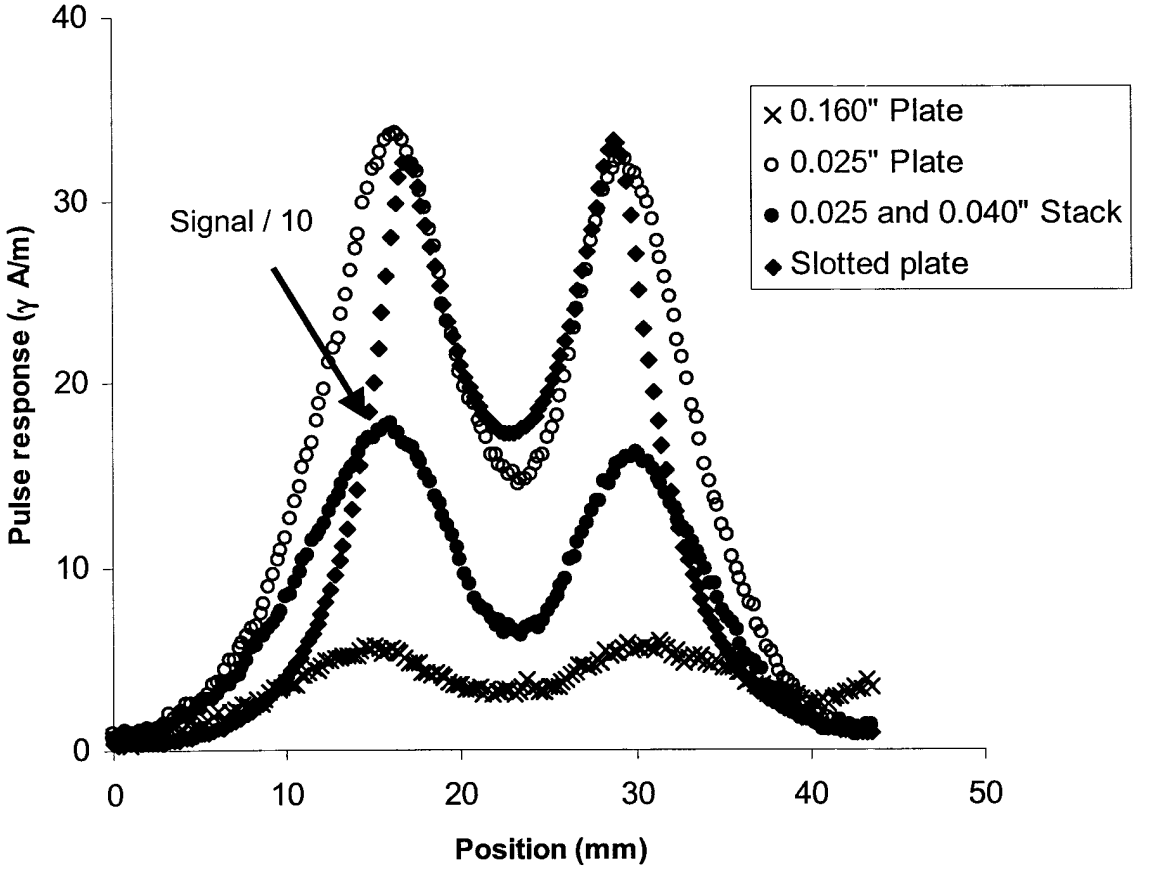

Slot length: **0.5”**

Slot width: **0.015”**

Slot plate thickness: **0.025”**

Slot plate conductivity: **34.5% IACS**

Technical Details

Performance

- Response is insensitive to temperature

Latest scans are free from thermal drift. The previous version of SPEC was plagued by drift problems which manifested themselves as a gradients superimposed onto the C-scan images.

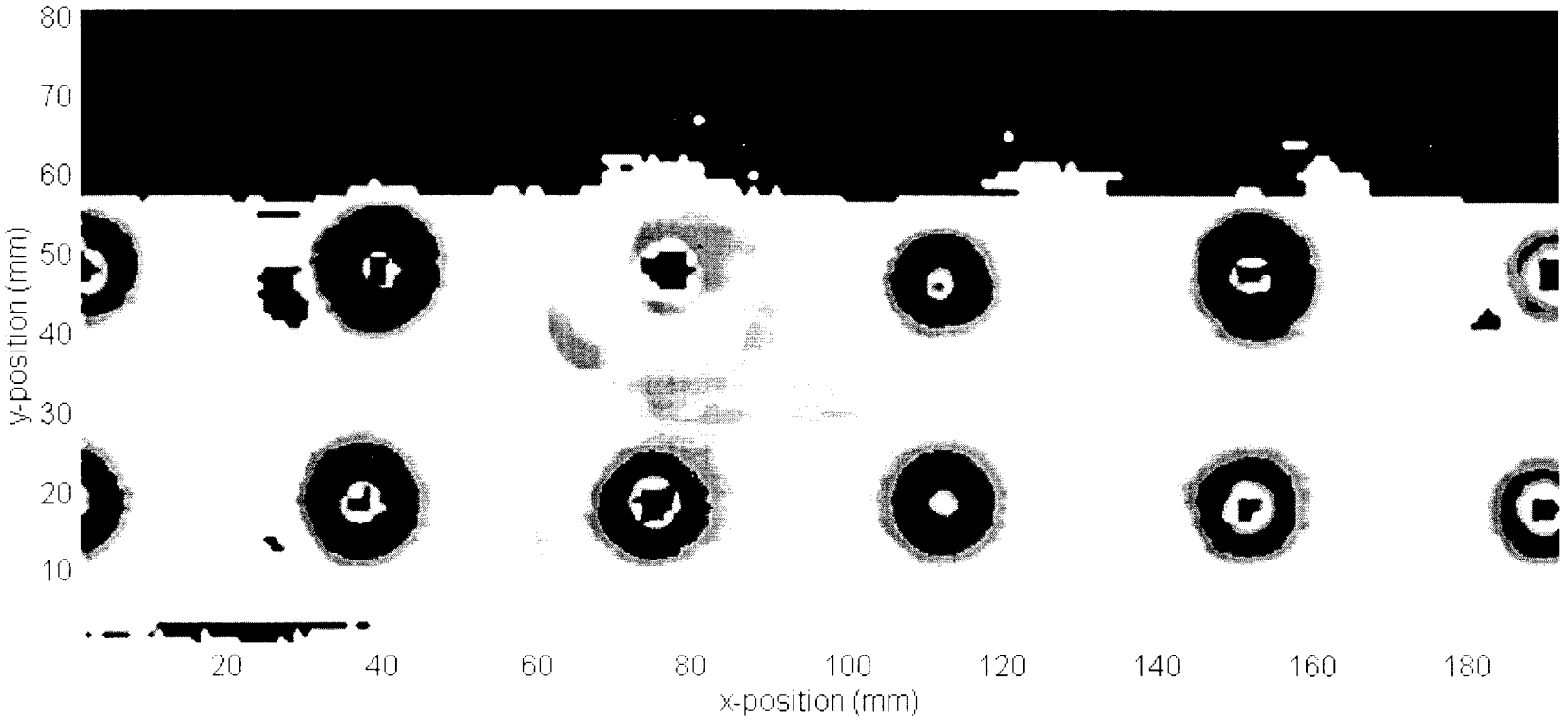

Technical Details

Graphical User Interface

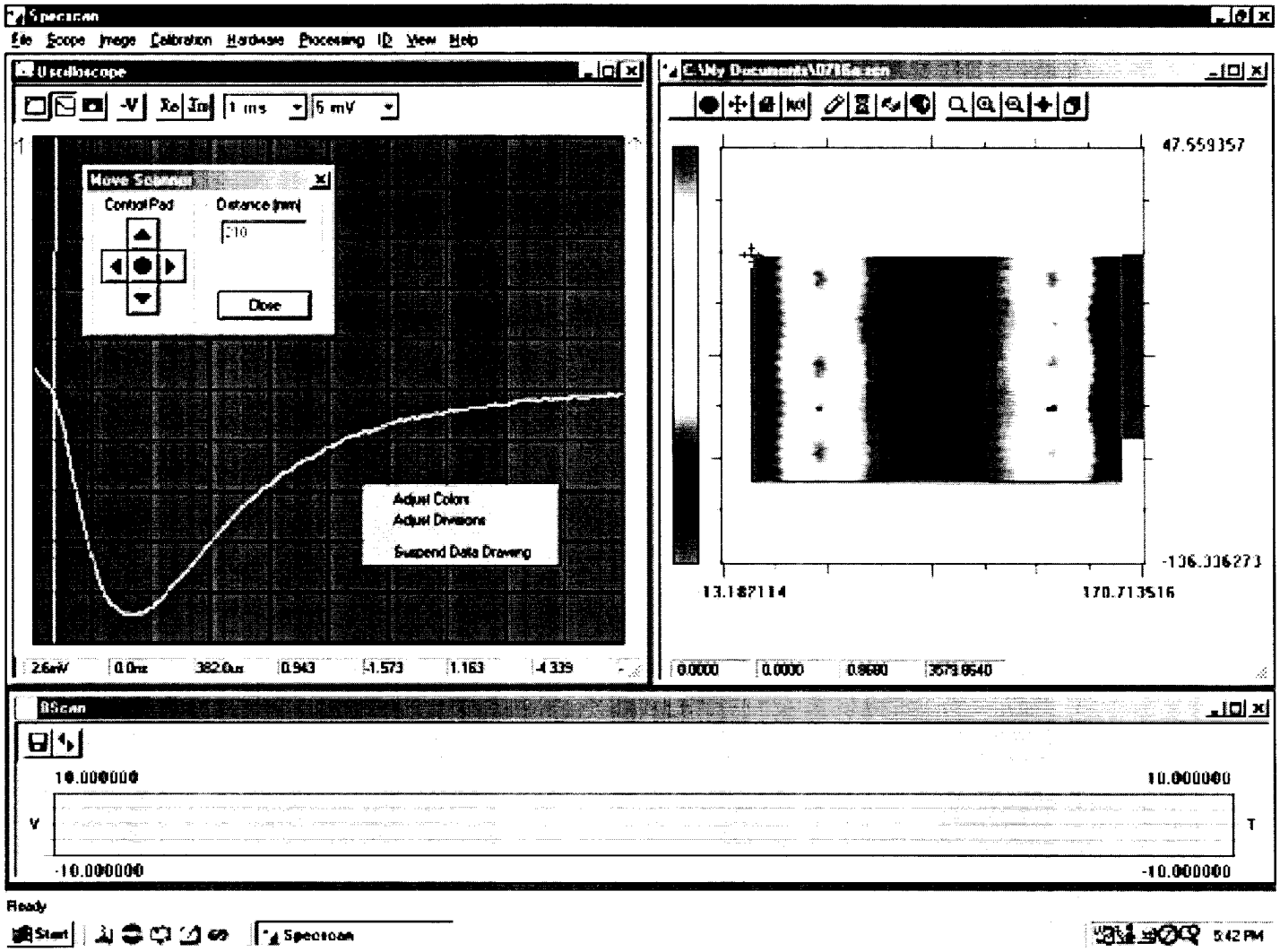

Technical Details

Analysis and Processing

- SPEC I stored only peak height and the zero-crossing time.
- In SPEC II the entire signal is stored which allows more advanced processing of the signals off-line.
- An edge-subtraction procedure is performed for removing signals due to stringers etc.

Technical Details

Edge Subtraction

Edge subtraction enables flaws around stringers or other multi-layer features to be viewed more clearly.

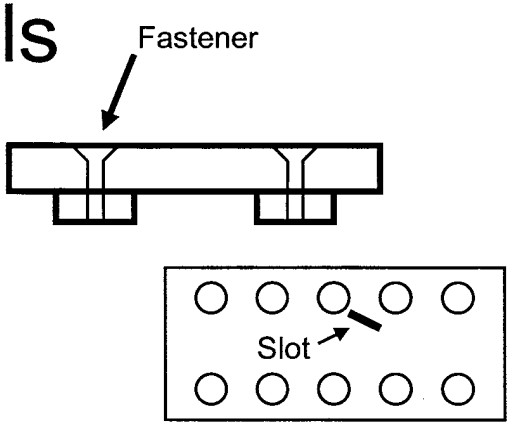

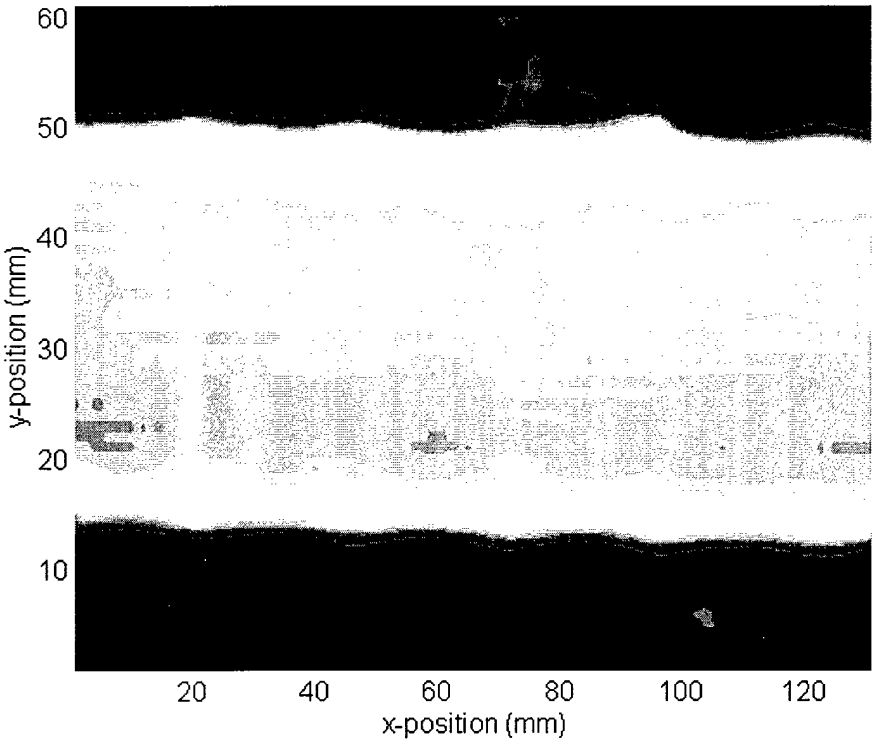

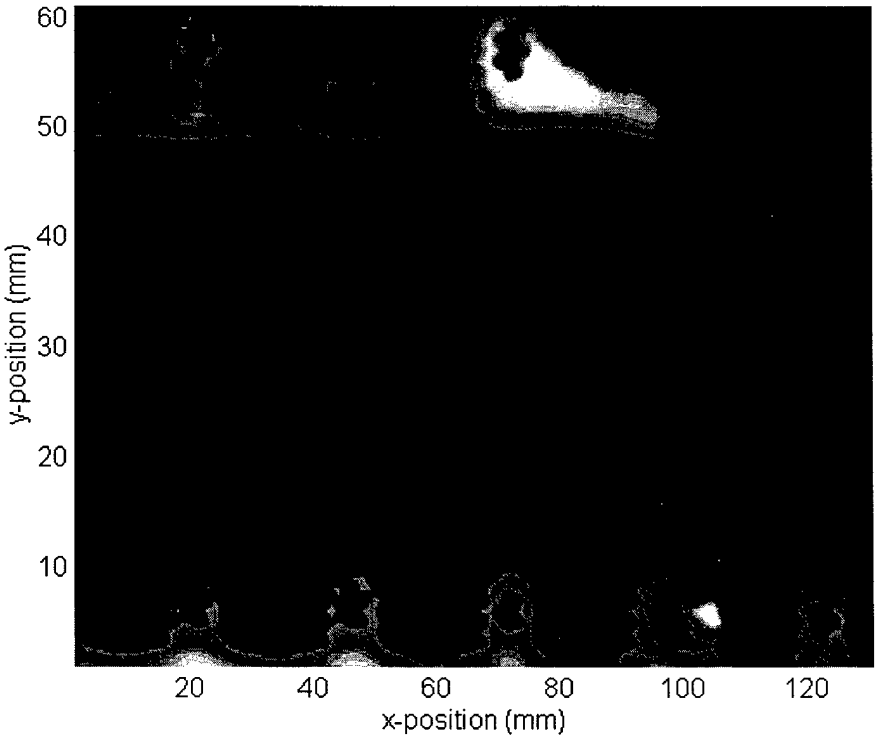

Technical Details

Edge Subtraction

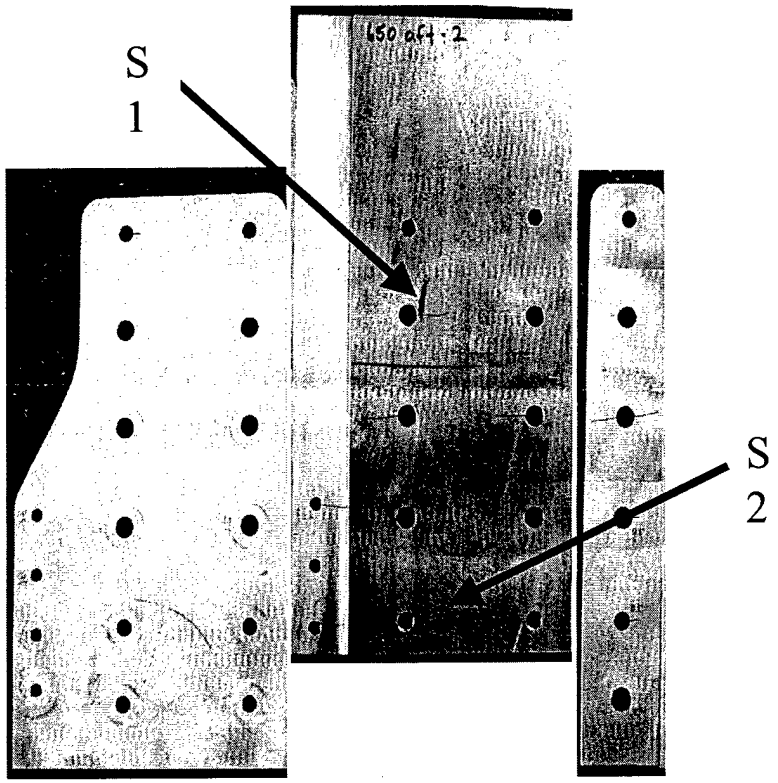

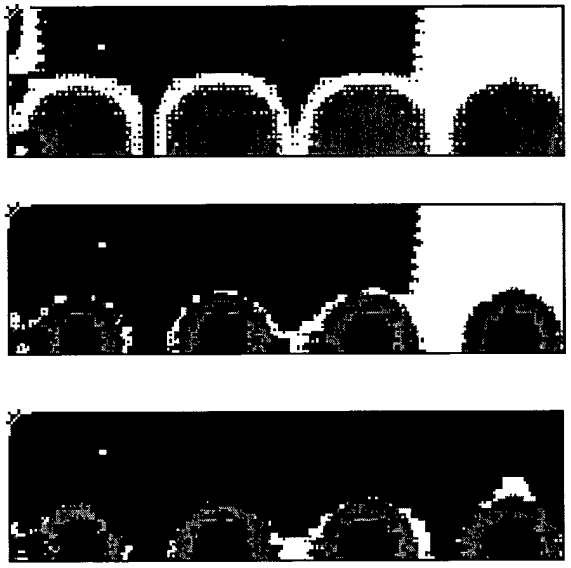

S2 is not visible due to significant changes in layer structure. A second reference measurement could be made which would enable S2 to be imaged.

Technical Details

- Full waveform now stored for off-line processing

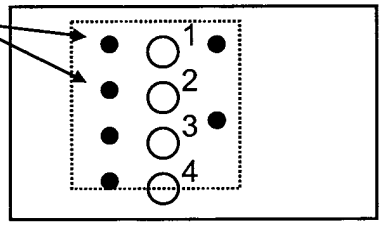

Material loss 1: 5%
2: 10%
3: 15%
4: 20%

Depth Gage

Without Air Gap

Surface

With 0.01" Air Gap

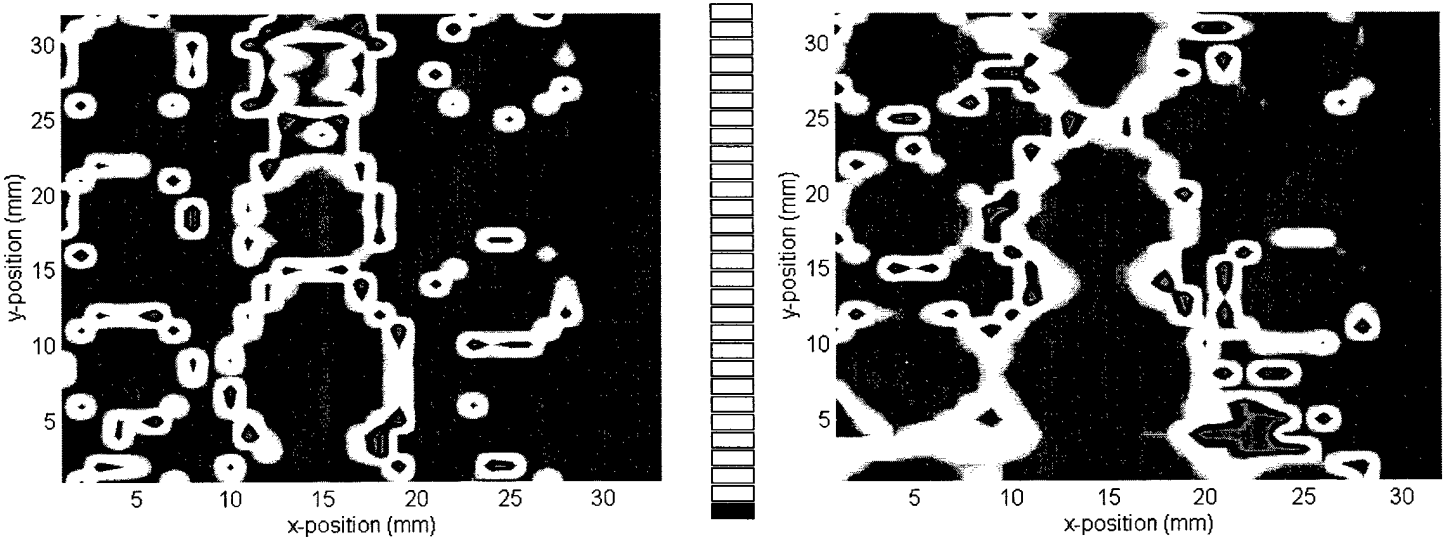

Far side

Technical Details

"Time-of-flight" Crack Imaging

Field migration by diffusion: depth ~ √(time of arrival)

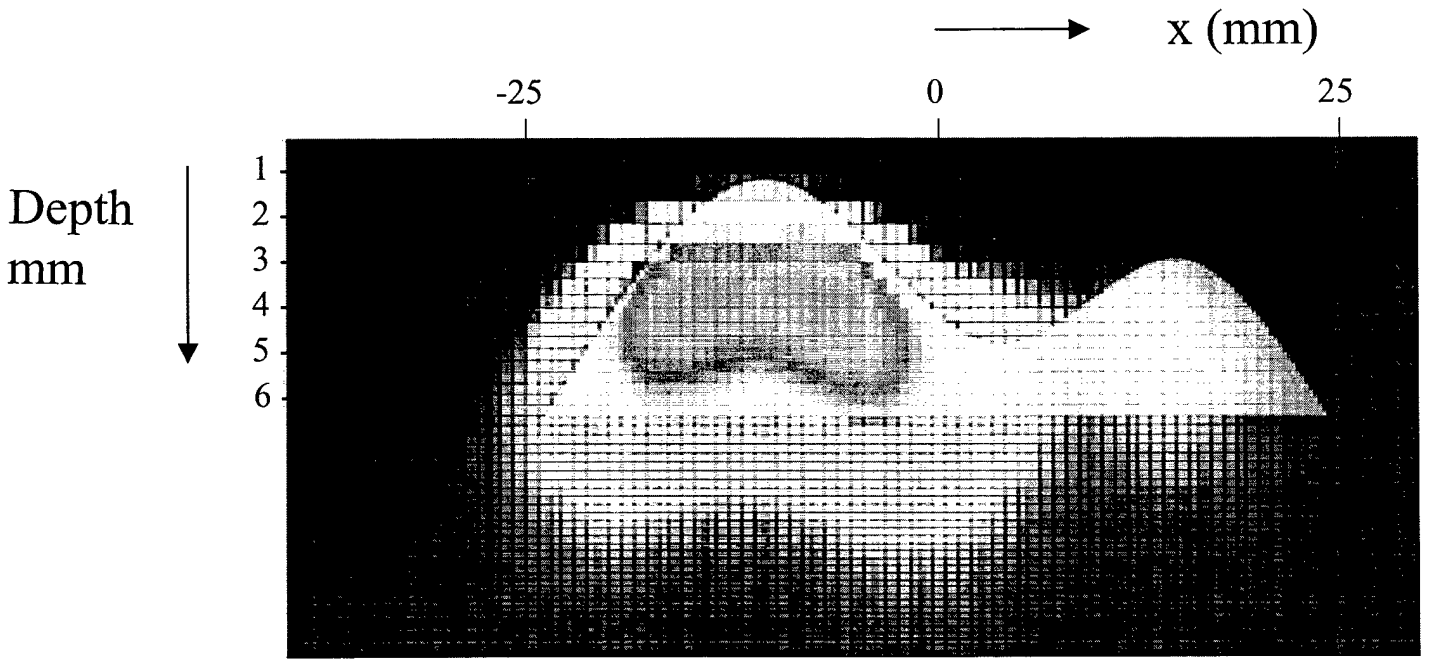

Aviation Safety Impact

Contacts with industry have indicated that the technology offers crucial advantages over existing equipment:

- **SPEC can be used to locate flaws in structures that have a complex geometry**
  - Using edge subtraction algorithms
  - Using new signal analysis and interpretation procedures
- **Capable of compensating for changing liftoff**
  - Using features in the signal that vary only with liftoff
- **SPEC can be used to distinguish between corrosion and coincident air-gap**
  - Using inversion algorithms on the pulse signals

Plans for the Future

Dec 00	Complete construction Field System
Jan 01	Deliver Field System to Boeing, Renton for evaluation by Ronald Novak.
Jan 01	Deliver Field System to Boeing, Long Beach, CA.
Feb 01	Initiate plans for field testing at Renton and Long Beach.
Mar 01	Complete design of new probes based on results of field testing.
Sept 01	Complete field testing, beta-site testing and final report.

Summary

- The SPEC laboratory system has been used for slot and corrosion detection, some preliminary performance results have been obtained.
- Results indicate that depth-penetration and performance will be good.
- The signals can be analyzed in a manner that allows depth profiling.
- Two field versions of the system will be delivered to Boeing in January for a more complete evaluation.
- Based on feedback from Boeing, new probes will be developed to optimize performance for certain problems.
- The Laboratory System will also be used in the AANC's structured corrosion experiment.

APPENDIX B

INDEPENDENT REPORT

MEASUREMENT MODEL DEVELOPMENT

John R. Bowler

Iowa State University, Center for Nondestructive Evaluation
Applied Science Complex II, 1915 Scholl Road Ames IA 50011-3042 USA
Tel. 515 294 2 093, Fax 515 294 7771

Integrated Quantitative Non-Destructive Evaluation and Reliability Assessment of Aging Aircraft Structures

Measurement model development for reliability assessment of pulsed eddy-current non-destructive evaluation

John R Bowler

Professor of Electrical Engineering and Senior Scientist,
Iowa State University Center of Nondestructive Evaluation
E-mail: jbowler@iastate.edu

Preface

This research reported here is motivated by the need to keep an aging fleet of military aircraft at a safe state of readiness with limited capital resources. A key requirement is for the development of flexible inspection technologies that can be adapted to deal with a wide range of operational problems on a variety of aircraft each of which have their own failure mechanisms. Typically such problems are unforeseen and require new inspections to be devised and implemented at short notice. This program seeks a cost effect way of designing new inspections in response to operational needs and to validate the reliability of those inspections in order that aircraft are maintained in a safe condition for their full or extended service life.

The need for cost-effective assessment of aircraft inspection reliability is being met in this program by the development of computer-based tools for the evaluation of flaw detection probabilities. In addressing the need, we have focused on the reliability of pulsed eddy-current methods for the detection of corrosion in aircraft. Using a new approach for reliability assessment, a measurement model simulates the test conditions and sensor flaw interactions, replacing a costly and lengthy process of sample preparation and laboratory testing. The approach will allow the performance of inspections to be designed, compared and optimized using a technology that is flexible, rapid and economic.

Contents

Chapter 1

Requirements, Aims and Objectives

1.1 Aims

The general long term aim of the present program, guiding the work in both Phase I and Phase II, is to develop quantitative inspection methods that are integrated with a set of tools and procedures to provide performance guarantees for first time users and permit new inspections to be evaluated in terms of their performance reliability. Inspection reliability is quantified using estimates of the probability of detection (POD) and is dependent on defect parameters and measurement conditions.

The work program has been subdivided into tasks design to achieve a number of specific, well defined objectives in support of the overall program aim. Tasks and Phase I objectives are discussed in the next section.

The tools developed to assess inspection performance and reliability are geared specifically to an emerging technology; pulsed eddy-current testing. A pulsed eddy-current inspection system has been developed in an earlier AFOSR program at the Center for Non-destructive Evaluation, Iowa State University. With additional support from the Federal Aviation Administration, the technology has reached the point at which beta test equipment is being designed and constructed for delivery to users in the civil sector. In Phase II of the current program, an advanced inspection system will be designed and built for application to military aircraft. In Phase I, the focus has been on the development of software to assess performance reliability and to simulate measurements of corrosion damage.

The central aim of Phase I is to develop a measurement model, validated using experiment data and coupled with a basic POD evaluation capability to provide a reliability metric for corrosion damage assessment on aircraft. A schematic representation of data and model priorities is shown in Figure 1. Inputs to the measurement model are flaw and inspection parameters including physical parameters defining the sensor properties, the flaw size, shape and location together with relevant material parameters. Outputs are the flaw dependent probe signal response as a function of probe position, frequency in the case of a time-harmonic excitation or time in the case of a transient response. The calculated signal is used, together with empirical data on the variability of the inspection parameters, to estimate the probability of detection of a given flaw and thereby assess the

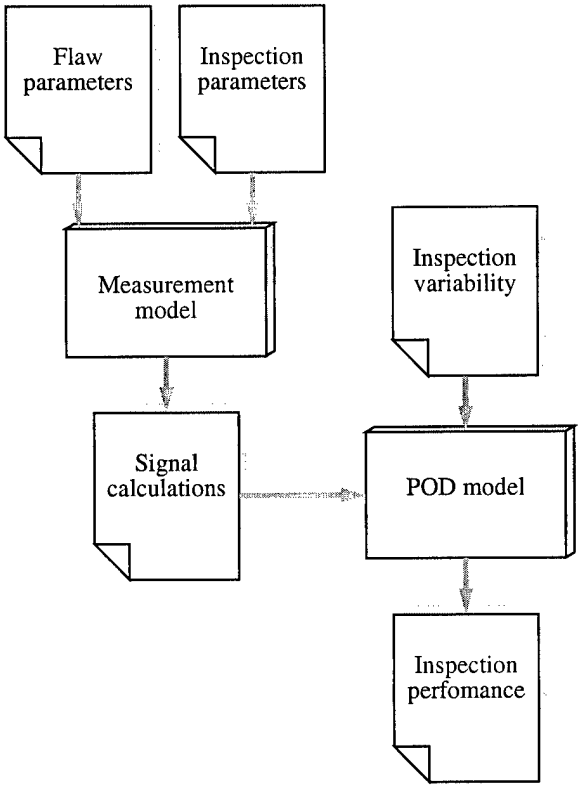

Figure 1.1: Schematic diagram showing the measurement and POD models together with data input/output files and documents.

inspection performance.

Although the value of reliability metric for management of nondestructive inspection (NDI) is widely recognised, traditional methods of establishing detection probabilities through multiple sample preparation and extensive testing can be prohibitively expensive and/or impractical. Substitution of a measurement model is a cost-effective rapid-response alternate to the traditional approach [1]. Clearly, it is vital that evaluations of sensor output, here performed through analytical and numerical treatment of the field equations governing probe flaw-interaction, are accurate. Ultimately it is necessary to simulate realistic part geometries taking account of common structural features of an aircraft, such as installed fasteners, lap joints and spars. However, initial progress has been made by analyzing simply geometrical forms for the test pieces. In Phase II, the measurement model will be generalize to deal with complex structures.

1.2 Program Tasks and Objectives

The proposal for the present program identified three Phase I Tasks in line with the need to develop quantitative NDE capabilities for life-cycle management of corrosion in aircraft structures:

1. Development of quantified flaw detection requirements and acceptance criteria.

2. Development of measurement modeling tools to enable prediction of output signal levels with different probe designs and inspection conditions.

3. Development and linking of measurement output to a predictive POD model to support NDE engineering especially in facilitating the introduction and validation of new procedures.

Here the outcomes of Task 2, the measurement model for performance and reliability assessment is described.

Measurement models can be constructed using a number of different approaches which can be classified as synthetic or deterministic. In the synthetic approach the model is a secondary data source acting to integrate, organize and process data delivered to it from a primary source. Statistical techniques or artificial neural networks fall into this category because they require extensive input of empirical data in order to be able to regenerate probe signals in agreement with laboratory experiments or field inspections. It has already been emphasized that reliance on sample preparation and laboratory testing for controlled sensor data is expensive and time consuming, severely limiting the ability to quantify reliability. Statistical or artificial neural network methods relying solely on empirical input data suffer from the same resource limitations. Furthermore they are lacking a genuine predictive capability and therefore cannot be used beyond the limits of the primary data.

Methods that ignore the physical relationship between probe and defect can be parameterized or trained to conform with the physical realities using a deterministic model but then the latter is a prerequisite and takes priority. However, the availability of a deterministic model does not render the synthetic methods redundant since these may have advantages such as speed of response and ease of use.

Eddy-current signal calculations have been carried out in this program using physical (deterministic) models based on electromagnetic field theory. Limited testing of the output via comparisons with experiment are necessary but only a few experiments are needed for validation purposes and this process is therefore not expensive. This approach is the only effective solution that avoids the cost of multiple sample preparation and extensive empirical testing. A new measurement model based on the physics of the probe-defect relationship has been developed for Task 2. The theoretical study of the interaction of eddy current probe and flaw yields a set of equations that are solved numerically to give the electromagnetic field in the presence of corrosion damage, the corrosion being represented as a non-conducting region embedded in a conducting region. The field equations have been translated into an efficient computer code using numerical methods and solutions generated from input data which describe the test conditions.

The theory of transient electromagnetic fields has been used to evaluate pulsed eddy-currents (PEC) in conductors. By computing numerical solutions of the field equations, probe signals due to localized regions of corrosion have be determined for the first time in this study as a function of probe position and time. Previous theoretical studies of pulsed eddy-current nondestructive evaluation have represented corrosion as an infinite layer [2, 3, 5]. In another earlier study, pulsed eddy-current interactions with cracks have been predicted and compared with experimental measurements [4]. The new results presented

here, however, are derived from a more flexible model than has been used previously. The model makes use of a regular three-dimensional array of volume elements which can be assembled in a form that represents either a crack or a finite region of corrosion. Simply by assigning conductivity values to the volume cells in a three dimensional grid, a corroded region arbitrary shape can be represented, including for example an approximation of a conical corrosion pit.

Task 2 entails the following objectives which have been accomplished with the aid of transient eddy-current measurements models:

1. An existing transient eddy current code has been modified for predicting signals due to corrosion. Parametric studies of probes have been carried out find probes with good signal sensitivity. The corrosion for this study was modeled as a uniform infinite non-conducting layer.

2. Noise and signal variability parameters have been measured for a pulsed eddy-current test instrument and scanning system.

3. A response model has been developed to determine signals due to finite regions of corrosion.

4. Interface the measurement model to the POD code.

5. This report has been produce.

The results from Task 2 are reported in next chapter. To conclude this chapter, the prospects for finding quantitative measures of corrosion damage are reviewed below.

1.3 Quantitative Corrosion Assessment

The rough location of corrosion damage beneath an aircraft skin can be identified directly from raw eddy-current data, using for example, false color c-scan images. The data needed to generate such images is acquired by scanning the surface of the aircraft using an eddy-current probe while recording transient or time-harmonic field measurements. It is relatively easy to get an approximate idea of the lateral position of the corrosion from the images but there is a need to estimate material loss and to determine the depth of corrosion damage in a layered structure. This information is not readily available from the c-scan images. The task of locating the in-depth limits of localized corrosion is an important element in the planned Phase II program and can be accomplished with the aid of the measurement model developed in Phase I.

The simplest model of corrosion treats the test piece as a series of uniform layers stacked on top of one another. The parameters of the structure, the conductivity and thickness of the layers, has been found from pulsed eddy-current data by parameter fitting [5]. However, the infinite layer model does not give realistic representation of a localize and irregular region of corrosion damage. For the case of crack inversion, it has been shown that irregular shapes can be reconstructed using eddy current data by

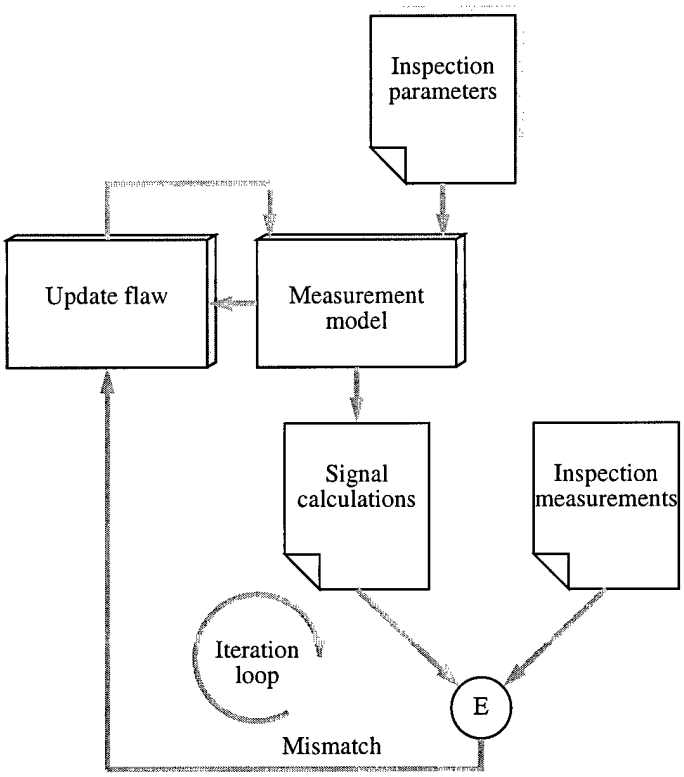

Figure 1.2: Schematic diagram showing the measurement model in an iterative inversion process.

applying a least square optimization scheme that relies on a fast and accurate forward measurement model to predict probe signals [6, 7]. By adjusting flaw parameters iteratively until calculated signals agree with measurements, Figure 1.2, the boundaries of the crack was found. Therefore we can be reasonably confident that a similar approach would determine the limits of the corroded region from eddy-current probe data. The general principles for accomplishing this task have been established by Norton and Bowler for time-harmonic eddy-current data [8] but it is not difficult to extend these principles to deal with transient fields.

Implementation of the inversion procedure for the quantification of material loss due to corrosion using pulsed eddy-current data will be set as a Phase II objective. This objective will be accomplished with the aid of a measurement model that can calculate pulsed eddy-current signals due to local regions of material loss and has been developed in Phase I.

Chapter 2

Simulation of Pulsed Eddy-Current Probe Response due to Corrosion

2.1 Introduction

In order to quantify material loss due to corrosion using eddy-current techniques, advances are needed in inspection performance and data analysis. Fortunately these advances are emerging with the use of new field sensors and measurement methods such as pulsed excitation or remote field methods. Laboratory tests conducted at the Center for Nondestructive Evaluation at Iowa State University show that a 2% material loss could be reliably detected under laboratory conditions using pulsed eddy-currents. For conventional eddy-current techniques, by comparison, the detection limit is more than 10% material loss due to simulated corrosion in lap joints at a probability of detection of level 90% [10].

In transient eddy-current inspection, a current pulse in a coil excites a time-varying electromagnetic field which induces current in a conducting test piece. As this pulse migrates into the material it is broadened by dispersion and perturbed by discontinuities in the conductivity and permeability of the conductor. Sub-surface defects disrupt the field causing a perturbation to migration back to the surface. Above the conductor, it can be observed as a transient signal in the time domain, either as an electromotive force (emf) in a pick-up coil, or as a signal produce by a solid state field sensor such as a Hall probe or magnetoresistive sensor. A clear transient signal, measured with the probe remote from flaws or structural features such as fasteners, is typically used as a reference which is subtracted from all other signals. The difference signal contains flaw information, the fastener signal or indeed any indication which differs from the reference signal. The transient is broad band, carrying information from a wide frequency spectrum in contrast to a time-harmonic excitation which yields information only at a single frequency.

Eddy-current inspection is effective for detecting surface or near surface cracks and corrosion in conductors. Because induced currents in a plane structure flow roughly parallel to the interfaces, cracks that are predominantly perpendicular to the surface are readily detectable, the response being related to the area of the crack face. Corrosion in aircraft structures, such as exfoliation corrosion and corrosion in lap joints, tends to emerge at the interfaces between the plates that make up the structure. Eddy current

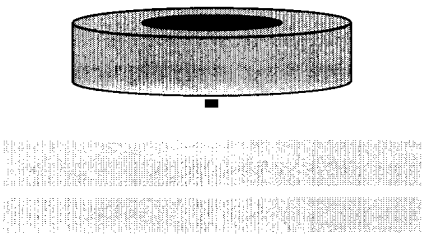

Figure 2.1: Hall sensor mounted on the axis of an excitation coil.

measurements are affected by the change in conductivity caused by decomposition of the metal but the presence of corrosion is not easy to detect at the early stages due to the small perturbations of the induced current.

2.2 Measurement Model of Pulsed Eddy-Currents

In order to assess the capabilities of eddy currents for detecting and characterizing corrosion, the uniform layer model has been used as an idealized representation of corrosion attack between plates. The probe signal is initially calculated for the frequency domain using analytical formulae and then transformed to the time domain using a fast Fourier transform.

In experiments on a simple layer structure, a series of electromagnetic field pulses were induced in the specimen by passing a square wave current through an excitation coil. Transient fields interact with the material and with the non-conducting regions between plates giving rise to a field perturbation which migrates to the surface. The near surface field is measured as a function of time using a Hall sensor, Fig. 2.1. The pulsed eddy-current layer model has been evaluated by comparing predictions with experiment, Figure 2.2. The results show that three distinct transient signals are found depending on whether the air gap between two plates is due to loss of material from the top plate, loss of material from the bottom plate or simply an increase in plate separation[2].

The layer model is adequate for basic probe optimization studies and for finding an upper bound to the probability of detection of a region of corrosion. However it is limited because it cannot be used to compute the effects of localized corrosion damage. In order to perform such calculations for finite pockets of material loss, a new volume element code has been developed. This calculates probe signals directly in the time domain making use of an integral equation with a time-domain kernel [9]. The volume element approach uses the same kernel as one previously used for boundary element calculations and produced the same results when used to simulate the effects of a subsurface crack, Fig. 2.3.

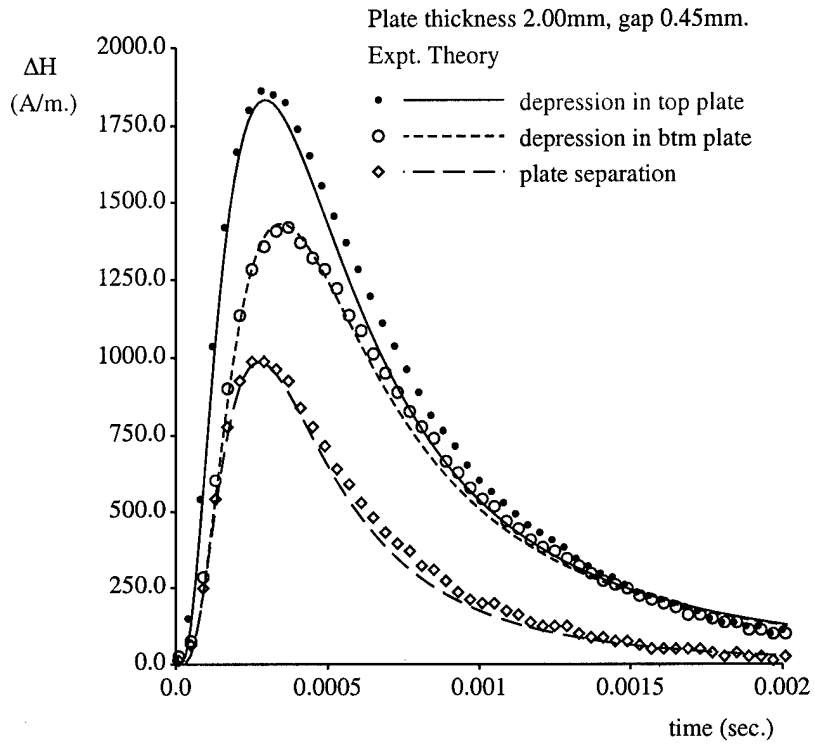

Figure 2.2: Comparison of prediction of a layer model of corrosion with experiment.

2.3 Phase I Accomplishments

The accomplishments below correspond to the objectives given in Section 1.2.

2.3.1 Investigation of Probe Sensitivity

The sensitivity of probes have been compared using on the basis of signal to noise ratio. A probe containing a Hall sensor gives a magnetic field measurement, H, (in A/m) normalized to the excitation coil current. In general, the axial length and the inner radius of the coil is small for optimum sensitivity. The coil lift-off (height of the base above the work-piece) should be as small as possible and the Hall sensor placed as close to the surface of the work-piece as possible on the coil axis. The sensor is supplied in an encapsulated dual-in-line package whose size constrains the probe and coil lift-off. It was concluded that the probe dimensions for best performance are those given in Table 2.1.

2.3.2 Noise and signal variability

Quasi-random background noise levels for the above probe was approximately 25 A/m per Ampére of coil current whereas signal variability (standard deviation) was approximately 100 A/m, mainly due to variations of lift-off (i.e. inconsistency in the probe-workpiece

Table 2.1: Coil Parameters.

Outer radius	10.0 ± 0.05 mm
Inner radius	2.50 ± 0.01 mm
Axial length	2.80 ± 0.01 mm
Nominal lift-off	0.80 ± 0.01 mm
Number of turns	1000 ± 1 mm

contact). The signal variation compares with the typical flaw signal levels shown in figure 2.2 for a material loss of 22.5%. Note that a 1% material loss corresponds to a signal level of 80 A/m which is about three times the noise level. This is roughly the limit of resolution of material loss.

Signal variability or lack of repeatability is mainly dependent on scanning conditions especially the positioning of the probe on the surface of the work-piece. The main cause of the lack of repeatability in the signal is probe lift-off or probe tilt. Assuming the signal variability is due to a lift-off only, it is possible to calculate the lift-off variation which give rise to the observed variation of the signal. In this way the lift-off variation of 0.15 mm was inferred.

2.3.3 Response Model for Localized Regions of Corrosion

The measurement model for calculating the probe response due to local pockets of corrosion of arbitrary shape is described in Chapter 3.

2.3.4 Calculation of Probability of detection

A flaw is said to be detected or detectable when the signal it produces v, exceeds a given threshold, v_t. The threshold level is chosen as a compromise between maximizing the probability of detection, which means v_t should be low, and minimizing the number of false calls which requires a high value. The threshold can be calculated from a statistical analysis of the observation data based on, for example, a tolerable level of false calls, but for present purposes we shall simple set the detection threshold at three times the noise level. This seems to be a satisfactory criterion for most purposes.

Repeated measurement produces a distribution of values of the signal v about a mean value say $\bar{v}(x)$, with a standard deviation of σ_v. Assuming this distribution is normal (Gaussian), the probability that a given signal for a flaw of size x exceeds the threshold and therefore satisfies the criterion for detection, is given by

$$\begin{aligned} p(x) &= \frac{1}{\sqrt{2\pi}\sigma_v}\int_{v_t}^{\infty} \exp[-(v-\bar{v}(x))^2/2\sigma_v^2(x)]dv \\ &= \frac{1}{2}\mathrm{erfc}(V) \end{aligned} \tag{2.1}$$

where $V = (v_t - \bar{v}(x))/\sigma_v$ and erfc is the complementary error function.

It is reasonable to suppose that the mean value of the observation is approximated by the model prediction for a given flaw of characteristic dimension x. Applying the layer

model to the calculation of POD, with x representing the reduction in plate thickness due to loss of material, the corresponding detection probabilities are shown in Fig. 2.4 for cases where the first layer plate is 2 mm and 4 mm respectively. .

2.4 Volume Element Measurement Model Description

The model input is a set of inspection parameters used to characterize the physical conditions of an idealize inspection. These parameters, which include the probe dimensions, the material properties of the part and the flaw dimensions, are used to calculate the sensor probe response to a flaw, such as a region of corrosion. The flaw signals, the variability of the input parameters, noise sources and the detection threshold are to be combined in a probability of detection model to determine inspection performance.

An eddy-current probe responds to the loss of conducting material due to corrosion but it also detects probe lift-off changes, fasteners and other structural features of the aircraft. In order to take account of these effects, the measurement model has the capability of representing general three-dimensional objects. However, the time taken for the calculations is kept within reasonable bounds. In developing a modern three-dimensional electromagnetic field code, much of the software engineering effort is devoted to reducing the computation cost of the calculation.

Initially, the model has been used to represent a finite pocket of corrosion in an otherwise uniform plate. However the approach taken is quite general and can be adapted to accommodate fasteners and lap joints etc. without excessive computational cost. These features will be included as part of the Phase II extensions. The probe signal is evaluated from the electromagnetic field in the part, the field being calculated using a new volume element method based on recent advances in time-domain electromagnetic theory [9]. A region of corrosion is represented as a non-conducting or partially conducting zone of arbitrary shape constructed using volume elements.

The measurement model code determines the eddy-current field in the part using a matrix solver. This is a three-stage calculation in which matrix elements are calculated in the first stage and in the second, the field of the probe is determined. In the third stage, the field in the flaw is found by solving a matrix equation and the probe signal calculated from the solution. Details of the field analysis and numerical method are given in Chapter 3.

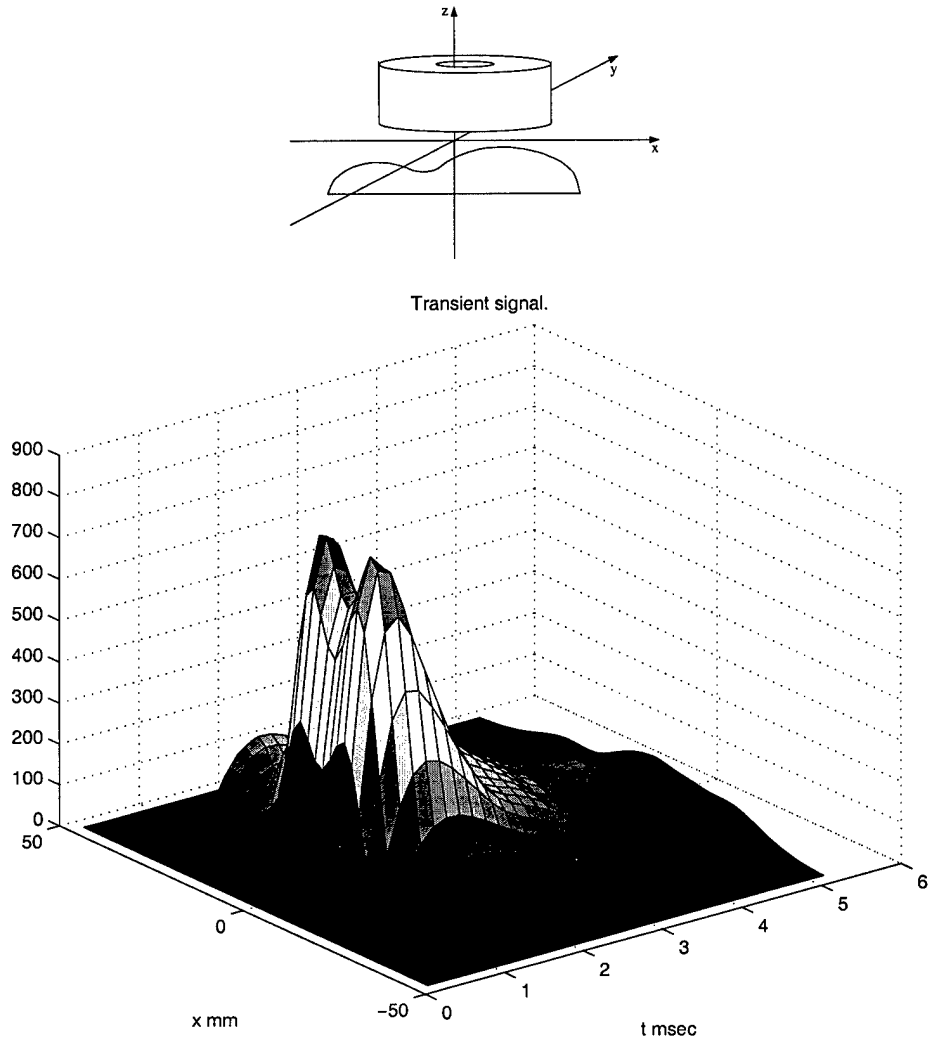

Figure 2.3: Calculations of the response of a field sensor on the axis of a coil in the presence of a sub-surface crack or notch. The vertical scale gives the magnetic field at the site of the Hall sensor (A/m). The double peak corresponds to the region where the notch is approximately 1 mm from the surface. To the left of the double peak is the indication from the deeper portion of the notch. This part of the indication is delayed in time.

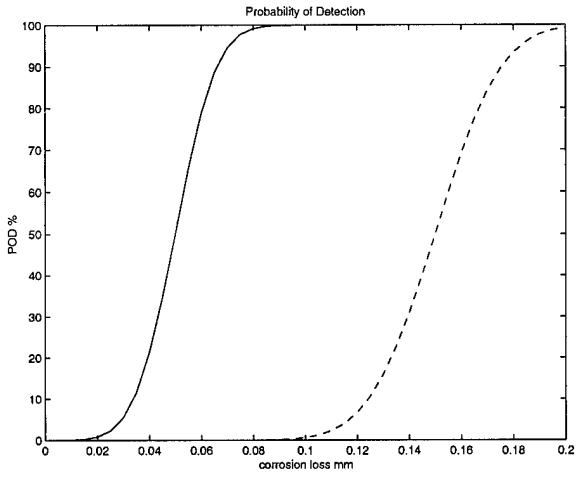

Figure 2.4: Probability of detection against first layer material loss for (a) 2 mm first layer, solid line (b) 4 mm first layer, dashed line.

Chapter 3

Numerical Evaluation of Pulsed Eddy-Current Interaction with Volumetric Flaws

In the problem considered, induce current pulses excited by an eddy-current probe interact with a three dimensional flaw in an otherwise uniform half-space conductor. The perturbation of the electromagnetic field due to the flaw is detected by measuring the time variation of the external magnetic field or the induced emf in a sensor coil. The aim is to compute the field as a function of time and hence predict the sensor signals. A volume integral formulation of the problem has been developed in order to calculate the perturbed field due to a region of corrosion or a crack in an otherwise homogeneous conductor. An integral equation for the field in the flaw has been derived. It is then approximated by a matrix equation using the moment method. Closed form expressions have been obtained for calculating the matrix elements including the singular element. From the solution of the matrix equation, the external magnetic field can be evaluated using a formula derived using reciprocity principles.

3.1 Introduction

The evolution of the electromagnetic field in a conductor containing an inhomogeneity has been calculated using volume elements by San Filipo and Hohmann[12] and by Wang and Hohmann[13] using the finite difference technique. These calculations are aimed at applications in geophysics but similar problems exist in pulsed eddy-current nondestructive evaluation(NDE). In NDE, the inhomogeneity is usually considered as localised which favours the volume element technique because its primary goal is calculate the field in the flaw region only. If this region is small and well defined then a good approximation may be obtained using a relatively small number of volume elements.

This article describes a time-domain volume element formulation for obtaining solutions that are approximated as piecewise linear in time and space. Results of transient field calculations are not included at this stage. However, the key features of the approach are set out, including the calculation of the self-element taking into account the singularity

of the Green's function. In addition, the remaining matrix elements corresponding, to a free-space dyadic Green kernel have been expressed in closed form. From the information given, it should be a relatively straightforward matter to adapted the matrix calculation to other geometries such as a conducting half-space.

3.2 Formulation

Assuming that the material properties are linear, that the permeability is that of free space and that displacement current is negligible, the electromagnetic field in a conductor containing a local conductivity variation satisfies

$$\nabla \times \mathbf{E}(\mathbf{r}) = -\mu_0 \frac{\partial \mathbf{H}(\mathbf{r})}{\partial t} \tag{3.1}$$

and

$$\nabla \times \mathbf{H}(\mathbf{r}) = \sigma_0 \mathbf{E}(\mathbf{r}) + \mathbf{P}(\mathbf{r}) \tag{3.2}$$

where σ_0 is the host conductivity and $\mathbf{P}(\mathbf{r}) = [\sigma(\mathbf{r}) - \sigma_0]\mathbf{E}(\mathbf{r})$ is a current dipole distribution representing the effect of the flaw as an equivalent source.

A solution of Maxwell's equations will be sought using the magnetic vector potential by following standard electromagnetic theory. The vector potential is defined such that $\mathbf{B} = \nabla \times \mathbf{A}$, hence, for a medium with the permeability of free space

$$\mathbf{H} = \frac{1}{\mu_0} \nabla \times \mathbf{A}. \tag{3.3}$$

By substituting for $\mu_0 \mathbf{H}(\mathbf{r})$ in the induction law, one concludes that the electric field has the form

$$\mathbf{E} = -\frac{\partial \mathbf{A}}{\partial t} - \nabla \psi, \tag{3.4}$$

where $\nabla\psi$ is a scalar potential. Substituting (3.3) and (3.4) into (3.2) and choosing the gauge where $\psi = -\nabla \cdot \mathbf{A}/\mu_0$ it is found that the vector potential satisfies a three dimensional vector diffusion equation

$$\nabla^2 \mathbf{A} + \mu_0 \sigma_0 \frac{\partial \mathbf{A}}{\partial t} = -\mu_0 \mathbf{P}(\mathbf{r}). \tag{3.5}$$

Combining the gauge condition with (3.4), shows that the electric field is given by

$$\mathbf{E} = -\left(\mathcal{I} \frac{\partial}{\partial t} - \frac{1}{\mu_0 \sigma_0} \nabla \nabla \right) \cdot \mathbf{A}, \tag{3.6}$$

where $\mathcal{I} = \hat{x}\hat{x} + \hat{y}\hat{y} + \hat{z}\hat{z}$ is the unit dyad. The solution of (3.5) will be written in the form

$$\mathbf{A}(\mathbf{r}) = \mathbf{A}^{(0)}(\mathbf{r}) - \mu_0 \int_0^t \int_\Omega \mathcal{G}_A(\mathbf{r}, \mathbf{r}', t - t') \cdot \mathbf{P}(\mathbf{r}', t') \, d\mathbf{r}' \, dt'. \tag{3.7}$$

where $\mathbf{A}^{(0)}(\mathbf{r})$ is the unperturbed field and the dyadic Green's function $\mathcal{G}_A(\mathbf{r}, \mathbf{r}', t - t')$ satisfies

$$\nabla^2 \mathcal{G}_A(\mathbf{r}, \mathbf{r}', t - t') + \mu_0 \sigma_0 \frac{\partial \mathcal{G}_A(\mathbf{r}, \mathbf{r}', t - t')}{\partial t} = -\mathcal{I} \delta(\mathbf{r} - \mathbf{r}') \delta(t - t'). \tag{3.8}$$

A solution of (3.8) for a half space conductor are given in reference [9].

3.3 Electric field integral equation

From (3.6) and (3.7), the electric field in the presence of a volumetric flaw is written as

$$\mathbf{E}(\mathbf{r},t) = \mathbf{E}^{(0)}(\mathbf{r},t) - \Big(\mu_0\frac{\partial}{\partial t}\mathcal{I} - \frac{1}{\sigma_0}\nabla\nabla\Big)\cdot\int_0^t\int_\Omega \mathcal{G}_A(\mathbf{r},\mathbf{r}',t,t')\cdot\mathbf{P}(\mathbf{r}',t')\,d\mathbf{r}'\,dt', \qquad (3.9)$$

where $\mathbf{P}(\mathbf{r}',t')$ is the induced dipole density at the defect and Ω is the flaw region. Multiplying by $\sigma(\mathbf{r}) - \sigma_0 = \sigma_0 v(\mathbf{r})$ gives

$$\mathbf{P}(\mathbf{r},t) = \mathbf{P}^{(0)}(\mathbf{r},t) - \sigma_0 v(\mathbf{r})\Big(\mu_0\frac{\partial}{\partial t}\mathcal{I} - \frac{1}{\sigma_0}\nabla\nabla\Big)\cdot\int_0^t\int_\Omega \mathcal{G}_A(\mathbf{r},\mathbf{r}',t,t')\cdot\mathbf{P}(\mathbf{r}',t')\,d\mathbf{r}'\,dt', \qquad (3.10)$$

which is a Fredholm integral equation of the second kind for the flaw polarisation. In Equation (3.10), $\mathbf{P}(\mathbf{r},t) = \sigma_0 v(\mathbf{r})\mathbf{E}(\mathbf{r},t)$ and $\mathbf{P}^{(0)}(\mathbf{r},t) = \sigma_0 v(\mathbf{r})\mathbf{E}^{(0)}(\mathbf{r},t)$.

3.4 Integral kernel

In the case of an unbounded domain, the integral kernel is given by[9]

$$\mathcal{G}_A(\mathbf{r},\mathbf{r}',t,t') = \mathcal{I}\phi(|\mathbf{r}-\mathbf{r}'|,t-t'), \qquad (3.11)$$

where $\phi(|\mathbf{r}-\mathbf{r}'|,t-t')$ satisfies the scalar diffusion equation with a singular source term, the solution being

$$\phi(R,t-t') = \frac{1}{8}\sqrt{\frac{\mu_0\sigma_0}{\pi^3(t-t')^3}}e^{-\mu_0\sigma_0 R^2/4(t-t')}H(t-t'). \qquad (3.12)$$

where $H(t-t')$ is the Heavyside step function, unity for positive argument and zero otherwise. This scalar Green's function can also be written as

$$\phi(|\mathbf{r}-\mathbf{r}'|,t-t') = \frac{1}{\mu_0\sigma_0\alpha^3}U\Big(\frac{x-x'}{\alpha}\Big)U\Big(\frac{y-y'}{\alpha}\Big)U\Big(\frac{z-z'}{\alpha}\Big)H(t-t'), \qquad (3.13)$$

where

$$\alpha(t-t') = 2\sqrt{(t-t')/\mu_0\sigma_0} \qquad (3.14)$$

is a diffusion length and

$$U(s) = \frac{1}{\sqrt{\pi}}e^{-s^2}. \qquad (3.15)$$

Note that the function $U(s)$ is normalised in the sense that

$$\int_{-\infty}^{\infty} U(s)\,ds = 1. \qquad (3.16)$$

An alternative to equation (3.12) is to write

$$\mu_0\sigma_0\phi(|\mathbf{r}-\mathbf{r}'|,t-t') = \frac{1}{\pi\alpha^3}U\Big(\frac{R}{\alpha}\Big)H(t-t'). \qquad (3.17)$$

The integral of the scalar Green's kernel is of interest, hence we define

$$\Phi(|\mathbf{r}-\mathbf{r}'|,t-t') = \int \phi(|\mathbf{r}-\mathbf{r}'|,t-t')d(t-t') = \frac{\mathrm{erfc}(R/\alpha)}{4\pi R}H(t-t'). \tag{3.18}$$

Note that as $t-t' \to \infty$, the complimentary error function approach unity and the right hand side of (3.18) tends to the familiar static Green's function.

In order to make prediction that can be compared with experiment, it would be necessary to used a half- space[9] or plate kernel in (3.10). The addition complications associated with this will not be considered here. Instead, the procedure of discretisation, as prescribed by the moment method, is defined for a flaw in an unbounded domain.

3.5 Regularisation

The differential operators might be dealt with in a numerical scheme using difference formulae but a better approach is to bring the derivatives inside the integrals with respect to time and space allowing them to act directly on the kernel. This leads to a modified kernel that can be approximated by adopting a numerical integration scheme. Note however, that the action of the time derivative on the time integral leads to a form

$$\frac{\partial}{\partial t}\int_{t_0}^{t} F(t,t')\,dt' = \int_{t_0}^{t} \frac{\partial F(t,t')}{\partial t}\,dt' + F(t,t) \tag{3.19}$$

evaluation of which requires the evaluation of $F(t,t')$ at $t'=t$. If it happens that $F(t,t')$ cannot be evaluated at $t'=t$, them some other way must be found to bring the time derivative inside the integral.

In the case of the integral equation (3.10), for the dipole distribution $\mathbf{P}(\mathbf{r},t)$ one identifies $F(t,t')$ with the components of

$$\mathbf{F}(\mathbf{r},t,t') = \int_{\Omega} \mathcal{G}_A(\mathbf{r},\mathbf{r}',t,t')\cdot\mathbf{P}(\mathbf{r}',t')\,d\mathbf{r}' \tag{3.20}$$

Assuming the dipole density is smooth, the integral can be approximated for small $t-t'$ by

$$\mathbf{F}(\mathbf{r},t,t') = \int_{\Omega_0} \mathcal{G}_A(\mathbf{r},\mathbf{r}',t,t')\cdot\,d\mathbf{r}'\mathbf{P}(\mathbf{r},t') \tag{3.21}$$

where Ω_0 is a sphere of radius R_0 about $\mathbf{r}$. Integration gives

$$\mathbf{F}(\mathbf{r},t,t') = \frac{1}{\mu_0\sigma_0}\mathbf{P}(\mathbf{r},t) \tag{3.22}$$

Provided $\mathbf{P}(\mathbf{r},t)$ is smooth, the function $\mathbf{F}(\mathbf{r},t,t')$ is non-singular, hence we can bring the time derivative inside the time integral. Bringing it inside the spatial integral is another matter and does in fact result in a kernel that has a singularity in time at $t-t'=0$. In finding a discrete form of the equation that determines the approximate dipole density of the source, this singularity is dealt with by subtraction. Thus we write

$$\mathbf{P}(\mathbf{r},t) \;-\; \sigma_0 \upsilon(\mathbf{r}) \int_\Omega \mathcal{K}(\mathbf{r},\mathbf{r}',t)\cdot\mathbf{P}(\mathbf{r}',t)\,d\mathbf{r}' =$$

$$\mathbf{P}^{(0)}(\mathbf{r},t) \;+\; \sigma_0 \upsilon(\mathbf{r}) \int_0^t \int_\Omega \mathcal{G}(\mathbf{r},\mathbf{r}',t,t')\cdot[\mathbf{P}(\mathbf{r}',t') - \mathbf{P}(\mathbf{r}',t)]\,d\mathbf{r}'\,dt' \qquad (3.23)$$

where

$$\mathcal{K}(\mathbf{r},\mathbf{r}',t) = -\mu_0 \mathcal{G}_A(\mathbf{r},\mathbf{r}',t) + \nabla\nabla\cdot\int \mathcal{G}_A(|\mathbf{r}-\mathbf{r}'|,t-t')\,d(t-t'), \qquad (3.24)$$

$$\mathcal{G}(\mathbf{r},\mathbf{r}',t-t') = -\Big(\mu_0 \frac{\partial}{\partial t}\mathcal{I} - \frac{1}{\sigma_0}\nabla\nabla\Big)\mathcal{G}_A(\mathbf{r},\mathbf{r}',t-t') \qquad (3.25)$$

For an unbounded domain, Equation (3.11) holds which means

$$\mathcal{K}(\mathbf{r},\mathbf{r}',t) = \mathcal{K}_0(\mathbf{r},\mathbf{r}',t) = -\mu_0\phi(|\mathbf{r}-\mathbf{r}'|,t)\mathcal{I} + \frac{1}{\sigma_0}\nabla\nabla\Phi(|\mathbf{r}-\mathbf{r}'|,t). \qquad (3.26)$$

and

$$\mathcal{G}(\mathbf{r},\mathbf{r}',t-t') = \mathcal{G}_0(\mathbf{r},\mathbf{r}',t-t') = -\Big(\mu_0 \frac{\partial}{\partial t}\mathcal{I} - \frac{1}{\sigma_0}\nabla\nabla\Big)\mathcal{I}\phi(\mathbf{r},\mathbf{r}',t-t') \qquad (3.27)$$

These functions are now expanded and the integral operators of equation (3.23) approximated by a discrete form using the moment method.

3.6 Expansion of the unbounded domain kernel

In expanding equation (3.27) it is necessary to consider the time and spatial derivative. Firstly we have

$$\mu_0\sigma_0 \frac{\partial\phi(R,t)}{\partial t} = \frac{2}{\alpha^2}\Big[2\Big(\frac{R}{\alpha}\Big)^2 - 3\Big]\phi(R,t) \qquad (3.28)$$

Note that this involves a t^{-1} singularity. Secondly

$$\frac{\partial^2\phi(R,t)}{\partial p^2} = \frac{2}{\alpha^2}\Big[2\Big(\frac{p}{\alpha}\Big)^2 - 1\Big]\phi(R,t) \qquad (3.29)$$

$$\frac{\partial^2\phi(R,t)}{\partial p\partial q} = \frac{4pq}{\alpha^4}\phi(R,t) \qquad (3.30)$$

Hence

$$\sigma_0\hat{x}\cdot\mathcal{G}(\mathbf{r},\mathbf{r}',t-t')\cdot\hat{x} = \sigma_0 G_0^{xx}(\mathbf{r},\mathbf{r}',t,t') = \frac{4}{\alpha^2}\Big[1 - \frac{(y-y')^2+(z-z')^2}{\alpha^2}\Big]\phi(|\,\mathbf{r}-\mathbf{r}'\,|,t-t') \qquad (3.31)$$

and

$$\sigma_0\hat{x}\cdot\mathcal{G}(\mathbf{r},\mathbf{r}',t-t')\cdot\hat{y} = \sigma_0 G_0^{xy}(\mathbf{r},\mathbf{r}',t,t') = \frac{4(x-x')(y-y')}{\alpha^4}\phi(|\,\mathbf{r}-\mathbf{r}'\,|,t-t') \qquad (3.32)$$

where $\hat{x}$ and $\hat{y}$ are unit vectors. Similar terms are obtain for yy zz yx yz and zy components by a cyclic rotation of the variables. The functions defined by Equation (3.31) and (3.32) lead to a t^{-1} singularity in the time integral. Hence the need to use some method such as the subtraction scheme, to regularise the time integral.

3.7 Primary Matrix Evaluation

The discrete form of the equation for the dipole density is found by assuming that the solution may be approximated as piecewise linear in space and time. Matrix elements are then defined by point matching. This process is carried out in two stages. Firstly the solution is approximated as piecewise linear in space by expanding in terms of linear expansion functions. Point matching then produces a set of time dependent primary matrix elements. Secondly the time variation is approximated as piecewise linear.

Linear expansion in space and point matching gives a set a matrix elements defined by

$$G^{(pq)}_{\alpha\beta}(t) = \int_{\Omega_\beta} G^{(pq)}(\mathbf{r}_\alpha, \mathbf{r}', t)\psi_\beta(\mathbf{r}')\, d\mathbf{r}' \tag{3.33}$$

where $x, y = p, q$. The function $\psi_\beta(\mathbf{r}')$ which is a convolution of the expansion and testing functions is given by

$$\psi_\beta(\mathbf{r}) = \psi_{jkl}(\mathbf{r}) = \psi_j(\frac{x}{\delta_x})\psi_k(\frac{y}{\delta_y})\psi_l(\frac{z}{\delta_z}) \tag{3.34}$$

where

$$\psi_j(s) = 1 - |s - j| \tag{3.35}$$

for $j - 1 < s \leq j + 1$ and zero otherwise.

For an unbounded domain,

$$\mathcal{G}_{\alpha\beta}(t) = \mathcal{G}^{(0)}_{\alpha-\beta}(t) = \int_{\Omega_\beta} \mathcal{G}_0(\mathbf{r}_\alpha, \mathbf{r}', t)\psi_\beta(\mathbf{r}')\, d\mathbf{r}' = \int_{\Omega_{\alpha-\beta}} \mathcal{G}_0(\mathbf{0}, \mathbf{r}', t)\psi_{\beta-\alpha}(\mathbf{r}')\, d\mathbf{r}', \tag{3.36}$$

where $\mathcal{G}_0(\mathbf{r}, \mathbf{r}', t)$ is given by (3.27). The components of the tensor, written as

$$G^{pq}_{jkl}(t) = \hat{p} \cdot \mathcal{G}^{(0)}_{jkl}(t) \cdot \hat{q}. \tag{3.37}$$

For the self element, equations (3.31) and (3.36) combine to give

$$\begin{aligned}
G^{xx}_{000}(t - t') &= 8\int_0^{\delta_x}\int_0^{\delta_y}\int_0^{\delta_z} \frac{4}{\alpha^2}\Big(1 - \frac{y^2 + z^2}{\alpha^2}\Big)\phi(0, \mathbf{r}, t - t')\psi_{000}(\mathbf{r})\, dx\, dy\, dz \\
&= \frac{8}{(t - t')}\int_0^{\delta_x}\int_0^{\delta_y}\int_0^{\delta_z} \frac{1}{\alpha^3}\Big(1 - \frac{y^2 + z^2}{\alpha^2}\Big) \\
&\qquad U(x/\alpha)U(y/\alpha)U(z/\alpha)\psi_{000}(\mathbf{r})\, dx\, dy\, dz \\
&= \frac{8}{(t - t')}\int_0^{\delta_x/\alpha}\int_0^{\delta_y/\alpha}\int_0^{\delta_z/\alpha} (1 - y^2 - z^2) \\
&\qquad U(x)U(y)U(z)\psi_{000}(\alpha\mathbf{r})\, dx\, dy\, dz \\
&= \frac{2}{(t - t')}\int_0^{\delta_x/\alpha}\Big(1 - \frac{\alpha x}{\delta_x}\Big)U(x)\, dx \times \\
&\qquad \int_0^{\delta_y/\alpha}\int_0^{\delta_z/\alpha}(1 - y^2 - z^2)\Big(1 - \frac{\alpha y}{\delta_y}\Big)\Big(1 - \frac{\alpha z}{\delta_z}\Big)U(y)U(z)\, dy\, dz \\
&= \frac{\alpha^3}{\delta_x\delta_y\delta_z(t - t')}F^{(0)}\Big(\frac{\delta_x}{\alpha}\Big)\Big[F^{(2)}\Big(\frac{\delta_y}{\alpha}\Big)F^{(0)}\Big(\frac{\delta_z}{\alpha}\Big) + \\
&\qquad F^{(0)}\Big(\frac{\delta_y}{\alpha}\Big)F^{(2)}\Big(\frac{\delta_z}{\alpha}\Big) - F^{(0)}\Big(\frac{\delta_y}{\alpha}\Big)F^{(0)}\Big(\frac{\delta_z}{\alpha}\Big)\Big]
\end{aligned} \tag{3.38}$$

where

$$F^{(n)}(s) = \frac{2}{\sqrt{\pi}} \int_0^s x^n (x-s) e^{-x^2} dx \tag{3.39}$$

For the cases where $n = 0, 1, 2$, it is found that

$$F^{(0)}(s) = \frac{1}{\sqrt{\pi}} - s \, \mathrm{erf}(s) - U(s), \tag{3.40}$$

$$F^{(1)}(s) = -\frac{s}{\sqrt{\pi}} + \frac{1}{2}\mathrm{erf}(s) \tag{3.41}$$

and

$$F^{(2)}(s) = \frac{1}{\sqrt{\pi}} - \frac{1}{2} s \, \mathrm{erf}(s) - U(s). \tag{3.42}$$

For a general matrix element, equations (3.31) and (3.36) give

$$\begin{aligned} G^{xx}_{jkl}(t-t') &= \int_{(j-1)\delta_x}^{(j+1)\delta_x} \int_{(k-1)\delta_y}^{(k+1)\delta_y} \int_{(l-1)\delta_z}^{(l+1)\delta_z} \frac{4}{\alpha^2}\Big(1 - \frac{y^2+z^2}{\alpha^2}\Big) \\ &\quad \phi(0, \mathbf{r}, t-t') \psi_{jkl}(\mathbf{r}) \, dx \, dy \, dz \\ &= \frac{1}{(t-t')} \int_{(j-1)\delta_x/\alpha}^{(j+1)\delta_x/\alpha} \int_{(k-1)\delta_y/\alpha}^{(k+1)\delta_y/\alpha} \int_{(l-1)\delta_z/\alpha}^{(l+1)\delta_z/\alpha} (1 - y^2 - z^2) \\ &\quad U(x)U(y)U(z)\psi_{jkl}(\alpha \mathbf{r}) \, dx \, dy \, dz. \end{aligned} \tag{3.43}$$

This can be expressed in terms of standard functions as defined above by separating the integrals as follows.

$$\begin{aligned} G^{xx}_{jkl}(t-t') &= \frac{1}{(t-t')} \int_{(j-1)\delta_x/\alpha}^{(j+1)\delta_x/\alpha} \Big(1 - |\frac{\alpha x}{\delta_x} - j|\Big) U(x) \, dx \\ &\quad \int_{(k-1)\delta_y/\alpha}^{(k+1)\delta_y/\alpha} \int_{(l-1)\delta_z/\alpha}^{(l+1)\delta_z/\alpha} (1 - y^2 - z^2) \\ &\quad \Big(1 - |\frac{\alpha y}{\delta_y} - k|\Big)\Big(1 - |\frac{\alpha z}{\delta_z} - l|\Big) U(y)U(z) \, dy \, dz \\ &= \frac{\alpha^3}{8\delta_x\delta_y\delta_z(t-t')} F^{(0)}_j(\frac{\delta_x}{\alpha}) \Big[F^{(2)}_k(\frac{\delta_y}{\alpha}) F^{(0)}_l(\frac{\delta_z}{\alpha}) + \\ &\quad F^{(0)}_k(\frac{\delta_y}{\alpha}) F^{(2)}_l(\frac{\delta_z}{\alpha}) - F^{(0)}_k(\frac{\delta_y}{\alpha}) F^{(0)}_l(\frac{\delta_z}{\alpha}) \Big] \end{aligned} \tag{3.44}$$

where

$$\begin{aligned} F^{(n)}_j(s) &= \frac{2}{\sqrt{\pi}} \int_{(j-1)s}^{(j+1)s} x^n (|x - js| - s) e^{-x^2} dx \\ &= F^{(n)}(s_{j+1}) - 2F^{(n)}(s_j) + F^{(n)}(s_{j-1}) \end{aligned} \tag{3.45}$$

with $s_j = js$. Note that $F^{(n)}_0(s) = 2F^{(n)}(s)$.

From (3.32) it can be seen that the terms off the tensor diagonal are of the type

$$\begin{aligned} G^{xy}_{000}(t-t') &= 8\int_0^{\delta_x}\int_0^{\delta_y}\int_0^{\delta_z}\frac{4xy}{\alpha^4}\phi(0,\mathbf{r},t-t')\psi_{000}(\mathbf{r})\,dx\,dy\,dz \\ &= \frac{8}{(t-t')}\int_0^{\delta_x/\alpha}\int_0^{\delta_y/\alpha}\int_0^{\delta_z/\alpha} xyU(x)U(y)U(z)\psi_{000}(\alpha\mathbf{r})\,dx\,dy\,dz \\ &= -\frac{\alpha^3}{\delta_x\delta_y\delta_z(t-t')}F^{(1)}(\frac{\delta_x}{\alpha})F^{(1)}(\frac{\delta_y}{\alpha})F^{(0)}(\frac{\delta_z}{\alpha}) \end{aligned} \tag{3.46}$$

For a general off-diagonal element

$$\begin{aligned} G^{xy}_{jkl}(t-t') &= \int_{(j-1)\delta_x}^{(j+1)\delta_x}\int_{(k-1)\delta_y}^{(k+1)\delta_y}\int_{(l-1)\delta_z}^{(l+1)\delta_z}\frac{4xy}{\alpha^4}\phi(0,\mathbf{r},t-t')\psi_{jkl}(\mathbf{r})\,dx\,dy\,dz \\ &= \frac{1}{(t-t')}\int_{(j-1)\delta_x/\alpha}^{(j+1)\delta_x/\alpha}\int_{(k-1)\delta_y/\alpha}^{(k+1)\delta_y/\alpha}\int_{(l-1)\delta_z/\alpha}^{(l+1)\delta_z/\alpha} xyU(x)U(y)U(z)\psi_{jkl}(\mathbf{r})\,dx\,dy\,dz \\ &= -\frac{\alpha^3}{8\delta_x\delta_y\delta_z(t-t')}F^{(1)}_j(\frac{\delta_x}{\alpha})F^{(1)}_k(\frac{\delta_y}{\alpha})F^{(0)}_l(\frac{\delta_z}{\alpha}) \end{aligned} \tag{3.47}$$

3.8 Integrated Kernel Matrix

Define the integrated kernel matrix as

$$\mathcal{K}_{\alpha\beta}(t) = \sigma_0\int_{\Omega_\beta}\mathcal{K}(\mathbf{r}_\alpha,\mathbf{r}',t)\psi_\beta(\mathbf{r}')\,d\mathbf{r}' \tag{3.48}$$

and the moment matrix as

$$\mathcal{M}_{\alpha\beta}(t) = \sigma_0\int_{\Omega_\beta}\mathcal{M}(\mathbf{r}_\alpha,\mathbf{r}',t)\psi_\beta(\mathbf{r}')\,d\mathbf{r}' \tag{3.49}$$

where, by definition,

$$\mathcal{K}(\mathbf{r}_\alpha,\mathbf{r}',t) = \int\mathcal{G}(\mathbf{r},\mathbf{r}',t)\,dt \tag{3.50}$$

and

$$\mathcal{M}(\mathbf{r},\mathbf{r}',t) = \int\mathcal{G}(\mathbf{r},\mathbf{r}',t)t\,dt \tag{3.51}$$

Thus

$$K^{(pq)}_{klm}(t) = \int_{\Omega_{klm}}\beta_{klm}(\mathbf{r})[-\mu_0\sigma_0\delta_{pq}\phi(\mathbf{r},t)+\partial_p\partial_q\Phi(\mathbf{r},t)]\,d\mathbf{r} \tag{3.52}$$

and

$$M^{(pq)}_{klm}(t) = tK^{(pq)}_{klm}(t) - \int K^{(pq)}_{klm}(t)\,dt \tag{3.53}$$

In order to evaluate (3.52) and (3.53), note that

$$4\pi\frac{\partial^2\Phi(R,t)}{\partial^2 x} = 4\frac{(x-x')^2}{\alpha^3R^2}U\Big(\frac{R}{\alpha}\Big) - \frac{1}{R^3}\Big[2\frac{R}{\alpha}U\Big(\frac{R}{\alpha}\Big)+\operatorname{erfc}\Big(\frac{R}{\alpha}\Big)\Big]\Big[1-\frac{3(x-x')^2}{R^2}\Big] \tag{3.54}$$

and

$$4\pi\frac{\partial^2\Phi(R,t)}{\partial x\partial y} = \Big\{\frac{2}{\alpha}\Big[2\Big(\frac{R}{\alpha}\Big)^2-3\Big]U\Big(\frac{R}{\alpha}\Big) - 3\operatorname{erfc}\Big(\frac{R}{\alpha}\Big)\Big\}\frac{(x-x')(y-y')}{R^3} \tag{3.55}$$

For the singular elements, we introduce a cubic exclusion volume Ω_0, each side having a length $2a$ that is less than or equal to the smallest of the cell dimensions, δ_x δ_y and δ_z. The exclusion volume is centered on the singularity at $\mathbf{r} = 0$. Define the regularized singular integral corresponding to the tensor components of Eq. (3.48) as[14]

$$\begin{aligned} K_{klm}^{(pq)}(t) &= \int_{\Omega_{klm}} \beta_{klm}(\mathbf{r})[-\mu_0\sigma_0\delta_{pq}\phi(\mathbf{r},t) + \partial_p\partial_q\Phi(\mathbf{r},t)]\ d\mathbf{r} \\ &= A_{klm}^{(pq)}(t) + B_{klm}^{(pq)}(t) + C_{klm}^{(pq)}(t) + D_{klm}^{(pq)}(t), \end{aligned} \tag{3.56}$$

where, suppressing the time dependence

$$A_{klm}^{(pq)} = \int_{\Omega_{klm}-\Omega_0} \beta_{klm}(\mathbf{r})\partial_p\partial_q\Phi(\mathbf{r})\ d\mathbf{r} \tag{3.57}$$

$$B_{klm}^{(pq)} = \int_{\Omega_0} [\beta_{klm}(\mathbf{r}) - \beta_{klm}(\mathbf{0})]\partial_p\partial_q\Phi(\mathbf{r})d\mathbf{r} + \beta_{klm}(\mathbf{0}) \int_{\Omega_0} \partial_p\partial_q[\Phi(\mathbf{r}) - \Phi_0(\mathbf{r})]d\mathbf{r} \tag{3.58}$$

$$C_{klm}^{(pq)} = \beta_{klm}(\mathbf{0})\Big[\partial_p\partial_q \int_{\Omega_0} \Phi_0(\mathbf{r}-\mathbf{r}')\ d\mathbf{r}'\Big]_{\mathbf{r}=\mathbf{0}} \tag{3.59}$$

$$D_{klm}^{(pq)} = -\mu_0\sigma_0\delta_{pq} \int_{\Omega_{klm}} \phi(\mathbf{r})\beta_{klm}(\mathbf{r})\ d\mathbf{r} \tag{3.60}$$

Here $\Phi_0(\mathbf{r})$ is the static potential and $\Phi(\mathbf{r})$ the dynamic potential defined as

$$\Phi_0(\mathbf{r}) = \frac{1}{4\pi|\mathbf{r}|} \qquad \Phi(\mathbf{r}) = \frac{\mathrm{erfc}(|\mathbf{r}|/\alpha)}{4\pi|\mathbf{r}|}. \tag{3.61}$$

The contributions to Eq. (3.56) are examined below, term by term and case by case.

3.8.1 Evaluation of $A_{klm}^{(pq)}$

The calculation of $A_{klm}^{(pq)}$ is done using any suitable numerical quadrature scheme which approximates the integral over the region, $\Omega_{klm} - \Omega_0$, by a summation[15]. Thus,

$$A_{klm}^{(pq)} = \int_{\Omega_{klm}-\Omega_0} \beta_{klm}(\mathbf{r})\partial_p\partial_q\Phi(\mathbf{r})\ d\mathbf{r} \tag{3.62}$$

$$\approx \sum_{\mathbf{r}_\nu} c_\nu\beta_{klm}(\mathbf{r}_\nu)[\partial_p\partial_q\Phi(\mathbf{r})]_{\mathbf{r}_\nu}, \tag{3.63}$$

where c_ν and $\mathbf{r}_\nu$ are the appropriate quadrature weights and points of evaluation respectively.

3.8.2 Evaluation of $C_{klm}^{(pq)}$

With reference to Eq. (3.59), the only case where $\beta_{klm}(\mathbf{0})$ is nonzero is that where $k, l, m = 0$. Evaluating the relevant integral and noting that $\beta_{000}(\mathbf{0}) = 1.0$, it is found that

$$C_{000}^{(pq)} = \beta_{000}(\mathbf{0})\Big[\partial_p\partial_q \int_{\Omega_0} \Phi_0(\mathbf{r}-\mathbf{r})\ d\mathbf{r}\Big]_{\mathbf{r}=\mathbf{0}} = -\frac{1}{3}\delta_{pq}, \tag{3.64}$$

where $\delta_{pq} = 1$ if $p = q$ and $\delta_{pq} = 0$ otherwise.

3.8.3 Evaluation of $D_{klm}^{(pq)}$

For a general element

$$\begin{aligned} D_{klm}^{(pq)} &= -\mu_0\sigma_0\delta_{pq}\int_{\Omega_{klm}}\phi(\mathbf{r})\beta_{klm}(\mathbf{r})\,d\mathbf{r} \\ &= -\delta_{pq}\int_{(j-1)\delta_x}^{(j+1)\delta_x}\int_{(k-1)\delta_y}^{(k+1)\delta_y}\int_{(l-1)\delta_z}^{(l+1)\delta_z}\left(1-|\frac{\alpha x}{\delta_x}-j|\right)\left(1-|\frac{\alpha y}{\delta_y}-k|\right)\left(1-|\frac{\alpha z}{\delta_z}-l|\right) \\ &\quad U(x)U(y)U(z)\,dx\,dy\,dz \\ &= \delta_{pq}\frac{\alpha^3}{8\delta_x\delta_y\delta_z}F_j^{(0)}\left(\frac{\delta_x}{\alpha}\right)F_k^{(0)}\left(\frac{\delta_y}{\alpha}\right)F_l^{(0)}\left(\frac{\delta_z}{\alpha}\right) \end{aligned} \tag{3.65}$$

where $F_j^{(0)}(\xi)$ is given by (3.45).

3.8.4 Evaluation of $B_{klm}^{(pq)}$

We begin this section by considering $B_{000}^{(pp)}$. Results for this initial case are used in the evaluation of $B_{klm}^{(pq)}$ where k, l and m take on values that are combinations of zero and one. In all other cases there is no overlap with the exclusion zone.

Note that the first term in brackets in equation (3.58) is

$$[\beta_{000}(\mathbf{r}')-\beta_{000}(\mathbf{0})] = -|\frac{x'}{\delta_x}|-|\frac{y'}{\delta_y}|-|\frac{z'}{\delta_z}|+|\frac{x'y'}{\delta_x\delta_y}|+|\frac{x'z'}{\delta_x\delta_z}|+|\frac{y'z'}{\delta_y\delta_z}|-|\frac{x'y'z'}{\delta_x\delta_y\delta_z}|. \tag{3.66}$$

Substituting into the defining relationship for $B_{000}^{(pp)}$, Equation (3.58), we find that

$$B_{000}^{(pp)} = 8(-c_0^x q_0 - c_1^x q_1 + c_2^x q_2 + c_3^x q_3 - c_3 q_4 + q_5) \tag{3.67}$$

where

$$c_0^x = \frac{a}{\delta_x} \qquad c_1^x = \frac{a}{\delta_y}+\frac{a}{\delta_z} \qquad c_2^x = \frac{a^2}{\delta_x\delta_y}+\frac{a^2}{\delta_x\delta_z} \qquad c_3^x = \frac{a^2}{\delta_y\delta_z} \qquad c_3 = \frac{a^3}{\delta_x\delta_y\delta_z}. \tag{3.68}$$

and the q's are defined by integrals given below. Note that the integration in each case is over the region defined by $0 < x < \delta_x$, $0 < y < \delta_y$ and $0 < z < \delta_z$, the region being referred to as the first octant, Ω_1. Thus

$$q_0 = \frac{1}{a}\int_{\Omega_1} x\frac{\partial^2\Phi}{\partial x^2}\,d\mathbf{r} \qquad q_1 = \frac{1}{a}\int_{\Omega_1} y\frac{\partial^2\Phi}{\partial x^2}\,d\mathbf{r} \qquad q_2 = \frac{1}{a^2}\int_{\Omega_1} xy\frac{\partial^2\Phi}{\partial x^2}\,d\mathbf{r} \tag{3.69}$$

$$q_3 = \frac{1}{a^2}\int_{\Omega_1} yz\frac{\partial^2\Phi}{\partial x^2}\,d\mathbf{r} \qquad q_4 = \frac{1}{a^3}\int_{\Omega_1} xyz\frac{\partial^2\Phi}{\partial x^2}\,d\mathbf{r}' \qquad q_5 = \int_{\Omega_1}\frac{\partial^2\Phi-\Phi_0}{\partial x^2}\,d\mathbf{r} \tag{3.70}$$

These integrals are approximated by power series in $\lambda = a/\alpha$, by expanding the function $\mathrm{erfc}(R/\alpha)$ as a power series in R/α and integrating term by term. In general

$$q_s = \int_{\Omega_1} f_s(\mathbf{r})\frac{\partial^2}{\partial x^2}\left[\frac{g(R/\alpha)}{R}\right]d\mathbf{r} \tag{3.71}$$

In this form one can compare similar developments for the time- harmonic case, where $1/\alpha = ik$ and $g(ikR) = exp(ikR)$, with the transient case for which $g(R/\alpha) = \text{erfc}(R/\alpha)$. Formally integrating with respect to x gives

$$q_s = \int_0^1 \int_0^1 [F(1,y,z) - F(0,y,z)]dy\,dz \tag{3.72}$$

where

$$\begin{aligned} F(x,y,z) &= f_s(\mathbf{r})\frac{\partial}{\partial x}\left[\frac{g(R/\alpha)}{R}\right] - \frac{\partial f_s(\mathbf{r})}{\partial x}\frac{g(R/\alpha)}{R} \\ &= -\left[\frac{\partial f_s(\mathbf{r})}{\partial x} + \frac{x}{R^2}f_s(\mathbf{r})\right]\frac{g(R/\alpha)}{R} + f_s(\mathbf{r})\frac{x}{R^2}\frac{\partial g(R/\alpha)}{\partial R} \end{aligned} \tag{3.73}$$

The required series expansions are

$$g(x) = 1 - \text{erf}(x) = 1 - \sum_{n=0}^{\infty} a_n x^{2n+1} \qquad \text{and} \qquad x\frac{\partial g(x)}{\partial x} = -\sum_{n=0}^{\infty} a_n(2n+1)x^{2n+1} \tag{3.74}$$

where

$$a_n = \frac{2}{\sqrt{\pi}}\frac{(-1)^n}{n!(2n+1)} \tag{3.75}$$

Substituting into (3.73) gives

$$F(x,y,z) = -\frac{1}{R}\left[\frac{\partial f_s(\mathbf{r})}{\partial R} + \frac{x}{R^2}f_s(\mathbf{r})\right] + \frac{1}{R}\sum_{n=0}^{\infty}\left[\frac{\partial f_s(\mathbf{r})}{\partial x} - 2n\frac{x}{R^2}f_s(\mathbf{r})\right]a_n\left(\frac{R}{\alpha}\right)^{2n+1} \tag{3.76}$$

Numerical integration of (3.72) will now give the coefficient in the power series.

Alternatively the integration can be performed numerically in three dimensions in which case we need to evaluate

$$\frac{\partial^2}{\partial x^2}\left[\frac{g(R/\alpha)}{R}\right] = \frac{1}{R^3}[Rg' - g][1 - \frac{3x^2}{R^2}] + \frac{x^2}{R^3}g'' \tag{3.77}$$

Using the power series expansion for the error function gives

$$\frac{\partial^2}{\partial x^2}\left[\frac{g(R/\alpha)}{R}\right] = -\frac{1}{R^3}\left[1 - \frac{3x^2}{R^2}\right] - \frac{1}{R^3}\sum_{n=1}^{\infty} 2n\left[1 + 2(n-1)\frac{x^2}{R^2}\right]a_n\left(\frac{R}{\alpha}\right)^{2n+1} \tag{3.78}$$

Similarly

$$\frac{\partial^2}{\partial x \partial y}\left[\frac{g(R/\alpha)}{R}\right] = \frac{3xy}{R^5} - \frac{xy}{R^5}\sum_{n=1}^{\infty} 4n(n-1)a_n\left(\frac{R}{\alpha}\right)^{2n+1}. \tag{3.79}$$

In this way we get

$$q_0 \approx .035475 + 0.029931\lambda^2 - 0.038911\lambda^3 + 0.027508\lambda^4 - 0.014249\lambda^5 \tag{3.80}$$

$$q_1 \approx -0.0177375 + .029931\lambda^2 - .032924\lambda^3 + .022662\lambda^4 - 0.11850\lambda^5 \tag{3.81}$$

$$q_2 \approx 0.0038345 + .014966\lambda^2 - .020952\lambda^3 + .016141\lambda^4 - 0.009015\lambda^5 \tag{3.82}$$

$$q_3 \approx -.007669 + .014966\lambda^2 - .017959\lambda^3 + .013362\lambda^4 - 0.007483\lambda^5 \tag{3.83}$$

$$q_4 \approx .007483\lambda^2 - .011224\lambda^3 + .009353\lambda^4 - 0.005612\lambda^5 \tag{3.84}$$

$$q_5 \approx 0.059862\lambda^2 - 0.059862\lambda^3 + 0.037913\lambda^4 - 0.018465\lambda^5 \tag{3.85}$$

	$B_{000}^{(xx)}$	$B_{100}^{(xx)}$	$B_{010}^{(xx)}$	$B_{001}^{(xx)}$	$B_{110}^{(xx)}$	$B_{011}^{(xx)}$	$B_{101}^{(xx)}$	$B_{111}^{(xx)}$
$b_0^{(xx)}$	$-8c_0^x$	$4c_0^x$	0	0	0	0	0	0
$b_1^{(xx)}$	$-8c_1^x$	0	$4c_1^y$	$4c_1^z$	0	0	0	0
$b_2^{(xx)}$	$8c_2^x$	$-4c_2^x$	$-4c_3^z$	$-4c_3^y$	$2c_3^z$	0	$2c_3^y$	0
$b_3^{(xx)}$	$8c_3^x$	0	$-4c_3^x$	$-4c_3^x$	0	$2c_3^x$	0	0
$b_4^{(xx)}$	$-8c_3$	$4c_3$	$4c_3$	$4c_3$	$-2c_3$	$-2c_3$	$-2c_3$	c_3
$b_5^{(xx)}$	8	0	0	0	0	0	0	0

Table 3.1: Coefficients for the evaluation of $B_{klm}^{(xx)}$

As the second order partial with respect to x, y or z produces an even function and β_{000} is even, contributions from the remaining 7 octants are the same as those for the first octant. The above considerations allow us to determine $B_{000}^{(xx)}$. In a similar way, the other possibilities are expressed in the form

$$B_{klm}^{(xx)} \approx \sum_{s=0}^{5} b_s^{(xx)} q_s, \tag{3.86}$$

with the $b's$ given in Table 3.1. The corresponding results for yy and zz components are found by appropriate cyclic rotation of the coordinate indices.

Next consider the evaluation of Eq. (3.58), for cases involving a mixed derivative, for example derivatives with respect to x and y. It is necessary to evaluate both of the integrals in equation (3.58). In doing so one notes that the mixed derivatives are odd functions in x and y, therefore the first integral is zero for all cases except $B_{110}^{(xy)}$ and $B_{111}^{(xy)}$. The second integral is zero for all k, l and m, since $\beta_{klm}(\mathbf{0}) = 0$ unless $k = l = m = 0$ in which case the integral is zero by anti-symmetry. Hence we need only concern ourselves with the terms

$$t_0 = \frac{1}{a^2} \int_{\Omega_1} xy \frac{\partial^2 \Phi}{\partial x \partial y} \, d\mathbf{r} \qquad t_1 = \frac{1}{a^3} \int_{\Omega_1} xyz \frac{\partial^2 \Phi}{\partial x \partial y} \, d\mathbf{r} \tag{3.87}$$

Expanding the integrand as a power series in R/α and integrating term by term gives

$$\begin{aligned} t_0 &\approx .020833 - .007982\lambda^3 + .008741\lambda^4 - 0.005714\lambda^5 \ldots \\ t_1 &\approx .006367 - .003991\lambda^3 + .004846\lambda^4 - 0.003448\lambda^5 \ldots \end{aligned} \tag{3.88}$$

Thus we express

$$B_{klm}^{(xy)} \approx \sum_{s=0}^{1} b_s^{(xy)} t_s \tag{3.89}$$

with the coefficients are given in Table 3.2.

3.9 Conclusion

A volume integral formulation has been presented for calculating the interaction of pulsed eddy currents with a volumetric flaw in a conductor. The approach uses a hypersingular kernel, as

	$B_{000}^{(xy)}$	$B_{100}^{(xy)}$	$B_{010}^{(xy)}$	$B_{001}^{(xy)}$	$B_{110}^{(xy)}$	$B_{011}^{(xy)}$	$B_{101}^{(xy)}$	$B_{111}^{(xy)}$
$b_0^{(xy)}$	0	0	0	0	$2c_2^z$	0	0	0
$b_1^{(xy)}$	0	0	0	0	$-2c_3$	0	0	c_3

Table 3.2: Coefficients for the evaluation of $B_{klm}^{(xy)}$

in the corresponding time-harmonic problem[16]. This means that the methods used by Lee *et al* [14] for the crucial calculation of the self-element, can be adopted for treating the time domain problem[17]. Here complete analysis of the self-element evaluation has been given.

Appendix A
Half-space matrix

A1 Half-space kernel

In Sections 7 and 8, matrix elements are evaluated from the unbounded domain integral kernels. In this Appendix, the matrix elements for half-space kernels are evaluated. For a half-space, the primary Green's function is written as [9]

$$\mathcal{G}(\mathbf{r},\mathbf{r}',t,t') = \mathcal{G}_0(\mathbf{r},\mathbf{r}',t,t') + \mathcal{G}_i(\mathbf{r},\mathbf{r}',t,t') + \frac{1}{\sigma_0}\frac{\partial}{\partial t}\nabla\times\hat{z}[\nabla'\times\hat{z}V(\mathbf{r},\mathbf{r}',t,t')], \tag{A1}$$

where $\mathcal{G}_0(\mathbf{r},\mathbf{r}',t,t')$ is the free-space integrated kernel given by (3.25) with (3.11) and (3.12). The corresponding image term is given by

$$\mathcal{G}_i(\mathbf{r},\mathbf{r}',t,t') = -\left[\mu_0\frac{\partial}{\partial t}\mathcal{I}' + \frac{1}{\sigma_0}\nabla\nabla'\right]\phi(\mathbf{r},\mathbf{r}'',t,t'), \tag{A2}$$

where $\mathcal{I} = \hat{x}\hat{x} + \hat{y}\hat{y} - \hat{z}\hat{z}$, and $\mathbf{r}'' = \mathbf{r} - 2z'\hat{z}$, is the image point. In evaluating the Green's kernel we note that[9]

$$V(\mathbf{r},\mathbf{r}',t-t') = \frac{1}{(2\pi)^2 i}\int_0^\infty\left\{\int_{\mathrm{Br}}\frac{1}{s}\widetilde{V}(\kappa,s)e^{s(t-t')}\,ds\right\}J_0(\kappa\rho)\kappa d\kappa \tag{A3}$$

where

$$\widetilde{V}(\kappa,s) = \left(\frac{1}{\kappa}-\frac{1}{\gamma}\right)e^{-\gamma|z+z'|}, \tag{A4}$$

$\rho^2 = (x-x')^2 + (y-y')^2$ and $\gamma = \sqrt{\kappa^2 - \mu_0\sigma_0 s}$.

A2 Moment kernels

The integrated kernel is defined as

$$\mathcal{K}(\mathbf{r},\mathbf{r}',t,t') = \int\mathcal{G}(\mathbf{r},\mathbf{r}',t,t')\,d(t-t') \tag{A5}$$

and the (first order) moment kernel as

$$\mathcal{M}(\mathbf{r},\mathbf{r}',t,t') = \int(t-t')\mathcal{G}(\mathbf{r},\mathbf{r}',t,t')\,d(t-t'). \tag{A6}$$

Therefore the integrated kernel is given by

$$\mathcal{K}(\mathbf{r},\mathbf{r}',t,t') = \mathcal{K}_0(\mathbf{r},\mathbf{r}',t,t') + \mathcal{K}_i(\mathbf{r},\mathbf{r}',t,t') + \frac{1}{\sigma_0}\nabla\times\hat{z}[\nabla'\times\hat{z}V(\mathbf{r},\mathbf{r}',t,t')], \tag{A7}$$

where $\mathcal{K}_0(\mathbf{r},\mathbf{r}',t,t')$ is the free-space integrated kernel given by (3.24) with (3.11) and (3.12). The corresponding image term is given by

$$\mathcal{K}_i(\mathbf{r},\mathbf{r}',t,t') = -\left[\mu_0\phi(\mathbf{r},\mathbf{r}'',t,t')\mathcal{I}' + \frac{1}{\sigma_0}\nabla\nabla'\Phi(\mathbf{r},\mathbf{r}'',t,t')\right], \tag{A8}$$

The first moment kernel is given by

$$\mathcal{M}(\mathbf{r},\mathbf{r}',t,t') = \mathcal{M}_0(\mathbf{r},\mathbf{r}',t,t') + \mathcal{M}_i(\mathbf{r},\mathbf{r}',t,t') + \frac{1}{\sigma_0}\nabla\times\hat{z}[\nabla'\times\hat{z}W(\mathbf{r},\mathbf{r}',t,t')], \tag{A9}$$

where

$$\begin{aligned} W(\mathbf{r},\mathbf{r}',t,t') &= \int t\frac{\partial V(\mathbf{r},\mathbf{r}',t,t')}{\partial t}\,dt \\ &= \frac{1}{(2\pi)^2 i}\int_0^\infty\left\{\int_{\mathrm{Br}}\left[-\frac{1}{s}\frac{\partial\tilde{V}(\kappa,s)}{\partial s}\right]e^{s(t-t')}\,ds\right\}J_0(\kappa\rho)\kappa d\kappa \\ &= \frac{\mu_0\sigma_0}{(2\pi)^2 i}\int_0^\infty\int_{\mathrm{Br}}\frac{1}{2\gamma s}\left[\frac{1}{\gamma^2}-|z+z'|\left(\frac{1}{\kappa}-\frac{1}{\gamma}\right)\right]e^{s(t-t')-\gamma|z+z'|}\,ds\,J_0(\kappa\rho)\kappa d\kappa \end{aligned} \tag{A10}$$

A3 Integrated Kernel Matrix evaluation

The matrix for the integrated kernel is written as

$$\mathcal{K}_{klm,KLM}(t) = \mathcal{K}^{(0)}_{k-K,l-L,m-M}(t) + \mathcal{K}^{(i)}_{k-K,l-L,m+M+1}(t) + \mathcal{K}^{(V)}_{k-K,l-L,m+M+1}(t), \tag{A11}$$

where $k,K = 0,\,1,\,2\ldots N_x$, $l,L = 0,\,1,\,2\ldots N_y$, $m,M = 0,\;1,\;2,\ldots N_z$. $\mathcal{K}^{(0)}_{k-K,l-L,m-M}(t)$ is given by (3.52) and

$$\begin{aligned} \mathcal{K}^{(V)}_{klm}(t) &= -\frac{1}{\sigma_0}\int_{\Omega_{klm}}\beta_{klm}(\mathbf{r}')\nabla'\times\hat{z}[\nabla'\times\hat{z}V(\mathbf{0},\mathbf{r}',t,0)]\,d\mathbf{r}' \\ &= -\frac{1}{\sigma_0}\int_{x_{k-1}}^{x_{k+1}}\int_{y_{l-1}}^{y_{l+1}}\int_{z_{m-1}}^{z_{m+1}}dx'\,dy'\,dz'\beta_k\left(\frac{x'}{\delta_x}\right)\beta_l\left(\frac{y'}{\delta_y}\right)\beta_m\left(\frac{z'}{\delta_z}\right)\nabla'\times\hat{z}[\nabla'\times\hat{z}V(\mathbf{0},\mathbf{r}',t,0)] \\ &= \begin{bmatrix} -K^{(V)}_{yy,klm}(t) & K^{(V)}_{xy,klm}(t) & 0 \\ K^{(V)}_{yx,klm}(t) & -K^{(V)}_{xx,klm}(t) & 0 \\ 0 & 0 & 0 \end{bmatrix}. \end{aligned} \tag{A12}$$

and we have written $z_m = m\delta_z - 2d$, $z_{m-1} = z_m - \delta_z$ and $z_{m+1} = z_m + \delta_z$.
Thus, the matrix $\mathcal{K}^{(V)}_{klm}(t)$, contains only transverse components and can be written as

$$K^{(V)}_{pq,klm}(t) = \frac{1}{\sigma_0}\int_{x_{k-1}}^{x_{k+1}}\int_{y_{l-1}}^{y_{l+1}}\int_{z_{m-1}}^{z_{m+1}}dz\,dx\,dy\,\beta_k\left(\frac{x}{\delta_x}\right)\beta_l\left(\frac{y}{\delta_y}\right)\beta_m\left(\frac{z}{\delta_z}\right)\frac{\partial^2 V(0,\mathbf{r},t,0)}{\partial p\,\partial q}, \tag{A13}$$

where $p,q = x$ or y.

Note that

$$\frac{\partial^2}{\partial p^2}\{J_0(\kappa\rho)\} = -\frac{\kappa^2 p^2}{\rho^2}J_0(\kappa\rho) - \frac{\kappa}{\rho}\left[1-\frac{2p^2}{\rho^2}\right]J_1(\kappa\rho) \tag{A14}$$

and

$$\frac{\partial^2}{\partial p \partial q}\{J_0(\kappa\rho)\} = -\frac{\kappa^2 pq}{\rho^2}[J_0(\kappa\rho) - \frac{2}{\kappa\rho}J_1(\kappa\rho)] \tag{A15}$$

which suggests that we can write

$$K^{(V)}_{pp,klm}(t) = \frac{1}{\sigma_0}\int_{x_{k-1}}^{x_{k+1}}\int_{y_{l-1}}^{y_{l+1}}\left[\left(\frac{p^2}{\rho^2}\right)S_0^1(\rho,m,t) + \left(1-\frac{2p^2}{\rho^2}\right)S_1^1(\rho,m,t)\right]\beta_k\left(\frac{x}{\delta}\right)\beta_l\left(\frac{y}{\delta_y}\right)dy\ dx \tag{A16}$$

$$K^{(V)}_{pq,klm}(t) = -\frac{1}{\sigma_0}\int_{x_{k-1}}^{x_{k+1}}\int_{y_{l-1}}^{y_{l+1}}\left(\frac{pq}{\rho^2}\right)\left[S_0^1(\rho,m,t) - 2S_1^1(\rho,m,t)\right]\beta_k\left(\frac{x}{\delta_x}\right)\beta_l\left(\frac{y}{\delta_y}\right)dx\ dy. \tag{A17}$$

with

$$\begin{bmatrix} S_0^1(\rho,m,t) \\ S_1^1(\rho,m,t) \end{bmatrix} = \frac{1}{(2\pi)^2 i}\int_0^\infty \int_{\mathrm{Br}} \frac{1}{s}\left(\frac{1}{\kappa}-\frac{1}{\gamma}\right) f_m(\kappa,s)e^{st}\,ds \begin{bmatrix} \kappa^2 J_0(\kappa\rho) \\ \kappa/\rho J_1(\kappa\rho) \end{bmatrix}\kappa d\kappa \tag{A18}$$

where

$$\begin{aligned} f_m(\kappa,s) &= \int_{z_{m-1}}^{z_{m+1}} \beta_m\left(\frac{z}{\delta_z}\right)\exp(-\gamma z)\,dz \\ &= \frac{1}{\delta_z\gamma^2}\exp(-\gamma z_m)[2-\exp(\gamma\delta_z)-\exp(-\gamma\delta_z)] \end{aligned} \tag{A19}$$

Write

$$\begin{bmatrix} S_0^1(\rho,m,t) \\ S_1^1(\rho,m,t) \end{bmatrix} = \frac{1}{2\pi\delta_z}\int_0^\infty [2F_3(\alpha,\kappa,z_m) - F_3(\alpha,\kappa,z_{m+1}) - F_3(\alpha,\kappa,z_{m-1})] \begin{bmatrix} \kappa J_0(\kappa\rho) \\ 1/\rho J_1(\kappa\rho) \end{bmatrix}\kappa d\kappa \tag{A20}$$

where (see Appendix B)

$$\begin{aligned} F_3(\alpha,\kappa,\zeta) &= \frac{\kappa}{2\pi i}\int_{\mathrm{Br}} \frac{1}{\gamma^2 s}\left(\frac{1}{\kappa}-\frac{1}{\gamma}\right)e^{-\gamma\zeta+s(t-t')}ds \\ &= \mu_0\sigma\,\frac{1}{2\pi i}\int_{\mathrm{Br}} \frac{1}{\gamma^3(\gamma+\kappa)}e^{-\gamma\zeta+s(t-t')}ds \end{aligned} \tag{A21}$$

A4 Moment Kernel Matrix evaluation

$$\begin{aligned}
\mathcal{M}^{(V)}_{klm}(t) &= -\frac{1}{\sigma_0}\int_{\Omega_{klm}} \beta_{klm}(\mathbf{r}')\nabla' \times \hat{z}[\nabla' \times \hat{z}W(\mathbf{0},\mathbf{r}',t,0)]\,d\mathbf{r}' \\
&= -\frac{1}{\sigma_0}\int_{x_{k-1}}^{x_{k+1}}\int_{y_{l-1}}^{y_{l+1}}\int_{z_{m-1}}^{z_{m+1}} dx'\,dy'\,dz'\beta_k\left(\frac{x'}{\delta_x}\right)\beta_l\left(\frac{y'}{\delta_y}\right)\beta_m\left(\frac{z'}{\delta_z}\right)\nabla' \times \hat{z}[\nabla' \times \hat{z}W(\mathbf{0},\mathbf{r}',t,0)] \\
&= \begin{bmatrix} -M^{(V)}_{yy,klm}(t) & M^{(V)}_{xy,klm}(t) & 0 \\ M^{(V)}_{yx,klm}(t) & -M^{(V)}_{xx,klm}(t) & 0 \\ 0 & 0 & 0 \end{bmatrix}. \qquad \text{(A22)}
\end{aligned}$$

Thus, the matrix $\mathcal{M}^{(V)}_{klm}(t)$, contains only transverse components and can be written as

$$M_{pq,klm}(t) = \frac{1}{\sigma_0}\int_{x_{k-1}}^{x_{k+1}}\int_{y_{l-1}}^{y_{l+1}}\int_{z_{m-1}}^{z_{m+1}} dz\,dx\,dy\,\beta_k\left(\frac{x}{\delta_x}\right)\beta_l\left(\frac{y}{\delta_y}\right)\beta_m\left(\frac{z}{\delta_z}\right)\frac{\partial^2 W(0,\mathbf{r},t,0)}{\partial p\,\partial q}, \quad \text{(A23)}$$

where $p, q = x$ or y. We write

$$M^{(V)}_{pp,klm}(t) = -\frac{1}{\sigma_0}\int_{x_{k-1}}^{x_{k+1}}\int_{y_{l-1}}^{y_{l+1}}\left[\left(\frac{p^2}{\rho^2}\right)S_0^2(\rho,m,t) + \left(1-\frac{2p^2}{\rho^2}\right)S_1^2(\rho,m,t)\right]\beta_k\left(\frac{x}{\delta}\right)\beta_l\left(\frac{y}{\delta_y}\right)dy\,dx \quad \text{(A24)}$$

$$M^{(V)}_{pq,klm}(t) = -\frac{1}{\sigma_0}\int_{x_{k-1}}^{x_{k+1}}\int_{y_{l-1}}^{y_{l+1}}\left(\frac{pq}{\rho^2}\right)\left[S_0^2(\rho,m,t) - 2S_1^2(\rho,m,t)\right]\beta_k\left(\frac{x}{\delta_x}\right)\beta_l\left(\frac{y}{\delta_y}\right)dx\,dy. \quad \text{(A25)}$$

where

$$\begin{bmatrix} S_0^2(\rho,m,t) \\ S_1^2(\rho,m,t) \end{bmatrix} = \frac{1}{(2\pi)^2 i}\int_0^\infty \int_{\mathrm{Br}}\left(-\frac{1}{s}\right)\frac{\partial}{\partial s}\left\{\left(\frac{1}{\kappa}-\frac{1}{\gamma}\right)f_m(\kappa,s)\right\}e^{st}\,ds \begin{bmatrix} \kappa^2 J_0(\kappa\rho) \\ \kappa/\rho J_1(\kappa\rho) \end{bmatrix}\kappa d\kappa \quad \text{(A26)}$$

Write

$$\begin{bmatrix} S_0^2(\rho,m,t) \\ S_1^2(\rho,m,t) \end{bmatrix} = \frac{1}{2\pi\delta_z}\int_0^\infty [2F(\alpha,\kappa,z_m) - F(\alpha,\kappa,z_{m+1}) - F(\alpha,\kappa,z_{m-1})]\begin{bmatrix} \kappa J_0(\kappa\rho) \\ 1/\rho J_1(\kappa\rho) \end{bmatrix}\kappa d\kappa \quad \text{(A27)}$$

where

$$\begin{aligned}
F(\alpha,\kappa,\zeta) &= \frac{\kappa}{2\pi i}\int_{\mathrm{Br}}\left(-\frac{1}{s}\right)\frac{\partial}{\partial s}\left\{\frac{1}{\gamma^2}\left(\frac{1}{\kappa}-\frac{1}{\gamma}\right)e^{-\gamma\zeta}\right\}e^{st}\,ds \\
&= \frac{\mu_0\sigma}{2}\frac{\kappa}{2\pi i}\int_{\mathrm{Br}}\frac{\kappa}{\gamma^3 s}\left[\left(\frac{2}{\gamma}+\zeta\right)\left(\frac{1}{\kappa}-\frac{1}{\gamma}\right)-\frac{1}{\gamma^2}\right]e^{-\gamma\zeta+st}\,ds \\
&= \frac{(\mu_0\sigma)^2}{2}\frac{1}{2\pi i}\int_{\mathrm{Br}}\frac{1}{\gamma^4}\left[\left(\frac{5}{2\gamma}+\zeta\right)\frac{1}{\gamma+\kappa}-\frac{1}{2\gamma^2(\gamma-\kappa)}\right]e^{-\gamma\zeta+st}\,ds \\
&= \frac{\mu_0\sigma}{4}[5F_5(\alpha,\kappa,\zeta) + 2\zeta F_4(\alpha,\kappa,\zeta) - F_5(\alpha,-\kappa,\zeta)] \qquad \text{(A28)}
\end{aligned}$$

Appendix B
Half-space matrix

B1 Definitions of Functions

For convenience, have defined a function $F_\nu(\alpha,\kappa,\zeta)$ through its inverse Laplace transform. Thus

$$F_\nu(\alpha,\kappa,\zeta) = \mu_0\sigma\,\frac{1}{2\pi i}\int_{\mathrm{Br}}\frac{1}{\gamma^\nu(\gamma+\kappa)}e^{-\gamma\zeta+s(t-t')}ds \tag{B1}$$

which can be written as

$$F_\nu(\alpha,\kappa,\zeta) = e^{-\kappa^2(t-t')/\mu_0\sigma_0}\,\frac{1}{2\pi i}\int_{\mathrm{Br}}\frac{1}{s^{\nu/2}(\sqrt{s}+\kappa)}e^{-\sqrt{s}\zeta+s(t-t')/\mu_0\sigma_0}ds \tag{B2}$$

For example, it is found that[15]

$$F_1(\alpha,\kappa,\zeta) = e^{\kappa\zeta}\mathrm{erfc}\left(\frac{\alpha\kappa}{2}+\frac{\zeta}{\alpha}\right), \tag{B3}$$

B2 Recursive Relation

Note that

$$\frac{1}{\gamma^\nu(\gamma+\kappa)} = \frac{1}{\kappa}\left[\frac{1}{\gamma^\nu} - \frac{1}{\gamma^{\nu-1}(\gamma+\kappa)}\right] \tag{B4}$$

therefore

$$F_\nu(\alpha,\kappa,\zeta) = \frac{1}{\kappa}\left[\exp\left(-\alpha^2\kappa^2/4\right)\alpha^{\nu-2}i^{\nu-2}\mathrm{erfc}(\frac{\zeta}{\alpha}) - F_{\nu-1}(\alpha,\kappa,\zeta)\right] \tag{B5}$$

Hence

$$F_2(\alpha,\kappa,\zeta) = \frac{1}{\kappa}\left[e^{-\alpha^2\kappa^2/4}\mathrm{erfc}\left(\frac{\zeta}{\alpha}\right) - e^{\kappa\zeta}\mathrm{erfc}\left(\frac{\alpha\kappa}{2}+\frac{\zeta}{\alpha}\right)\right], \tag{B6}$$

which can also be written as

$$F_2(\alpha,\kappa,\zeta) = \frac{1}{\kappa}e^{-\kappa\zeta-\xi^2}\left[e^{\zeta^2/\alpha^2}\mathrm{erfc}\left(\frac{\zeta}{\alpha}\right) - e^{\xi^2}\mathrm{erfc}(\xi)\right], \tag{B7}$$

where $\xi = \frac{\zeta}{\alpha}+\frac{\alpha\kappa}{2}$. Note that $e^{x^2}\mathrm{erfc}(x)$ may be evaluated at large arguments using an asymptotic expansion[15].

B3 Further Relationships

Define

$$f_\nu(\alpha,\kappa,\zeta) = \frac{1}{2\pi i}\int_{\mathrm{Br}}\frac{1}{\gamma^\nu s}e^{-\gamma\zeta+s(t-t')}ds \tag{B8}$$

and note that

$$\frac{1}{s} = \frac{\mu_0\sigma}{2\kappa}\left[\frac{1}{\gamma-\kappa} - \frac{1}{\gamma+\kappa}\right] \tag{B9}$$

hence

$$f_\nu(\alpha,\kappa,\zeta) = \frac{\mu_0\sigma}{2\kappa}\frac{1}{2\pi i}\int_{\mathrm{Br}}\frac{1}{\gamma^\nu}\left[\frac{1}{\gamma-\kappa}-\frac{1}{\gamma+\kappa}\right]e^{-\gamma\zeta+s(t-t')}ds \tag{B10}$$

$$= \frac{1}{2\kappa}[F_\nu(\alpha,-\kappa,\zeta)-F_\nu(\alpha,\kappa,\zeta)] \tag{B11}$$

Bibliography

[1] R. B. Thompson "Overview of the ECT POD Methodology," Review of Progress in Quantitative Non-destructive Evaluation, Vol. 18, D. O. Thompson and D. E. Chimenti, Eds. (Plenum, NewYork, 1999) pp. 2295-2304.

[2] J. R. Bowler and D. J. Harrison, "Measurement and Calculations of Transient Eddy Currents in Layered Structures," Review of Progress in Quantitative Non-destructive Evaluation, Vol. 11A, D. O. Thompson and D. E. Chimenti, Eds. (Plenum, NewYork, 1992) pp. 241-248.

[3] J. R. Bowler, "Transient Eddy Current in Layered Media as a Model of Corrosion Detection, Non-destructive Testing and Evaluation," Vol. 6 pp. 315-322, 1992.

[4] 54. J. R. Bowler, "Developments in Transient Eddy Current Non-destructive Evaluation, Nonlinear Electromagnetic Systems," The Proceedings of the International Symposium on Electromagnetics, 1995 A. Moses and A. Basak Eds. (IOS Press, Amsterdam 1996) pp. 623-627.

[5] C Tai, J. H. Rose and J. C. Moulder, "Thickness and conductivity of metalic layers from pulsed eddy-current measuremenst." Rev. Sci. Instrum. 67(11) pp3965-3972, 1996.

[6] J. R. Bowler, "Eddy current interaction with an ideal crack, Part I: The forward problem," J. Appl. Phys. 75(12) pp. 8128-8137, 15th June 1994.

[7] J. R. Bowler, S. J. Norton and D. J. Harrison, "Eddy current interaction with an ideal crack, Part II: The inverse problem," J. Appl. Phys. 75(12) pp. 8138-8144, 15th June 1994.

[8] S. J. Norton and J. R. Bowler, "The Theory of Eddy Current Inversion," J. Appl. Phys. 72 (2) pp. 501-512, 1993.

[9] J. R. Bowler, "Time Domain Half-Space Dyadic Green's Functions for Eddy-Current Calculations," J. Appl. Phys, Vol 86, No 11, pp 6494-6500, 1999.

[10] M. A. Howard and G. O. Mitchell, "Non-destructive Inspection for Hidden Corrosion in US Air Force Aircraft," in "Structural Integrity in Aging Aircraft" American Society of Mechanical Engineers, Aerospace Division, AD 47, 1995, pp195-212.

[11] J. R. Bowler, "Pulsed Eddy-Current Interaction with Subsurface Cracks," Review of Progress in Quantitative Non-destructive Evaluation, Volume 18, D. O. Thompson and D. E. Chimenti, Eds. (Plenum, New York, 1999).

[12] W. A. SanFilipo and G. W. Hohmann, "Integral equation solutions for the transient electromagnetic response of a three-dimensional body in a conducting half-space," *Geophysics,* Vol. 50, No. 5, 798-809, 1985.

[13] T. Wang and G. W. Hohmann, "A finite difference time-domain solution for three dimensional electromagnetic modelling," *Geophysics,* Vol. 58, No. 6, 797-809, 1993.

[14] S. Lee, J. B. Boersma, C. Law and G. A. Deschamps, "Singularity in Green's function and its numerical evaluation," *IEEE Trans. Antennas Propagat.,* Vol. AP-28, No.3, pp311-317, 1986.

[15] M. Abramowitz and I. A. Stegun, *Handbook of Mathematical Functions with Formulas, Graphs, and Mathematical Tables,* (John Wiley & Sons, New York, 10th Printing, 1970) pp1020-1030.

[16] J. R. Bowler, S. A. Jenkins, H. A. Sabbagh and L. D. Sabbagh, "Eddy-Current Probe Impedance Due to a Volumetric Flaw," J. Appl. Phys. Vol 70, No. 3 August 1st 1991, pp1107-1114.

[17] S. A. Jenkins and J. R. Bowler, "Calculation of Singular Matrix Elements," *IEEE Trans. Magnetics,* Mag-27, No. 6, 1991, pp4438-4444.

APPENDIX C

SOFTWARE GUIDE TO THE PULSED EDDY CURRENT MEASUREMENT MODEL

Iowa State University
Center for Nondestructive Evaluation

Iowa State University
Center for Nondestructive Evaluation
Applied Science Complex II
1915 Scholl Road
Amrs IA 50011-3042
USA

Tel. 515 294 2093
Fax 515 294 7771

Integrated QNDE and Reliability of Aging Aircraft Structures

Measurement model development for reliability assessment of pulsed eddy-current nondestructive evaluation

Software Guide to Veetrans

Part 1. Veetrans Installation Guide

Part 2. Veetrans User Guide

Contents

Part

1

Veetrans Installation Guide

Veetrans is a computer code for calculating the pulsed eddy current signals due to a region of corrosion in an otherwise uniform conductor. The signals are measured as a function of time by a Hall sensor on the axis of an excitation coil.

Code Installation

1. Initially the files should be copied into one folder *C:\Veetrans*.

2. Uses Windows Explorer or My Computer to find *install.bat* in *C:\Vtrans* and double click on the icon with the mouse.

3. The *install.bat* will rearrange the files putting the main executable *VtransGMats.exe* in *C:\Veetrans\bin* along with other files associated with the execution.

The application can be started via Windows Explorer or My Computer or by adding *VtransGMats* to the Task Bar or the Desk Top in the usual way.

Folders Structure

1. By default, the path to the root folder is *C:\Veetrans*.

2. The folder, *Veetrans,* has two sub-folders, *bin* and *tips*.

3. The folder, *bin,* contains the application which consists of an executable file, *VtransGMats.exe* and other files supporting the execution. In the folder *tips* files containing input and output data are stored. The main input files define the probe, the probe scan and the flaw. These files have the extension *.tip* indicating that it is a transient data input file. The main output file has the extension *.trn* indication that is contains the coordinates of the probe and transient signal data.

A *.tip* is edited to get the desired input data and the output data found in the *.trn* file can be plotted using suitable graphics utilities (not supplied).

Part

2

Veetrans User Guide

This guide describes how to use *Veetrans* to compute the transient eddy current probe signal due to a region of corrosion. The signals are measured as a function of time by a Hall sensor on the axis of an excitation coil. The output data are magnetic field values in Amps/m.

Veetrans Calculations

The calculation of the transient probe signal due to a region of corrosion depends on (a) the probe parameters (b) the specimen parameters (c) the position of the probe. These parameters are specified in a *.tip* file. Several such files can be created and the calculations for each file, called a *job*, carried out in sequence. A sequence of jobs is called a *run*. The *.tip* files used in for a run are specified in the *Runspec.ctr* file located in the *tip* folder. This is called the control file because it controls the selection of the *.tip* files that are used in a particular run (sequence of jobs). Below is an example of a *Runspec.ctr* file.

```
#
Number of jobs (integer)
        2
Job number (integer)    File root name
                0               'circ10x10x1'
                1               'Slot1x10x6'
```

• Figure 1: A typical *Runspec.ctr* file

The above control file will take the data from the file named *circ10x10x1.tip* and performs the calculation defined in it. It then does the same thing for the file *Slot1x10x6.tip*. Note that you are required to specify the number of jobs to be performed, a job number for each and the file root name for the job. Notes can be added to the file prior to the # and these will be ignored by the application. This allow the user to write some comments in the file. There must be a file *circ10x10x1.tip* and another *Slot1x10x6.*tip in the tips folder otherwise the application will not be able to perform the calculation. It is also important that the *.tip* files have the correct format.

Input data files

Before a calculation is performed it is usually necessary to create or edit a *.tip* file to specify the calculation. An example of such a file is given below. The application begins to acquire data from the file after the # 0 is encountered. Before that point any information can be written into the file but it is not used by *Veetrans*. There follows eight data fields labelled 0 though 7.

```
# 0
0 NOTE
1 x 10 x 6 flaw grid. flaw: 0.25x9.97x8.016mm. 30 x 20 microsec.

1 TIME
Sat Jun 24 2000

2 PROBLEM Root    problem domain accuracy conductivity(S/m)
          'slot10x6'    1       1      0.01     1.8792E+07

3 FLAW  no x  no y no z  dx (mm)  dy (mm)  dz (mm) setflaw
          1    10    6    0.25     0.997    1.336    -1

  100 100 100 100 100 100 100 100 100 100

  100 100 100 100 100 100 100 100 100 100

  100 100 100 100 100 100 100 100 100 100

  100 100 100 100 100 100 100 100 100 100

  100 100 100 100 100 100 100 100 100 100

  100 100 100 100 100 100 100 100 100 100

4 SCAN  startx(mm) starty (mm) step x (mm)  step y (mm)  no.x  no.y   lift off (mm)
          0.0       0.0          2.5           2.5          5     5      0.6

5 PROBE COIL  inner r(mm)  outer r   bottom z   top z   no. turns
                 7.1         11.41     0.0       5.0     2550
```

0 NOTE: This is a one-line text string acting as a summary of the file data.

1 TIME: The date and time of the file creation

2 PROBLEM: This data field contains:

1. The root name of the output files.
2. An integer designation of the problem type. Always use 1 to indicate that a forward problem is being solved.
3. The domain number is also always 1. This denotes that the conductor is modelled as a half-space.
4. The accuracy is then given as a decimal fraction. A value of 0.001 is suitable.
5. The conductivity of the material is then given (in S/m).

3 FLAW: The flaw is made up of a number of cells in a regular array. Each is a rectangular parallelpiped of the same size. The flaw data field defines the number of cells in the x-, y-, and z-directions and the size of the x-, y- and z-dimension in mm. The value of *setflaw* is always –1. The z coordinate is the vertical direction.

The conductivity of each cell is denoted by an integer between 1 and 100. A value of 1 means that the cell has a conductivity 1% less than that of the host material, a value of 100 means that the conductivity of the cell is 100% less than that of the host and therefore zero, a value of 75 means that the cell conductivity is 25% of the host value.

In the example above all the cells have a 100% reduction in conductivity and hence they have zero conductivity. This is typical of the way a crack or a void due to corrosion is represented since they are usually assumed to have zero conductivity. The cell values are given in blocks separated by a space. Each block has the same number of cells and represents different levels in the flaw starting at the top and working down. In the example there is only one line of values in each block indicating that there is only one cell in the x-direction. There are 10 values in the line one for each of the cells in the y-direction and there are 6 data blocks indicating that there are 6 levels of cells in the z-direction. The example therefore represents a slot of width 0.25 mm in the x-direction, 9.97 mm long and 8.016 mm deep.

Please note that none of the cell values can be zero. This will cause problems with the calculation.

4 SCAN: The probe position is varied over a regular grid starting at a location defined by *startx* and *starty*. These are the coordinates of the probe center in the *xy*-plane. The step size in the x and y directions are given in mm followed by the number of steps in the *x* and *y* directions. Finally the probe lift-off is defined. This is the distance from the coil reference level to the top of the work piece.

5 PROBE: The probe consists of a coil with a hall sensor on its axis. In the probe data field, the inner and outer radius of the coil is defined, the z coordinate of the bottom and the top of the coil and the number of turns. Note that the lift-off value is added to the top and bottom coordinates to get the location of the top and bottom of the coil with respect to the surface of the work piece.

6 TIME STEPS: This defines the number of time steps used to describe the pulse and the time interval between each signal sample. This time interval must be carefully controlled as discussed in the section Getting Started.

7 FLAW DEPTH: The first value in this data field is the distance from the top of the flaw region to the surface of the conductor. This distance is designated the ligament. The second value is the rise time of the coil current. The excitation of the pulsed eddy current is due the changing field caused by the

variation of the current in the coil. It is assumed that the coil current increases exponentially in time with a time constant given in this data field. Typically values for aircraft inspection for corrosion or subsurface cracks are in the range 50-500 micro-seconds. The third value in this data field is the height of the Hall sensor above the work piece in mm when the liftoff is zero. The *Liftoff* gets added to the height of the Hall sensor to give the distance from sensor to work piece.

Getting Started

The basic procedure for running a calculations is as follows:

1. Create or preferably edit a *.tip* file to define the input data.
2. Edit the *Runspec.ctr* file to include the new data file in the list of jobs.
3. Run the application.

The calculation becomes more accurate if the cell size is small but the smaller the cell size, the greater the number of cells needed for a given flaw and the longer it takes to do the calculation. It is best to do small calculation until experience with the results has been gained. Large calculations may have to run overnight but it is best to have some experience running small jobs before making the commitment to large calculations.

The calculation becomes more accurate if a small time interval is chosen but again the increase in accuracy comes at the cost of a longer calculation. A good rule of thumb is to assign a time increment dependent on the largest cell dimension: let da = max(dx, dy, dz) then the time increment is approximated by $dt=\mu\sigma (da)^2$.

D&W Enterprises, LTD.

Consulting Services

SPECIALIZING IN:
Nondestructive Inspection Engineering
Materials Science and Industrial Processes
Quality Assurance and Failure Analysis

APPENDIX D

SOFTWARE USER'S MANUAL

Excel ™ 95/7.0; 97; 2000 Macro

PROBABILITY OF DETECTION

FOR USE IN

ANALYSIS OF NONDESTRUCTIVE INSPECTION CAPABILITY DATA

Version 3.0

D&W Enterprises, LTD.
8776 W. Mountainview Lane TEL: (303) 791-1940
Littleton, CO 80125-9406 FAX: (303) 791-1940 - (Automatic Switching)
e-mail: wardduane@earthlink.net

NOTICE

Users are cautioned that the Macro is under development and currently operates only in conjunction with Microsoft Excel ™ 95/7.0; 97 and 2000 and is supplied as a user tool. No liability of any kind is assumed for the software or for use of the software. Users remain responsible for all results generated in conjunction with use of the software.

8776 W. Mountainview Lane TEL: (303) 791-1940
Littleton, CO 80125-9406 FAX: (303) 791-1940 - (Automatic Switching)
e-mail: wardduane@earthlink.net

I. INTRODUCTION:

The capability of a nondestructive inspection is dependent on

- **Flaw (Artifact) Variables**
- **Test Object Variables**
- **NDE Method Variables**
- **NDE Materials Variables**
- **NDE Equipment Variables**
- **NDE Procedure Variables**
- **NDE Process Variables**
- **Calibration Variables**
- **Acceptance Criteria / Decision Variables**
- **Human Factors**

A nondestructive inspection measurement is not single valued, but is probabilistic in nature due to its multi - parameter nature. The basis for use of probability of detection (POD) as a metric is discussed in detail in the attached papers and will not be discussed here [REF 1,2].

Since POD was developed and has been extensively applied to the assessment of crack detection capabilities in advanced engineering structures, examples of use in crack detection are included in the example data sets.

NOTE: Copies of the references are included on the CD.

II. REQUIREMENTS AND EXAMPLES INCLUDED:

A. SETTING UP THE COMPUTER FOR DATA ANALYSIS:

Excel ™ 95/7.0; 97 and 2000 have built in charting capabilities and templates. It also provides for user templates when a custom analysis and plotting routine is desired. Chart templates must be loaded BEFORE the analysis process is started. Set up instructions and templates for both shell and crack analysis are included on the CD (File - Computer Set up.doc). The following page is a copy of the single sheet, set up procedure.

8776 W. Mountainview Lane TEL: (303) 791-1940
Littleton, CO 80125-9406 FAX: (303) 791-1940 - (Automatic Switching)
e-mail: wardduane@earthlink.net

SETTING UP A COMPUTER FOR ANALYSIS

Excel programs have built in charting capabilities and templates. They also provides for user templates when a custom analysis and plotting routine is desired. User templates must be loaded BEFORE the analysis process is started.

To load a user template:

a) Select an analyzed data file with a plot in the format desired. Template plots have been provided for analysis of crack data by crack length. Load Excel and the appropriate chart example. The chart in the proper format must be visible when setting up a template.
b) From Tool Bar > [FORMAT] or [CHART]
c) Select [AutoFormat] or [Chart Type]
d) Select [User Defined]--
e) Select [Customize]
f) Select [Add] –
g) Dialog box will appear - INPUT [chart name -- for example - UT_Length

Use this user format in subsequent plotting.

8776 W. Mountainview Lane TEL: (303) 791-1940
Littleton, CO 80125-9406 FAX: (303) 791-1940 - (Automatic Switching)
e-mail: wardduane@earthlink.net

B. FILES INCLUDED ON THE CD

1. [Sample Plots]
   - Penetrant 1A.xlm
   - Penetrant 1B.xlm
   - Penetrant 1C.xlm
   - Penetrant 2A.xlm
   - Penetrant 2B.xlm
   - Penetrant 2C.xlm
   - Penetrant 3A.xlm
   - Penetrant 3B.xlm
   - Penetrant 3C.xlm

2. COMPUTER SET UP
   - W - Computer Set Up.doc

3. Manual in text format
   - W – POD Instructions
   - W – Reference : Rummel - Plenary Honor Lecture Paper - 1999.doc

4. Crack Length Analysis (The MACRO TOOLS)
   - XL - Interpol.xls – An interpolation tool
   - XL – Maxlikel.xls. – Maximum likelihood analysis module
   - XL - Verify.xls – Data verification module

5. Sample Files
   - XL - Sample A - Order.xls
   - XL - Sample B - Order.xls

6. [POD INSTRUCTIONS]
   - Excel 95.7.0
   - Excel 97
   - Excel 2000

8776 W. Mountainview Lane TEL: (303) 791-1940
Littleton, CO 80125-9406 FAX: (303) 791-1940 - (Automatic Switching)
e-mail: wardduane@earthlink.net

C. GENERAL REQUIREMENTS / EXERCISES

Sample files are included for initial analysis and exercise. You may prepare your own sample files by:

1. Loading a [Sample Plot] file (For Example – Penetrant 1a.xls;
2. Selecting [Sheet 1] from the bar at the bottom (this displays the analyzed data file);
3. Scrolling to the top and selecting all columns to the right of column D (E and above);
4. Deleting the selected columns;
5. Ordering the data as required.
6. Then starting analysis in the same manner as in the [Sample files].

Actual use of the Macro is a rather simple operation. Each step must be followed exactly to produce desired results. Instructions shown on the next pages provide the specific step-by-step instructions for analysis. For convenience, several template plots are included [Sample Plots] on this CD for use as templates.

1. DATA FORMAT

The data must be provide in the exact format and order shown in the [Example Data File]. The first row of each file is reserved for column and file header information. The columns must be in the following form:

a. Column A – Crack Number / Artifact Identifier
b. Column B - Crack Length / Depth / Diameter
c. Column C - Crack Depth (where applicable may be left blank)
d. Column D - 1 or 0 (Detect / nondetect)

The Macro operates on data located in Column B and Column D. Data in Column B must be ordered from the largest entry to the smallest entry without zero's The Macro counts down Column B until it finds an empty cell and then initiates analysis.

To order Column B data in Excel:

a. Selected Column B by clicking at the top of the column.
b. Copy Column B (Ctrl C).
c. Select Column A
d. On the TOOL BAR select Insert - Copied Cells. The data from Column B (Now shown as Column C) will now be duplicated in Column A.

8776 W. Mountainview Lane TEL: (303) 791-1940
Littleton, CO 80125-9406 FAX: (303) 791-1940 - (Automatic Switching)
e-mail: wardduane@earthlink.net

e. At the top of the columns, Select Columns A, B, C, D, and E. (They will appear highlighted)
f. On the TOOL BAR select Z-A↓. All data will now be ordered in concert to the data in Column A.
g. Click on Column A; right click and select DELETE. Data will now be in the form required for Analysis.

For your convenience and exercise, unordered data is provided in the file folder named [Example Data Files]. Select one of the data sets in this folder for practice or you may prepare your own files from reference data or user generated data.

8776 W. Mountainview Lane TEL: (303) 791-1940
Littleton, CO 80125-9406 FAX: (303) 791-1940 - (Automatic Switching)
e-mail: wardduane@earthlink.net

2. REQUIRED FILES

For execution, the macro requires that all three files provided in the [Crack Length Analysis] folders be loaded. It is necessary to close these files (do not save) each time the Macro program is run.

Select the folder [Crack Length Analysis]; the folder will open to show the three required files for analysis. Hold down the shift key and select all three files. The files will now be highlighted. Select OPEN. The three files will now be loaded.

Before Macro execution, it is necessary to have the data file in view. From the <TOOL BAR>, select <WINDOW> and click on the name of the prepared data file. Position the cursor at the top of Column E.

"Ctrl M" Starts the analysis.

Follow the step-by-step instructions for plotting as shown on the POD INSTRUCTION sheets.

The first notice that may appear, is a message that informs the user that the data distribution is not in a form that will allow the maximum likelihood analysis to converge. This indicates that the flaw distribution does not meet the requirements for absolute operation of the model. The data for the larger flaws will then be used for the analysis. This will result in a conservative POD plot. There are several reasons why data distribution will not meet the model requirements, but the most common are data out of order and too few misses at the lower defect sizes. The distribution must be adjusted for absolute convergence, but may not be possible in all cases. It is advised that a note be added to the footer information on all plots that do not converge. This lets the user know that the resulting plot is conservative and the actual capability is better than indicated by the data.

The second notice that the operator must deal with is the plotting parameters (noted as crack length). The crack length analysis program has been pre-set to plot from 0 to 0.750 inch in increments of 0.005 inch. Click ENTER to accept the pre-set values or modify the values to the desired plot. It is often desirable to plot as a function of crack depth or crack area. The range can be adjusted to the desired values. It may be convenient to save the files in a separate folder for crack depth or area analyses. The analysis programs have been protected with a password to avoid contamination and overwriting for different applications.

The analyzed parameters spread sheet will appear and the plotting routine should be followed in accordance with the POD INSTRUCTION sheets.

8776 W. Mountainview Lane TEL: (303) 791-1940
Littleton, CO 80125-9406 FAX: (303) 791-1940 - (Automatic Switching)
e-mail: wardduane@earthlink.net

POD
Program Instructions
(Applicable to Excel 95/7.0)

1. [USER FILE NAME] -Data must be in the form - Crack No. - Crack Length - Crack Depth - 1 or 0 (Detect / nondetect) - for analysis by crack length.
2. From the <FILE>//<OPEN> Select [Crack Length Analysis] folder and load all three programs -- "verify.xlm"; "maxlikel.xlm; and 'interpol.xlm. (for length).>>>{{OPEN}}. A Dialog box will appear. Click [READ ONLY].
3. Bring data to front (From the <TOOL BAR> Select <WINDOW>, [USER FILE NAME]. Place cursor at the top of the first open column – right of "Verified" (Column E).
4. CTRL - M; to start analysis. Analysis is completed.
5. A Dialog Box appears "POD Curve Table". Select the "maximum crack length " and "crack increment" to be used in plotting. 0.750 and 0.005 are the defaults.
6. From the <TOOL BAR> Click chart wizard; highlight columns $L and $M
7. Click Insert – Chart – As a new page.
8. A Dialog box appears, with range $L:$M, Click next.
9. Chart type appears - click scatter
10. Chart type appears - click line fit.
11. Click finish - POD curve appears.
12. From the <TOOL BAR> Click - insert new data - a box appears with range.
13. Switch to sheet 1, [Bottom tool bar] select $O:$P, click chart.
14. Click, x "Categories (X values) in first column).Then OK
15. From the <TOOL BAR> Select format – Autoformat.
16. Select, user defined
17. Click previous [USER FILE PLOT} POD -- OK. (Must have loaded the format previously – To load the applicable mode- See Note 1.
18. Change descriptive box data as applicable.
19. Enter 90% POD value - See Note 2.
20. From the <TOOL BAR> Select <FILE> Click Page set-up, Footer, enter description.
21. Data analysis is complete.
22. Print as desired.

Note 1:
To load a chart template (For Example – Pen 1A):

a) Load a previous POD plot into Excel.
b) From Tool Bar > Select [FORMAT]
c) Select [AutoFormat]
d) Select [User Defined]-- upper left corner
e) Select [Customize] – right corner

8776 W. Mountainview Lane TEL: (303) 791-1940
Littleton, CO 80125-9406 FAX: (303) 791-1940 - (Automatic Switching)
e-mail: wardduane@earthlink.net

f) Select [Add] – right side
g) Dialog box will appear - INPUT [chart name -- [FORMAT] for example - UT_Length
h) Select – [OK], Dialog Box will close
i) Use this user format in subsequent plotting.

Note 2:
To Interpolate for the 90% POD Value
a.) Got to Sheet 1 [Data] -- on the bottom tool bar.
b.) Scroll down Column M to the values at 89.XXX; 90.XXX
c.) Select these four cells <Example>

L	M
0.39	89.86499
0.395	90.01687

d.) Copy these four cells.
e.) From the <TOOL BAR> Select <WINDOW>, Select interpol.xls
f.) From the <TOOL BAR> Select <EDIT> "Paste Special"
g.) A Dialog box appears. Select "Values"
h.) The interpolation is completed and the 90% POD value appears to the right in units of both inches and millimeters.
i.) Copy these values to the descriptive data box on the <Chart>.

Your final Chart should look like this:

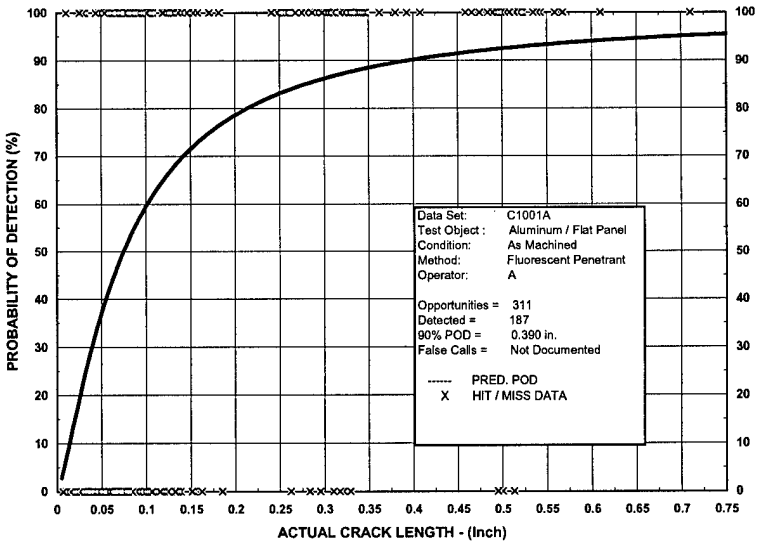

8776 W. Mountainview Lane TEL: (303) 791-1940
Littleton, CO 80125-9406 FAX: (303) 791-1940 - (Automatic Switching)
e-mail: wardduane@earthlink.net

POD
Program Instructions
(Applicable to Excel 97)

1. [USER FILE NAME] -Data must be in the form - Crack No. - Crack Length - Crack Depth - 1 or 0 (Detect / nondetect) - for analysis by crack length..
2. From the <FILE>//<OPEN> Select [Crack Length Analysis] folder and load all three programs --"verify.xlm"; "maxlikel.xlm; and 'interpol.xlm. (for length).>>>{{OPEN}}. A Dialog box will appear. Click [Enable Macro's} --Click [READ ONLY].
3. Bring data to front (From the <TOOL BAR> Select <WINDOW>, [USER FILE NAME]. Place cursor at the top of the first open column – right of "Verified" (Column E).
4. CTRL - M; to start analysis. Analysis is completed.
5. A Dialog Box appears "POD Curve Table". Select the "maximum crack length " and "crack increment" to be used in plotting. 0.750 and 0.005 are the defaults.
6. Highlight columns $L and $M
7. From the <TOOL BAR> Select [Insert Chart}
8. A Dialog Box Appears – Select [xy scatter]; NEXT
9. From the top bar Select [Series] NEXT…..NEXT
10. A dialog box appears. – Select "Place Chart" [As a new sheet].
11. Click [Finish]- POD curve appears.
12. From the <TOOL BAR> Select Chart – Add Data
13. Click - insert new data - a dialog box appears with range.
14. Switch to sheet 1, [Bottom tool bar] select $O:$P – [OK]
15. A dialog box appears {PASTE SPECIAL]
16. Click, x "Categories (X values) in first column).Then OK
17. From the <TOOL BAR> Select <CHART> ,CHART TYPE>
18. A dialog box appears. Select, "user defined"
19. Click previous [USER FILE PLOT} POD -- OK. (Must have loaded the format previously – To load the applicable mode- See Note 1.
20. X's appear on the top and bottom of the chart (Hit / Miss Values). Select one of the X's.; Double Click.
21. A dialog box appears. Select:
22. Line should be NONE
23. Marker should be CUSTOM
24. Select Style Symbol (ie. ▲)
25. Foreground – Select BLACK
26. Background – Select BLACK
27. Size – Select 8 pt.
28. [OK]
29. If you wish to have an insert descriptive box, Select from another chart (be sure the outline on the box is fully cross hatched. Copy and paste to the new chart. Text can then be edited to annotate the new chart.

POD
Program Instructions
(Applicable to Excel 97)

30. Enter 90% POD value - See Note 2.
31. From the <TOOL BAR> Select <FILE> Click Page set-up, Footer, enter description.
32. Data analysis is complete.
33. Print as desired.

Note 1:
To load a chart template (For Example – Pen 1A):

a) Load a previous POD plot into Excel.
b) From Tool Bar > Select [CHART]
c) Select [Chart Type]
d) Select [Custom Type] – Top Bar
e) Select [User Defined]-- Lower
f) Select [Add]
g) Dialog box will appear - INPUT [chart name -- for example - UT_Length
h) Select – [OK], Dialog Box will close
i) Use this user format in subsequent plotting.

Note 2:

a) To Interpolate for the 90% POD Value
b) Got to Sheet 1 [Data] -- on the bottom tool bar.
c) Scroll down Column M to the values at 89.XXX; 90.XXX
d) Select these four cells <Example>

L	M
0.39	89.86499
0.395	90.01687

e) Copy these four cells.
f) From the <TOOL BAR> Select <WINDOW>, Select interpol.xls
g) From the <TOOL BAR> Select <EDIT> "Paste Special"
h) A Dialog box appears. Select "Values"
i) The interpolation is completed and the 90% POD value appears to the right in units of both inches and millimeters.
j) Copy these values to the descriptive data box on the <Chart>.

POD
Program Instructions
(Applicable to Excel 97)

Chart should look like this:

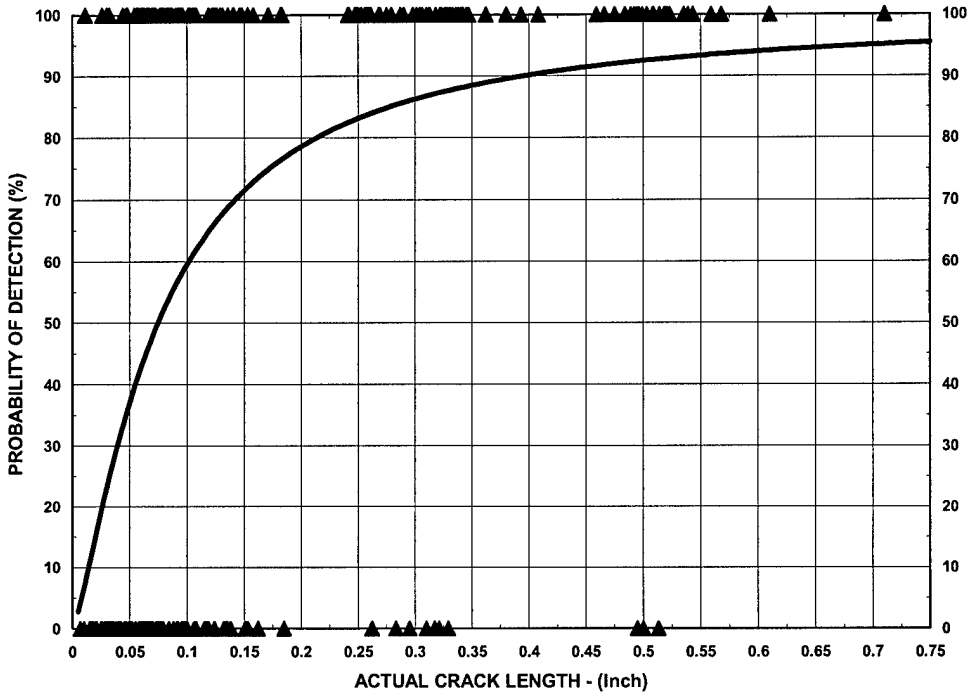

POD
Program Instructions
(Applicable to Excel 2000)

1. [USER FILE NAME] -Data must be in the form - Crack No. - Crack Length - Crack Depth - 1 or 0 (Detect / nondetect) - for analysis by crack length..
2. From the <FILE>//<OPEN> Select [Crack Length Analysis] folder and load all three programs --"verify.xlm"; "maxlikel.xlm; and 'interpol.xlm. (for length).>>>{{OPEN}}. A Dialog box will appear. Click [Enable Macro's} --Click [READ ONLY].
3. Bring data to front (From the <TOOL BAR> Select <WINDOW>, [USER FILE NAME]. Place cursor at the top of the first open column – right of "Verified" (Column E).
4. CTRL - M; to start analysis. Analysis is completed.
5. A Dialog Box appears "POD Curve Table". Select the "maximum crack length " and "crack increment" to be used in plotting. 0.750 and 0.005 are the defaults.
6. Highlight columns $L and $M
7. From the <TOOL BAR> Select [Insert Chart}
8. A Dialog Box Appears – Select [xy scatter]; NEXT
9. From the top bar Select [Series] NEXT…..NEXT
10. A dialog box appears. – Select "Place Chart" [As a new sheet].
11. Click [Finish]- POD curve appears.
12. From the <TOOL BAR> Select Chart – Add Data
13. Click - insert new data - a dialog box appears with range.
14. Switch to sheet 1, [Bottom tool bar] select $O:$P – [OK]
15. A dialog box appears {PASTE SPECIAL]
16. Click, x "Categories (X values) in first column).Then OK
17. From the <TOOL BAR> Select <CHART> ,CHART TYPE>
18. A dialog box appears. Select, "user defined"
19. Click previous [USER FILE PLOT} POD -- OK. (Must have loaded the format previously – To load the applicable mode- See Note 1.
20. X's appear on the top and bottom of the chart (Hit / Miss Values). Select one of the X's.; Double Click.
21. A dialog box appears. Select:
22. Line should be NONE
23. Marker should be CUSTOM
24. Select Style Symbol (ie. ▲)
25. Foreground – Select BLACK
26. Background – Select BLACK
27. Size – Select 8 pt.
28. [OK]
29. If you wish to have an insert descriptive box, Select from another chart (be sure the outline on the box is fully cross hatched. Copy and paste to the new chart. Text can then be edited to annotate the new chart.

POD
Program Instructions
(Applicable to Excel 2000)

30. Enter 90% POD value - See Note 2.
31. From the <TOOL BAR> Select <FILE> Click Page set-up, Footer, enter description.
32. Data analysis is complete.
33. Print as desired.

Note 1:
To load a chart template (For Example – Pen 1A):

a) Load a previous POD plot into Excel.
b) From Tool Bar > Select [CHART]
c) Select [Chart Type]
d) Select [Custom Type] – Top Bar
e) Select [User Defined]-- Lower
f) Select [Add]
g) Dialog box will appear - INPUT [chart name -- for example - UT_Length
h) Select – [OK], Dialog Box will close
i) Use this user format in subsequent plotting.

Note 2:
To Interpolate for the 90% POD Value

a) Got to Sheet 1 [Data] -- on the bottom tool bar.
b) Scroll down Column M to the values at 89.XXX; 90.XXX
c) Select these four cells <Example>

L	M
0.39	89.86499
0.395	90.01687

d) Copy these four cells.
e) From the <TOOL BAR> Select <WINDOW>, Select interpol.xls
f) From the <TOOL BAR> Select <EDIT> "Paste Special"
g) A Dialog box appears. Select "Values"
h) The interpolation is completed and the 90% POD value appears to the right in units of both inches and millimeters.
i) Copy these values to the descriptive data box on the <Chart>.

POD
Program Instructions
(Applicable to Excel 2000)

Chart should look like this:

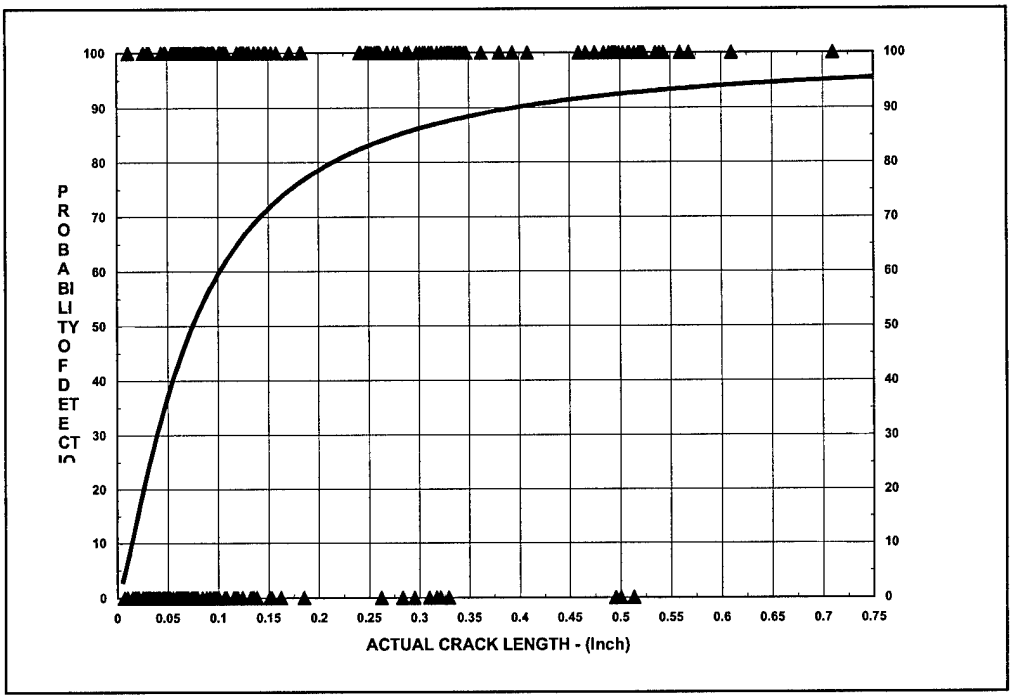

D. COMMENTS

The Macro is relatively simple, but was designed for users familiar with operation of Excel programs. A little practice is required to become comfortable with its operation.. Application to other data requires modification of some of the operating parameters. This will enable analysis of data on the NDE Capabilities CD is practice exercises.

Electronic copies of the reference paper is provided on the CD for user reference.

REFERENCES:

1. NDE Capabilities Data Book (3rd Edition - 1997), available from NTIAC, 415 Crystal Creek Drive, Austin, TX 78736-4725, Telephone: (512) 263-2106,(800) NTIAC 39, FAX: (512) 263-3530; CD version available.
2. Ward D. Rummel, "Nondestructive Evaluation Engineering", A Plenary paper prepared for and presented as an "Indian Society for Nondestructive Testing, Honorary Fellow Lecture to NDE - 99", 17 December 1999, Vadodara (Baroda), India.